

# The Kondo Effect in Quantum Dots

**Jörg D. Schmid**

Max-Planck-Institut für Festkörperforschung Stuttgart

2000



# The Kondo Effect in Quantum Dots

Von der Fakultät Physik der Universität Stuttgart zur Erlangung der  
Würde eines Doktors der Naturwissenschaften (Dr. rer. nat.) genehmigte  
Abhandlung

Vorgelegt von **Jörg D. Schmid** aus Mainz

Hauptberichter: Prof. Dr. Klaus von Klitzing  
Mitberichter: Prof. Dr. Martin Dressel

Tag der Einreichung: 6.9.2000  
Tag der mündlichen Prüfung: 20.11.2000

Max-Planck-Institut für Festkörperforschung Stuttgart

2000



# Contents

<b>1</b>	<b>Introduction</b>	<b>5</b>
<b>2</b>	<b>Sample structure and Coulomb blockade</b>	<b>8</b>
2.1	History of the Coulomb blockade of transport . . . . .	8
2.2	The quantum dot used in our experiments . . . . .	9
2.2.1	The basis: A two-dimensional electron system (2DES)	10
2.2.2	Dividing the 2DES by selective depletion with gate electrodes . . . . .	10
2.2.3	Contacting the quantum dot . . . . .	11
2.3	Single-electron tunneling and Coulomb blockade . . . . .	11
2.3.1	Single-electron tunneling . . . . .	13
2.3.2	Constant interaction model . . . . .	15
2.3.3	Charge stability diagram . . . . .	16
2.3.4	Current and transition rates . . . . .	19
2.4	Corrections to Coulomb blockade and single-electron tunneling	22
2.4.1	Fundamental limit . . . . .	22
2.4.2	Temperature . . . . .	23
2.4.3	Excited states for N electrons on the quantum dot . .	24
2.4.4	Tunnel-coupling and spectral density of the dot . . . .	24
2.5	Tunneling spectroscopy and differential conductance . . . . .	27
2.5.1	Resolution of tunnel-spectroscopy . . . . .	28
2.6	Analyzing a measurement for weak tunnel-coupling . . . . .	30
2.6.1	Energies of the dot . . . . .	30
2.6.2	Transition rates . . . . .	34
2.7	Summary . . . . .	37
<b>3</b>	<b>Resonances in the Coulomb blockade region</b>	<b>38</b>
3.1	Zero bias maximum for strong tunnel-coupling . . . . .	38
3.2	Deviation from single-electron tunneling . . . . .	40
3.3	Temperature dependence . . . . .	43
3.4	Splitting with magnetic field . . . . .	44
3.5	Other features in the Coulomb blockade regime . . . . .	44
3.6	Coulomb blockade lifted by strong tunnel-coupling . . . . .	47
<b>4</b>	<b>The Anderson Impurity model</b>	<b>50</b>
4.1	History of the Anderson impurity model . . . . .	50
4.2	The Hamiltonian of the Anderson impurity model . . . . .	51
4.3	Spectral density . . . . .	53

4.4	Properties for different parameter sets . . . . .	54
4.4.1	System without interaction $U = 0$ and finite level splitting $\Delta\varepsilon \neq 0$ . . . . .	55
4.4.2	Coulomb gap $U \neq 0$ and degeneracy $\varepsilon_{1/2} = \varepsilon_{-1/2}$ . . . . .	57
4.4.3	Master equation for the Anderson impurity model . . . . .	59
4.4.4	Spectral densities in the Anderson impurity model . . . . .	61
4.4.5	Finite Coulomb interaction and finite level splitting . . . . .	62
4.5	Non-equilibrium properties and finite temperatures . . . . .	62
4.5.1	Temperature dependence . . . . .	62
4.5.2	Finite bias voltage . . . . .	63
4.6	Extension to multiple states . . . . .	64
4.7	Application to quantum dots . . . . .	64
4.7.1	Relation of the spectral density to the observed differential conductance . . . . .	66
4.8	Observability of the signatures . . . . .	66
4.9	Deviations from the model . . . . .	67
4.10	Summary of the predictions for the Anderson impurity model . . . . .	67
4.10.1	Prediction 1: Resonance in the differential conductance at zero $V_{DS}$ . . . . .	68
4.10.2	Prediction 2: Splitting of this resonance for finite level splitting . . . . .	68
4.10.3	Prediction 3: Universal temperature dependence . . . . .	68
<b>5</b>	<b>Evaluation of the Kondo resonances</b> . . . . .	<b>70</b>
5.1	Magnetic field . . . . .	70
5.1.1	Field in the plane of the 2DES . . . . .	70
5.1.2	Constant magnetic field at different angles . . . . .	71
5.2	Temperature dependence . . . . .	71
5.3	Physical parameters and high energy behavior . . . . .	74
5.3.1	Temperature dependence of the differential conductance at $\mathbf{V}_{DS} = \mathbf{0}$ . . . . .	75
5.3.2	Relevance . . . . .	79
5.3.3	Conclusions on the scaling . . . . .	83
5.4	Speculations on the other features . . . . .	85
<b>6</b>	<b>Kondo resonances and electron configuration</b> . . . . .	<b>86</b>
6.1	Previous work . . . . .	86
6.2	Kondo resonances and electron configuration . . . . .	87
6.3	Interpretation of the transitions observed in a magnetic field . . . . .	90

6.4	Kondo effect in different Coulomb blockade regions . . . . .	92
6.5	Temperature dependence of the split Kondo resonances . . . . .	95
6.6	Other observations . . . . .	97
6.7	Summary . . . . .	101
<b>7</b>	<b>Conclusion</b>	<b>102</b>
<b>8</b>	<b>Deutsche Zusammenfassung</b>	<b>104</b>
8.1	Einleitung . . . . .	104
8.2	Übersicht über die einzelnen Kapitel . . . . .	105
8.2.1	Probenstruktur und Coulomb-Blockade . . . . .	105
8.2.2	Resonanzen im Bereich der Coulomb-Blockade . . . . .	106
8.2.3	Das Anderson-Störstellen-Modell . . . . .	107
8.2.4	Auswertung der beobachteten Kondo-Resonanzen . . . . .	108
8.2.5	Kondo-Resonanzen und Elektronenkonfiguration auf dem Quantenpunkt . . . . .	109
8.3	Zusammenfassung und Ausblick . . . . .	111
<b>A</b>	<b>Acknowledgments</b>	<b>113</b>
<b>B</b>	<b>Fock-Darwin spectrum</b>	<b>115</b>
<b>C</b>	<b>Two-dimensional electron system</b>	<b>117</b>
C.1	Edge-channel picture . . . . .	117
C.2	Application to a single point contact . . . . .	117
C.3	Consequences for the quantum dot . . . . .	120
<b>D</b>	<b>Sample preparation</b>	<b>121</b>
D.1	Heterostructure . . . . .	121
D.2	Cutting the samples . . . . .	122
D.3	Mesa etching . . . . .	122
D.4	Alloyed ohmic contacts . . . . .	127
D.5	Bond pads and gate leads . . . . .	129
D.6	Electron-beam lithography . . . . .	131
D.7	Splitting and mounting . . . . .	135
<b>E</b>	<b>Measurement setup</b>	<b>138</b>
E.1	Instrumentation . . . . .	138
E.1.1	TLM400 . . . . .	138
E.1.2	Kelvinox 400 . . . . .	139

E.2	Low temperature measurements . . . . .	140
E.2.1	Thermal noise . . . . .	140
E.2.2	RF-interference . . . . .	141
<b>F</b>	<b>Symbols and notations</b>	<b>143</b>
F.1	Conventions . . . . .	143
F.2	Abbreviations . . . . .	144
F.3	Physical constants . . . . .	144
F.4	Material parameters of the two-dimensional electron system (2DES) . . . . .	145
F.4.1	Derived material parameters . . . . .	146
F.5	Voltages applied to the sample . . . . .	146
F.6	Observables . . . . .	147
F.7	Other experimental parameters . . . . .	148
F.8	Characteristics of a quantum dot . . . . .	148

# 1 Introduction

In recent years, it has become possible to manufacture and study single-electron transistors [1]. Two major technological developments have contributed to this: The possibility to create structures on the nanometer scale and the accessibility of low temperatures in dilution refrigerators. The main effect in a single-electron transistor is the quantization of charge on a very small island. This leads to Coulomb gaps in the energy spectrum of this island and to a blockade of transport. The effect of Coulomb blockade can be observed for a variety of island types, from tiny metal particles [2] over nanotubes [3] to electrons confined in semiconductors which are weakly coupled via tunnel-barriers to source and drain leads [4, 5, 6, 7, 8, 9, 10, 11, 12, 13]. For islands made of semiconductors, it is possible to have structures of a size comparable to the Fermi wave-length of the electrons and the quantization of electronic states on the dot becomes visible. Systems that display Coulomb blockade and a discrete energy spectrum — in analogy to excitations in atoms — are called quantum dots and are the subject of the studies in this thesis. They are realized by selectively depleting a two-dimensional electron system via metal gates and studied in transport measurements.

Coulomb blockade of transport is well understood for weakly tunnel-coupled dots and the field is mature enough that applications are already considered. One actively pursued application is the use of single-electron transistors as a current standard [14, 15, 16, 17], another application is the use of single-electron transistors as sensitive electrometers [18, 19, 20, 21]. Here we want to use a single-electron transistor tunnel-coupled to source and drain leads to study fundamental physical questions: The main objective of this work is to use a quantum dot as an experimental realization of the Anderson impurity model [22] and study correlation effects of electrons on the dot and in the tunnel-coupled leads via transport. The Anderson impurity model — a simple model of a single spin-degenerate level tunnel-coupled to a reservoir of electrons — has been studied extensively throughout solid state physics, the level being of atomic origin. In our case the quantum dot will take the role of a controllable impurity.

The interest in this model is strong, because it has a rich set of solutions in spite of its simplicity. At low temperature correlations of the electrons on the dot and in the reservoirs become important, the crossover occurs on a new energy scale — the Kondo temperature — that depends non-trivially on the model parameters. In spite of 40 years of theoretical interest, the numerical renormalization group approach for which Wilson received his

Nobel prize in 1982 is still the only method to study the whole temperature range on a single footing.

This type of low-temperature anomaly was first observed experimentally in the 1930's on noble metals with impurities. The effect is named Kondo-effect after Jun Kondo who explained it as a correlation effect of conduction electrons that are scattered at a localized spin, by introducing the Kondo model, which is closely related to the Anderson impurity model.

On a more fundamental level our system touches the question of the measurement process in physics. The leads attached to the quantum dot can be seen as the measurement setup, the amount of tunnel-coupling could be seen as a perturbation of the system studied, the dot. As this perturbation gets small, one would naively expect to get closer to measuring the spectrum of the isolated dot. The calculations to the Anderson impurity model, however, tell us that this is not true at zero temperature: Even an infinitesimally small perturbation via tunnel-coupling changes the system qualitatively.

The system we have chosen is a quantum dot defined in a two dimensional electron system by depletion via split gates. The major advantage of this system is the in-situ control over the tunnel-barriers, which is not present in most other systems. The experimental challenge is the fabrication of a small island with large level-spacing and extremely low temperatures. The nice thing is that the Kondo effect carries a clear experimental signature — a resonance in the differential conductance at zero drain-source voltage within a Coulomb blockade region of the quantum dot.

This thesis is organized as follows:

- In Chapter 2 the sample is presented and a simple model — that of single-electron tunneling — is introduced to explain the Coulomb blockade effect observed for weak tunnel-coupling.
- In Chapter 3 experimental data are presented for which deviations from this model are visible. The resonances in the differential conductance at zero drain-source voltage are interpreted as Kondo resonances and studied throughout the rest of this thesis.
- In Chapter 4 the Anderson impurity model is presented and the main predictions are quoted. It is discussed under which circumstances this model is applicable to quantum dots and it is found, that the observed resonances at zero transport voltage can be understood as Kondo resonances. In this chapter it becomes clear that very small quantum

dots with large level-spacing are necessary and that low temperatures are essential.

- The Anderson impurity model requires a degeneracy of the underlying level and a splitting of the Kondo resonance is predicted if this degeneracy is lifted. This is studied in Chapter 5 and it is found that the Kondo resonances are due to a spin-degeneracy. There are specific predictions for the temperature dependence of the Kondo resonances. Here a quantitative comparison with our data is presented.
- Kondo resonances are not expected and do not occur in every Coulomb blockade region. In Chapter 6 the occurrence of Kondo resonances is studied and related to transitions in the dot states that are observed when applying a magnetic field perpendicular to the two-dimensional electron system.
- Experimental details that would render the main chapters unreadable are collected in several appendices. These comprise sample preparation and measurement setup in particular.
- A German summary is provided at the end of this thesis.

Some of the results presented in this thesis have already been published:

- A quantum dot in the limit of strong coupling to reservoirs, Jörg Schmid, Jürgen Weis, Karl Eberl and Klaus von Klitzing, *Physica B*, **256-258**, 182-185 (1998)
- Kondo resonances in split-gate quantum dots, Jörg Schmid, Jürgen Weis and Karl Eberl, *Physica E*, **6**, 375-378 (2000)
- Absence of odd-even parity behavior for Kondo resonances in quantum dots, J. Schmid, J. Weis, K. Eberl and K. v. Klitzing, *Phys. Rev. Lett.* **84**, 5824-5827 (2000)

Or accepted for publication:

- Split Kondo resonances in quantum dots at finite magnetic fields, Jörg Schmid, Jürgen Weis, Karl Eberl and Klaus von Klitzing, to be published in *Physica E*.

## 2 Sample structure and Coulomb blockade

In this chapter the sample is introduced and characterized. The measurements and descriptions presented here reproduce previous work. The basic structure is depicted in Figure 1. It consists of a microscopic island weakly tunnel-coupled to leads and capacitively coupled to a gate electrode and has been realized in many different ways. Understanding electron transport through this kind of structure requires the concepts of single-electron tunneling and Coulomb blockade which are introduced here. Single-electron tunneling is an approximate description that neglects the effects of the tunnel-coupling on the spectrum of the dot. Transport spectroscopy can be used to study these effects and forms the basis for the interpretation of the experiments.

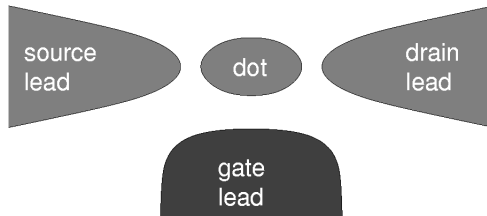


Figure 1: Single-electron transistor: The dot or microscopic island is weakly tunnel-coupled to the source and drain leads and electrostatically coupled to the gate lead.

### 2.1 History of the Coulomb blockade of transport

The first indications of Coulomb blockade were found in the non-linear current-voltage characteristics of metal particles embedded in films [23, 24]. Those experiments were relatively uncontrolled and had to be understood in terms of a large number of metallic islands. In spite of these experiments on islands, important theoretical work was done on single tunnel-junctions [25]. It was predicted that the quantization of charge tunneling through a junction with low capacitance would lead to voltage and current oscillations due to single-electron tunneling for a current bias across this junction. What makes this experimentally difficult to observe, is the fact that the leads contribute to the relevant capacitance. One way to get this contribution small is to use a large voltage-biased resistor close to the tunnel-barrier.

Equivalently these theories predicted that even a single tunnel-junction is subject to Coulomb blockade, but again a series resistor  $R > h/e^2$  is needed [26, 27] for Coulomb blockade to develop.

Using another tunnel-junction as this resistor, Fulton and Dolan [1] designed an aluminum structure with aluminum oxide tunnel-junctions that not only showed a nonlinear bias dependence, but also a periodic dependence of its characteristics on a gate voltage. *Single-electron transistors (SETs), defined as structures that show Coulomb blockade which is tunable by a gate*, have since been studied extensively both for metal islands in the superconducting and normal state [2]. It has been proposed that these SETs could be used in metrology, a frequency controlled transfer of single electrons establishing a new current standard [14, 15, 16, 17]. A new development is the use of SETs as sensitive potential probes in analogy to SQUIDs (superconducting quantum interference devices) as a sensitive flux probe [18, 19, 20, 21].

Another development was the realization of single-electron transistors in semiconductor structures [28]. The first type was the one that is also used in this thesis where the dots are isolated from a 2DES by gate electrodes [4, 5, 6, 7, 8, 9, 10]. In a second type of vertical structures the dots are laterally defined by etching [11, 12, 13]. In addition to those experiments with lithographically structured islands there exist a large number of experiments with “natural” islands, for example gold-clusters [29], semiconductor clusters [30], carbon nanotubes [3] and self-organized quantum dots [31]. Even though these islands are often times superior (smaller in size and sometimes even uniform on the atomic scale), contacting them in a controlled fashion remains an unsolved problem at this time.

## 2.2 The quantum dot used in our experiments

Quantum dots are distinguished from other single-electron devices by the observability of an discrete internal energy spectrum. In quantum dots the area to which the electrons are confined is comparable in size to the Fermi wavelength of these electrons. Semiconductors with low electron densities have a large Fermi wavelength and are a good starting point. In our samples the electrons are confined in one spatial dimension by using a modulation-doped GaAs/AlGaAs heterostructure [32, 33], the electrons form a two-dimensional electron system (2DES). In the other two spatial dimensions the electrons are confined to a small region by negative voltages applied to metal-gates patterned on the nanometer scale [34, 6, 8, 7]. Details of the

fabrication process for our quantum dots can be found in Appendix D, the basic elements and principles are described in the following.

### 2.2.1 The basis: A two-dimensional electron system (2DES)

The preparation and study of two-dimensional electron systems (2DES) is a rich field of its own. It has brought scientific surprises like the quantum Hall effects [35, 36] and the technologies involved have led to superior high frequency transistors and laser diodes.

Here we use a result from this field, namely a 2DES in a GaAs/AlGaAs heterostructure. A very simple picture of this modulation-doped heterostructure is sufficient for our experiments: The band-structure has a sharp minimum at a GaAs – AlGaAs interface created by MBE (molecular beam epitaxy) 50 nm below the sample surface. There is a discrete set of solutions for the z-component of the electron wave-function in this minimum, and the electron density is chosen such (via doping), that all electrons at the interface have the lowest energy z-component (see Figure 2). These electrons can move (almost) freely in the other two dimensions due to the following characteristics of the structure: On both sides of the interface GaAs and AlGaAs are lattice-matched to an underlying single crystal substrate, i. e. there are minimal structural sources for scattering (except for alloy disorder in the AlGaAs). In addition to this, the donors are removed from the plane of the 2DES to reduce scattering from the donors, a technique known under the name of modulation doping [32]. The detailed layer sequence of the MBE grown substrate is given in Appendix D.

### 2.2.2 Dividing the 2DES by selective depletion with gate electrodes

Gate electrodes on top of the heterostructure in a pattern depicted schematically in Figure 3(a) are used to define a potential landscape (Figure 3(b)) in the plane of the 2DES: A negative voltage of  $\approx -0.6$  V applied to these gates depletes the 2DES below the gates, leaving a nearly isolated area of 2DES below the opening between those so-called finger gates. From now on this puddle of electrons is called "quantum dot" or simply "dot". From the scanning electron microscope (SEM) image in Figure 3(c) one can estimate that the surface of the open area corresponds to that of a circle with  $r \approx 89$  nm which leads to an upper estimate for the number of electrons on the dot of  $N = \pi r^2 \times n_{2DES} \approx 80$ .

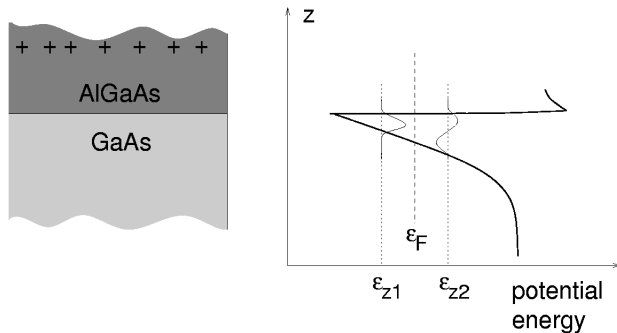


Figure 2: (a) Hetero-interface between GaAs and AlGaAs at which electrons are confined in  $z$ -direction. The positive dopants are removed from this interface. (b) Conduction-band edge, the two lowest energy states in  $z$ -direction and the position of the Fermi energy.

### 2.2.3 Contacting the quantum dot

Having controllable tunnel-barriers between the quantum dot and the leads is especially important for our experiment, as there is only a window in which interesting effects are expected: For weak tunnel-coupling, the correlation effects between dot and leads are not observable due to the finite temperature, for strong tunnel-coupling, charge quantization on the dot is lost. Due to the overall gate structure depicted in Figure 4, the drain and source contacts are isolated if all gates are at voltages below  $\approx -0.8$  V. For voltages above  $\approx -0.3$  V conductance takes place across the whole width of the Hall bar. For intermediate voltages, conductance across the dot sets in, the tunnel-coupling can be continuously controlled via the finger gates. This is the parameter range which is studied in the experiments.

## 2.3 Single-electron tunneling and Coulomb blockade

The gate electrodes can be tuned such, that there is a quantum dot weakly tunnel-coupled to the leads as depicted schematically in Figure 3(a). In this situation one can observe the Coulomb blockade effect: As a function of the drain-source voltage  $V_{DS}$  and the back-gate voltage  $V_{BG}$  rhomb-shaped areas of vanishing current are visible in Figure 5. In these regions of suppressed current a certain number  $N$  of electrons on the dot is stable against single-electron tunneling.

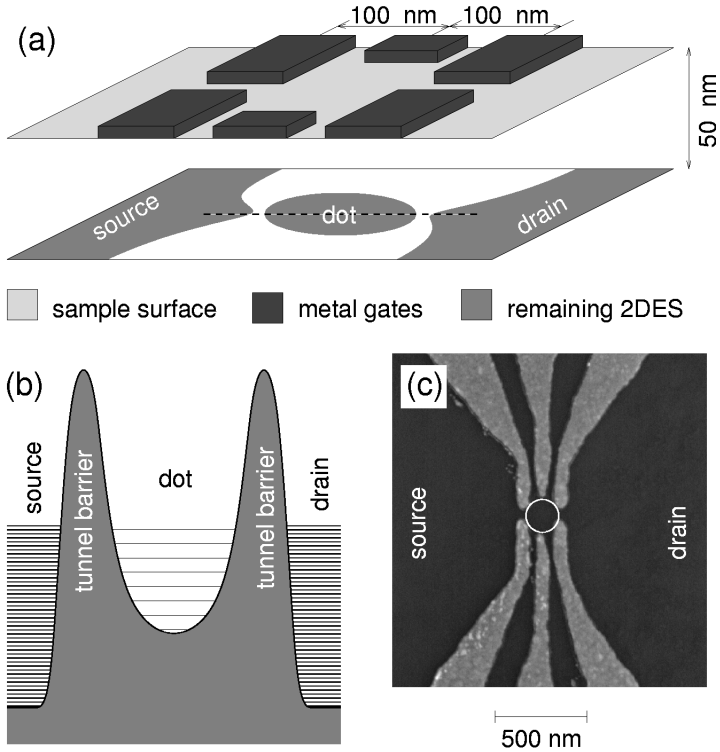


Figure 3: (a) Schematic pattern of the gates defining the quantum dot in the plane of the 2DES (not to scale). (b) Cut through the potential landscape along the dashed line in (a). (c) SEM image of these gates. The circle (radius  $r \approx 89$  nm) marks the area not covered by gates. Below this area electrons remain and form the quantum dot.

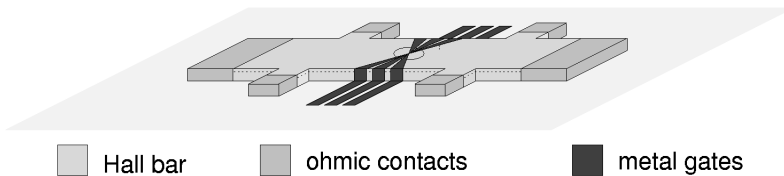


Figure 4: Overall sample structure, the 2DES is separated by the metallic gates into a source and drain region connected by the dot.

Even though the parameters of the quantum dot depend in a complicated fashion on all voltages applied to the system, there are simple models which allow the parameterization of our experiments. In this chapter, we want to compare experimental results in the case of weak tunnel-coupling to the predictions for single-electron tunneling in the constant-interaction model. Considering only ground states of the dot for different electron numbers, the areas of vanishing current can be qualitatively described. Excited states i. e. the internal degree of freedom on the dot are needed to explain structures observed outside the Coulomb-blockade regions.

In these considerations the constant interaction model — which is a phenomenological model for the energies of the isolated dot — can be easily replaced by other more accurate models that take into account e. g. the magnetic field. The description of electrical transport through the quantum dot in terms of single-electron tunneling is more difficult to correct. It can be seen as a lowest order perturbation theory in the tunnel-coupling and can fail spectacularly at low temperatures as will be seen in Chapter 3.

### 2.3.1 Single-electron tunneling

To describe transport through the quantum dot, the transparency of the barriers between the dot and the leads has to be taken into account.

The single-electron approximation does this under the following assumptions:

- *Transport takes place as a series of uncorrelated tunneling events of one electron across one barrier.*
- *Tunneling events through barrier  $r$  occur at a rate  $\Gamma_r$ , if energy-conservation permits the event.*

“*Uncorrelated*” in the above definition means that energy conservation has to be fulfilled for each “*tunneling event*”. In the expression “barrier  $r$ ”, “ $r$ ” stands for S or D corresponding to source and drain barrier respectively.

This approximation seems reasonable for the case of weak tunnel-coupling, as correlated tunneling is suppressed by a factor of  $(\hbar\Gamma)^n$  where  $n$  is the number of barriers that are tunneled and  $\Gamma = \Gamma_S + \Gamma_D$  the sum of the barrier transparencies.

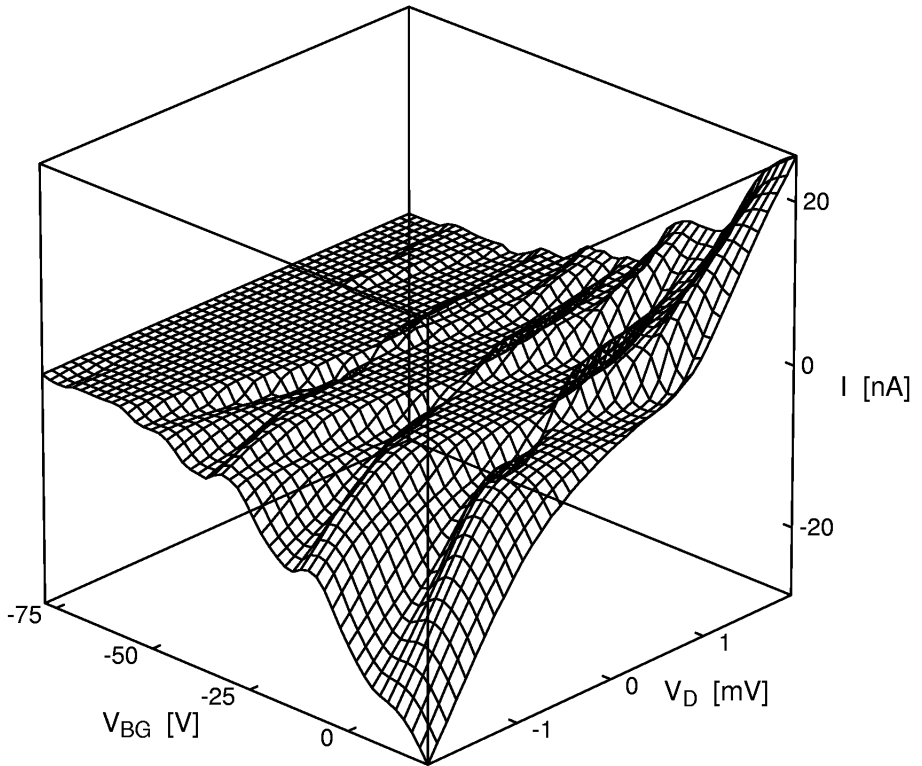


Figure 5: The Coulomb blockade effect measured at the base temperature of  $T \approx 30$  mK in a cryostat: The areas of vanishing current correspond to a number  $N$  of electrons being stable on the dot.

### 2.3.2 Constant interaction model

To study the energy conservation mentioned above, one needs a model for the energy of electrons on the dot and in the leads. The leads are described by a constant density of states occupied according to a Fermi-distribution. The dot is described by the constant interaction model (CI-model): The energy of  $N$  electrons in state  $I$  on the dot is given by a sum of "external energy"  $E_N$  due to the charge  $eN$  and an "internal energy"  $E_I^N$  due to the occupation  $I$  of a discrete level spectrum [37]:

$$E_{N,I} = E_N + E_I^N. \quad (1)$$

The Coulomb interaction between the electrons is quadratic in the electron number  $N$  and linear in the electrical potentials  $\varphi_i$  of the nearby electrodes:

$$E_N = \frac{e^2}{C_\Sigma} \frac{N(N-1)}{2} - Ne \sum_i c_i \varphi_i. \quad (2)$$

The constant in front of the quadratic term is conventionally written as  $e^2/C_\Sigma$ , for metallic islands  $C_\Sigma$  is the total capacitance and  $C_i = C_\Sigma \cdot c_i$  the capacitance between the dot and the electrode  $i$ .  $E_I^N$  is given by a sum over the energies of the occupied ( $n_i = 1$ ) single-particle levels  $\varepsilon_i$  of the dot:

$$E_I^N = \sum_i \varepsilon_i n_i.$$

Of course, the internal state  $I$  has to satisfy the condition  $N = \sum n_i$ .

When studying changes in the number of electrons on the dot, one has to know the energy needed for putting an additional electron onto the quantum dot. This energy for adding the  $N^{\text{th}}$  electron to the dot is given by the difference  $E_{N,F} - E_{N-1,I}$  of the total energies given by Equation (1). It is called "addition energy"  $\mu_{N,F,I}$  and is linear in  $\varphi_i$  as can be seen when substituting Equation (2):

$$\mu_{N,F,I} \equiv E_{N,F} - E_{N-1,I} = \frac{e^2}{C_\Sigma} (N-1) - e \sum_i c_i \varphi_i + E_F^N - E_I^{N-1}. \quad (3)$$

This model, which seems naive at first, can be used to fit the experiments as long as:

- All energies depend linearly on the applied voltages, i. e. the voltages applied are small enough to stay in the linear regime.

- The coefficients  $c_i$  of this linear relation do not depend on the number of electrons on the dot.

An agreement between the data and this model does not necessarily mean that the model is correct. It only means that the model captures the facts that it costs energy to add electrons to the dot, that the voltage dependence of the energies is linear and that the electrons on the dot have internal degrees of freedom. The constant interaction model is, therefore, useful to parameterize the experiments.

### 2.3.3 Charge stability diagram

The Coulomb blockade effect is understood in terms of a certain number  $N$  of electrons on the dot being stable against single-electron tunneling. Here we want to determine these regions of stability as a function of the drain-source voltage  $V_{DS}$  and a gate voltage  $V_G$ . The drain-source voltage is a unique parameter, because for single-electron effects it is related by the elementary charge  $e$  to the energies on the dot. The gate voltages change the energies of the dot and can be replaced in the argumentation with other parameters like the magnetic field.

Within the single-electron approximation only states that differ by one electron on the dot have to be compared in energy. Energy conservation for one electron leaving the dot towards the drain reservoir leads to the equation  $E_{N,0} - (E_{N-1,0} + \varepsilon_D) = 0$ , where  $\varepsilon_D$  is the energy of the level in the drain lead to which the electron is transferred and the index 0 for the internal states corresponds to the ground states. One has to take into account that at  $T = 0$  electrons from the source and drain leads are only available for energies  $\varepsilon$  below the respective electro-chemical potentials  $\mu_S$  and  $\mu_D$  i. e.  $\varepsilon_S \leq \mu_S$  and  $\varepsilon_D \leq \mu_D$ . Similarly, free states are only available above the electro-chemical potentials. Therefore the transition mentioned above is only possible for  $E_N - E_{N-1} = \varepsilon_D$ , i. e.  $\mu_N \geq \mu_D$ . In the single-electron tunneling approximation the  $N$  electron system can be unstable against gaining or losing an electron towards either the source or the drain contact, therefore four conditions have to be fulfilled for  $N$  electrons being stable on the dot:

$\mu_{N,0,0} \geq \mu_D$  gives stability against losing an electron towards the drain,

$\mu_{N+1,0,0} \leq \mu_D$  gives stability against adding an electron from the drain,

$\mu_{N,0,0} \geq \mu_S$  gives stability against losing an electron towards the source,

$\mu_{N+1,0,0} \leq \mu_S$  gives stability against adding an electron from the source.

These conditions can be rewritten using the CI-model (Equation (2)), paying special attention to the terms corresponding to the gate lead (index D) and the gate electrode (index G). This results in the following stability conditions for the  $N$ -electron ground state (for simplicity we choose  $V_S = 0$ ,  $\mu_S = 0$ ,  $V_D \equiv V_{DS}$  and assume  $\mu_D = -eV_{DS}$ ,  $\varphi_i = V_i$ ):

$$V_G \leq m_D V_{DS} + V_{G,N+1}$$

$$V_G \geq m_D V_{DS} + V_{G,N}$$

$$V_G \leq m_S V_{DS} + V_{G,N+1}$$

$$V_G \geq m_S V_{DS} + V_{G,N}$$

where

$$m_D = \frac{1 - c_D}{c_G}, \quad (4)$$

$$m_S = -\frac{c_D}{c_G}, \quad (5)$$

$$V_{G,N} = \frac{e(N-1)}{C_G} - \frac{\sum_i c_{i \notin \{DS,G\}} V_{i \notin \{DS,G\}}}{c_G} + \frac{E_0^N - E_0^{N-1}}{e c_G}. \quad (6)$$

These four conditions are depicted in Figure 6 and combined in Figure 7, showing a region where  $N$  electrons on the dot are stable against single-electron tunneling.

The largest voltage  $V_{DS\max}$  at which a suppression of transport can be expected is obtained from the conditions  $\mu_{N+1} = 0$  and  $\mu_N = \mu_D$  and one obtains:

$$V_{DS\max} = (V_{G,N+1} - V_{G,N}) \times c_G. \quad (7)$$

This can be used to define an Energy gap

$$E_G \equiv eV_{DS\max} \quad (8)$$

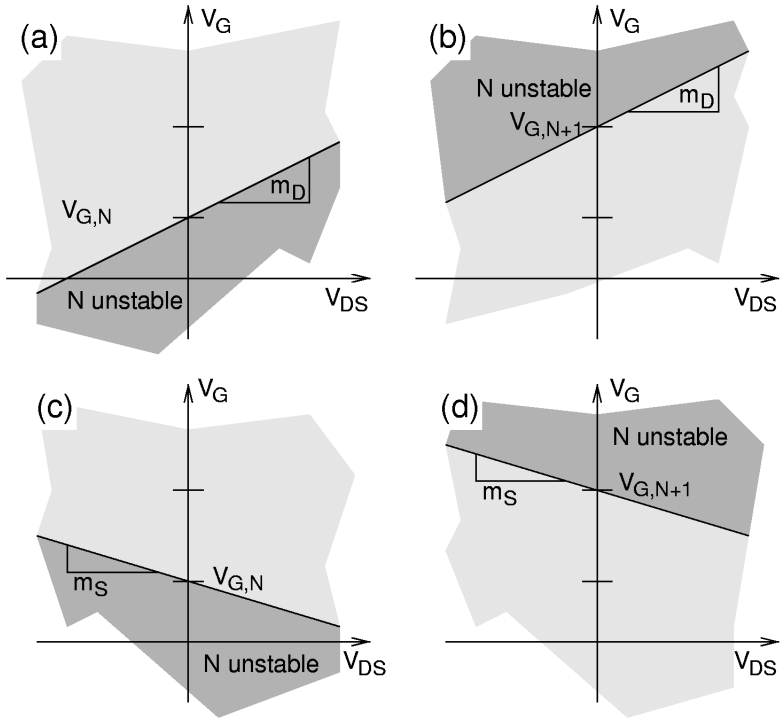


Figure 6: The dark areas mark the regions where the dot is unstable against (a) losing an electron towards the drain reservoir, (b) gaining an electron from the drain reservoir, (c) losing an electron towards the source reservoir (d) gaining an electron from the source reservoir.

which is — in the constant interaction model — determined by the Coulomb energy and the energy  $\varepsilon_{N+1}$  of the  $N + 1^{st}$  level:

$$E_G = \frac{e^2}{C_\Sigma} + \varepsilon_{N+1} - \varepsilon_N$$

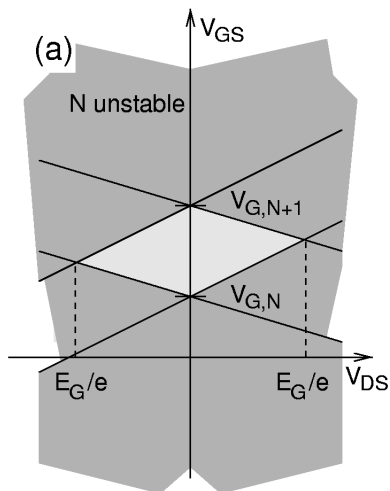


Figure 7: The region where  $N$  electrons are stable is marked by light grey.

This analysis can be done for any electron number and one obtains the pattern shown in Figure 8(a). As long as the effects of the internal degree of freedom are negligible, this pattern is periodic along the gate voltage axis. The schematic representation of a quantum dot given in Figure 8(b) provides an easy way to construct this stability diagram: The energies  $\mu_{N+i}$  can be shifted by the gate voltage  $V_G$  with respect to the Fermi energies of the reservoirs. The alignment of one of these energies with the Fermi levels  $\mu_S$  or  $\mu_D$  corresponds to one of the boundaries in Figure 8(a). For  $\mu_N$  these are drawn thick, solid for the alignment with  $\mu_D$ , dashed for the alignment with  $\mu_S$ .

### 2.3.4 Current and transition rates

In the previous section we have determined the regions of stability for certain electron numbers on the quantum dot. In this discussion the tunnel-coupling

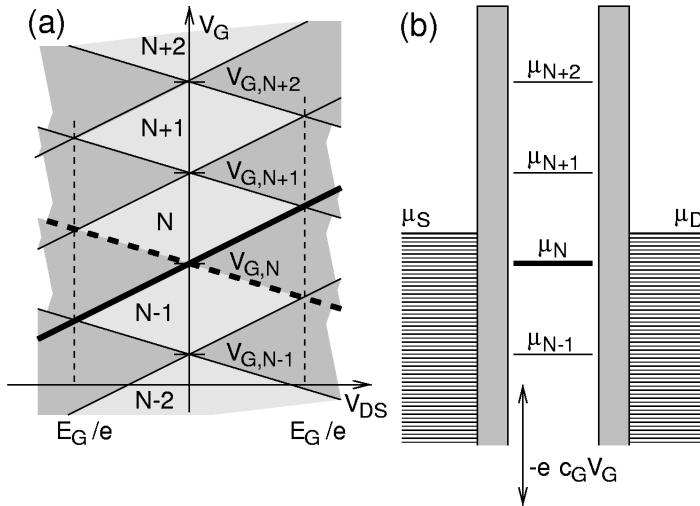


Figure 8: (a) Stable regions for different electron numbers. (b) Energy diagram of a quantum dot used to describe single-electron tunneling. The vertical axis is an energy axis. The energy-ladder in the middle corresponds to the addition energies  $\mu_{N+i}$  of the dot. The striped areas to the left and right correspond to the filled states in the reservoirs, the shaded areas to the tunnel-barriers.

played no quantitative role, even though a small amount of tunneling is necessary for the stable electron number to be reached in finite time. Here we want to determine what happens outside the stable regions where, for instance, the two electron numbers  $N$  and  $N - 1$  are allowed on the quantum dot. Again, these regions can be identified as a function of  $V_{DS}$  and  $V_G$  as shown in Figure 9(a), however, the following discussion considers only one configuration of the electrons (the ground state) for each electron number on the dot and is not valid for the whole region.

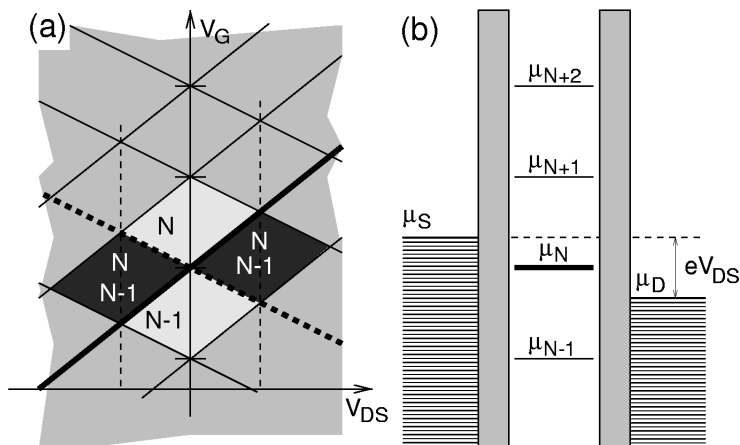


Figure 9: (a) The regions where only  $N$  and  $N - 1$  are allowed electron numbers are marked black. (b) This corresponds to situations where either  $\mu_{N+1} > \mu_S > \mu_N > \mu_D > \mu_{N-1}$  or  $\mu_{N-1} < \mu_S < \mu_N < \mu_D < \mu_{N+1}$ .

To determine the current, each tunnel-barrier  $r$  is characterized by a constant transparency  $\Gamma_r$ . The probabilities of finding the dot occupied by  $N$  or  $N - 1$  electrons ( $p_N$  and  $p_{N-1}$ ) are given by the following master equation [37] for the situation depicted in Figure 9(b):

$$\begin{aligned} p_N + p_{N-1} &= 1, \\ dp_N/dt &= -\Gamma_S p_N + \Gamma_D p_{N-1}, \\ dp_{N-1}/dt &= -\Gamma_D p_{N-1} + \Gamma_S p_N. \end{aligned} \quad (9)$$

The first equation corresponds to the fact that  $N$  and  $N - 1$  are the only accessible electron numbers. The other two equations describe the electron

exchange across the barriers. For the steady state ( $dp_N/dt = dp_{N-1}/dt = 0$ ) these probabilities are:

$$\begin{aligned} p_N &= \Gamma_D / (\Gamma_S + \Gamma_D), \\ p_{N-1} &= \Gamma_S / (\Gamma_S + \Gamma_D). \end{aligned}$$

The current is the rate at which electrons enter the dot from the source or, equivalently, the rate at which electrons leave towards the drain:

$$I = -e\Gamma_S p_N = -e\Gamma_D p_{N-1} = -e\Gamma_S\Gamma_D / (\Gamma_S + \Gamma_D). \quad (10)$$

This equation can be interpreted nicely in terms of the scheme in Figure 8(b). A constant current flows, when exactly one of the “levels” at the addition energies  $\mu_N$  falls into the window between  $\mu_S$  and  $\mu_D$ . This current is carried by electrons hopping across a single barrier at a time.

## 2.4 Corrections to Coulomb blockade and single-electron tunneling

The previous discussion is idealized but helpful as it gives an intuitive picture of single-electron tunneling. To come to a more realistic description of the experiments one has to include the effects of temperature, the additional effects of the internal degree of freedom and the effects of the tunnel-coupling. However, one has to be aware that there is a fundamental limit to the separation of the system into a dot connected to drain and source leads via tunnel-barriers.

### 2.4.1 Fundamental limit

The basic assumption in the previous considerations was that the tunnel-barriers are “high enough” to justify a separation of the system into three distinct areas, source–dot–drain connected by tunnel-barriers as indicated in Figure 3(b). The states on the dot are tunnel-coupled to the states in source and drain due to an overlap in their wavefunctions in the area under the barriers which leads to a finite lifetime  $1/\Gamma$  of an electron on the dot.

A limit to the validity of this model can immediately be given by Heisenberg’s uncertainty relation for the energy uncertainty or level spacing  $\Delta\varepsilon$  of an electron on the dot and the transparency of the barriers  $\Gamma = \Gamma_S + \Gamma_D$  which is the inverse lifetime for an electron on the dot:

$$\Delta\varepsilon/\Gamma > \hbar/2. \quad (11)$$

This relation is applicable to quantum dots with a discrete energy spectrum. For metallic systems an equivalent form of this relation can be obtained by assuming a constant density of states on the dot and a constant tunnel-coupling of these states to the reservoirs:

$$R_T > \hbar/2e^2 = h/4\pi e^2, \quad (12)$$

where  $R_T$  is the resistance of the tunnel-barriers. The equivalence can be seen as follows: Describing tunnel-barriers by a resistance makes sense for an island with states closely spaced compared to a corresponding voltage  $V$  across the barrier ( $\Delta\varepsilon \ll eV$ ). Assuming all states have identical tunnel-coupling  $\Gamma$  the current  $I$  can be obtained as a product of the number of states available for transport  $eV/\Delta\varepsilon$  the elementary charge  $e$  and the rate  $\Gamma$ :  $I = e^2(V/\Delta\varepsilon)\Gamma \Leftrightarrow R_T = V/I = (1/e^2)\Delta\varepsilon/\Gamma$ . Substituting this in Equation (11) results in Equation (12). Equation (12) is equivalent to

$$R_T C_\Sigma \times E_C > \hbar/2$$

[38, 39] in metallic systems where  $C_\Sigma$  denotes the total capacitance of the island. This is often taken as the starting point of this argument taking  $R_T C_\Sigma$  as the lifetime and  $E_C = e^2/C_\Sigma$  as the energy.

As will be seen later in this thesis, the tunnel-coupling can have qualitatively new effects on the spectral density of the dot below the so-called Kondo temperature. This imposes additional limitations to the validity of the single-electron tunneling approximation. These limitations can already be anticipated at this point, for a degenerate state on the dot one has to set  $\Delta\varepsilon = 0$  and Heisenberg's uncertainty relation (Equation (11)) cannot be fulfilled for finite tunnel-coupling.

### 2.4.2 Temperature

The equations above are given for zero temperature. The effect of temperature can be easily included in terms of the distribution functions for the reservoirs:

$$f_r(\varepsilon) = f_F((\varepsilon - \mu_r)/k_B T).$$

These reduce to the step-function at  $T = 0$  K that was assumed in the previous discussion for simplicity. Specifically, the master equation (Equation 9) can not be reduced to two electron numbers and the transition rates

are given by a product of  $\Gamma_r$  and a distribution function  $f_F(\mu_N - \mu_r)$  or  $1 - f_F(\mu_N - \mu_r)$  where  $N$  is the index of the transition considered.

The results of the inclusion of temperature are not surprising, the steps become broadened by  $k_B T$  and the corrections to the  $T = 0 K$  result become exponentially small with the energy difference between  $\mu_S$  and  $\mu_D$  and the nearest resonance  $\mu_N$ . When  $k_B T$  becomes comparable to  $E_G$  the effects of Coulomb blockade are smeared out.

### 2.4.3 Excited states for $N$ electrons on the quantum dot

Until now the existence of different configurations of  $N$  electrons on the dot has been neglected in the discussion of stability and transport. This is justified for small voltages  $|V_{DS}| < \Delta\mu_{N,1,0}/e$ , where  $\Delta\mu_{N,1,0} = E_1^N - E_0^N$  is the energy distance to the first excited state of the  $N$ -electron system. Measurements at higher drain-source voltages give interesting information about the inner degrees of freedom of the dot as studied extensively in [40, 41].

The main results are summarized in Figure 10, where the same considerations were made as in section 2.3.3. It is important to note that the meaning of the broken lines corresponding to the excited states in Figure 10 differs from those of the ground-states. The alignment of a ground-state transition with e.g.  $\mu_D$  leads to a step across the  $(V_{DS}, V_G)$ -plane, whereas the corresponding alignment of an excited state addition energy leads to a current step only outside the stability region of  $N$  electrons. The effect of excited states for the other electron numbers is not given explicitly for clarity. Transitions between excited states of both electron numbers involved can be identified by the fact that the corresponding line does not reach the boundary where  $N$  electrons are stable. The point marked by a circle in Figure 10(a) corresponds to the conditions  $\mu_{N,0,0} = \mu_D$  and  $\mu_{N,0,1} = \mu_S$ . This can be rewritten as

$$\mu_{N,0,1} - \mu_{N,0,0} = \mu_S - \mu_D = eV_{DS}, \quad (13)$$

which is a simple and important relation for interpreting the data.

### 2.4.4 Tunnel-coupling and spectral density of the dot

The single-electron tunneling approximation includes the tunnel-coupling  $\Gamma$  only in the lowest order. Nevertheless, it gives an intuitive picture of electrons hopping across one barrier at a time and is the starting point for interpreting the experiments. One approach to include the tunnel-coupling more

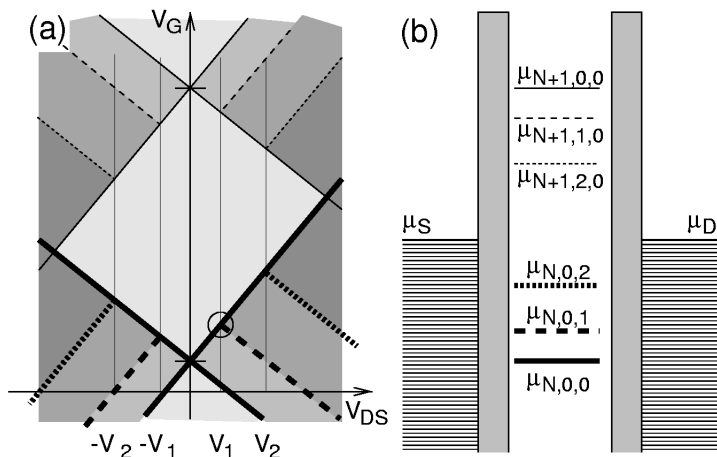


Figure 10: Taking two excited states of the  $N$  electron system into account: (a) The areas where one and two excited states are accessible in single-electron tunneling are marked by the two darkest grey levels. (b) Energy scheme including excited states of the  $N$  electron system.

accurately is the inclusion of second or higher order processes known under the name “cotunneling”. More than one barrier can be tunneled coherently either involving the same dot-state (“elastic cotunneling”) or different dot-states (“inelastic cotunneling”) [42, 43]. The term “coherently” means that energy conservation has to be fulfilled for the whole process and intermediate (“virtual”) states are acceptable at all energies. In the Coulomb blockade region at low temperatures, cotunneling dominates transport because single-electron tunneling is suppressed exponentially  $\propto \exp(-\Delta E/k_B T)$  whereas cotunneling is only suppressed by an energy denominator  $\propto 1/\Delta E^2$  where  $\Delta E$  is the energy difference symbolized in Figure 11. The energy conservation can again be used to identify where in the  $(V_{DS}, V_G)$ -plane a certain higher order process is possible, this is done in Chapter 3.

Here we will no further consider cotunneling for directly calculating the current through the dot. Instead, it is possible to represent all results in close analogy to the single-electron tunneling picture given above by introducing the spectral density  $A$  of the dot which will be defined more rigorously in Chapter 4. In this framework, transport is understood in the same way as in single-electron tunneling, but the addition-energy spectrum of the isolated dot is replaced by a spectral density that includes all higher order effects of

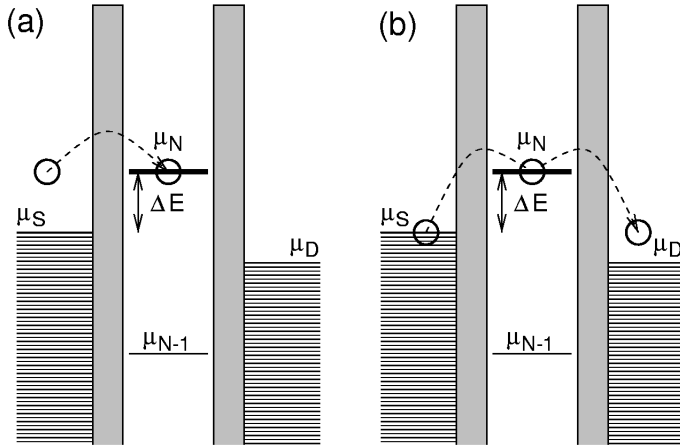


Figure 11: (a) For single-electron tunneling there are no electrons available in the source. (b) Cotunneling involves transmission through at least two barriers and a virtual intermediate state at a higher energy.

the tunnel-coupling. The tunnel-coupling and the corresponding finite lifetime of the electrons on the dot leads to a broadening of the onset of current at the addition energies  $\mu_N$  which are from now on called single-particle resonances. The single-electron approximation corresponds to a simple approximation for the spectral density that becomes correct in the limiting case of vanishing tunnel-coupling. For low transport voltages  $V_{DS}$  and temperatures there is a gate-voltage range, where only the ground states of the  $N$  and  $N - 1$  -electron system (which are assumed to be non-degenerate here) are accessible in analogy to Equations (9) and Figure 9(b). The addition of an electron at the addition energy  $\mu_N$  is represented by a delta function in the spectral density at this energy:  $A(\omega) = \sum_N \delta(\omega - \mu_N/\hbar)$  in the absence of tunnel-coupling and in the presence of tunnel-coupling by a Lorentzian at the energy  $\mu_N$  broadened by the sum of the transparencies of the source and the drain barriers [44]

$$A(\omega) = \sum_N \frac{\Gamma_S + \Gamma_D}{2\pi((\omega - \mu_N/\hbar)^2 + (\Gamma_S + \Gamma_D)^2/4)}. \quad (14)$$

The relation to the previous discussion can be seen as follows: The horizontal lines at the energies  $\mu_N$  in Figure 8(b) correspond to delta functions in the spectral density. The comparison of the dot energies with the electro-

chemical potentials of drain and source is replaced by an energy integral over a product of the spectral density  $A$  and the distribution functions (as will be shown in Chapter 4):

$$I = -e \frac{\Gamma_S \Gamma_D}{\Gamma_S + \Gamma_D} \int_{-\infty}^{\infty} A(\omega) [(f_F(\omega - \mu_S)(1 - f_F(\omega - \mu_D)) - (f_F(\omega - \mu_D)(1 - f_F(\omega - \mu_S)))] d\omega.$$

At  $T = 0$  in the situation depicted in Figure 9(b) this reduces to

$$I = -e \frac{\Gamma_S \Gamma_D}{\Gamma_S + \Gamma_D} \int_{\mu_S/\hbar}^{\mu_D/\hbar} A(\omega) d\omega \quad (15)$$

and for a delta function one recovers Equation (10). The relation (15) is sketched in Figure 12.

The constant interaction model leads to a spectral density where the peak positions depend on a linear combination of the surrounding electrical potentials  $c_i \varphi_i$  and a simple form of the spectral density

$$A(\omega) = \sum_N (p_{N-1} + p_N) \delta(\omega - ec_i \varphi_i / \hbar + \text{const}_N).$$

Over a limited parameter range ( $\{\mu_S, \mu_D\} \gg \mu_{N-1}$  and  $\{\mu_S, \mu_D\} \ll \mu_{N+1}$ ) the sum of the occupation probabilities ( $p_{N-1} + p_N$ ) is constant at  $T = 0$ .

## 2.5 Tunneling spectroscopy and differential conductance

In the last subsection, the effect of a drain-source voltage and a gate voltage on the the current through a quantum dot was discussed. However, now we want to concentrate on the spectrum of the dot which is just a slightly different way of looking at the experiments. The sharp Fermi edges of source and drain can be used as a spectrometer. The variation of the current with a small variation of the electro-chemical potential of the drain  $d\mu_D$  causes a current change

$$\frac{dI}{d\mu_D} = -\frac{e}{\hbar} \frac{\Gamma_S \Gamma_D}{\Gamma_S + \Gamma_D} A(\mu_D/\hbar, V_i) - e \int_{\mu_S/\hbar}^{\mu_D/\hbar} \frac{dA}{d\mu_D} d\omega. \quad (16)$$

The second term in this equation is zero if  $A$  is independent of  $\mu_D$  and in this case one obtains:

$$\frac{dI}{d\mu_D} = -\frac{e}{\hbar} \frac{\Gamma_S \Gamma_D}{\Gamma_S + \Gamma_D} A(\mu_D/\hbar, V_i).$$

In the experiment one can set  $d\mu_D = -e dV_D$  leading to a simple relation between the differential conductance and the spectrum of the dot:

$$\frac{dI}{dV_D} = \frac{e^2}{\hbar} \frac{\Gamma_S \Gamma_D}{\Gamma_S + \Gamma_D} A(\mu_D/\hbar, V_i), \quad (17)$$

as depicted schematically in Figure 12(a). Noting that the maximum value of the spectral density in Equation (14) is  $2/(\pi(\Gamma_S + \Gamma_D))$  one obtains the maximum possible value for the differential conductance through a single level of  $e^2/h$  in the case of  $\Gamma_S = \Gamma_D$ .

The assumption that  $A$  is independent of  $\mu_D$  corresponds to  $c_D = 0$ . In the experiments this is not the case. Assuming that  $A$  depends only on a linear combination of the surrounding electrical potentials and the energy in the form  $A(\omega, V_i) = A(\omega - ec_i\varphi_i/\hbar + const)$  one obtains from Equation (16):

$$\frac{dI}{d\mu_D} = -\frac{e}{\hbar} \frac{\Gamma_S \Gamma_D}{\Gamma_S + \Gamma_D} (A(\mu_D/\hbar, V_i) - c_D A(\mu_D/\hbar, V_i) + c_D A(\mu_S/\hbar, V_i))$$

and for the differential conductance:

$$\frac{dI}{dV_D} = \frac{e^2}{\hbar} \frac{\Gamma_S \Gamma_D}{\Gamma_S + \Gamma_D} ((1 - c_D)A(-eV_D/\hbar) + c_D A(-eV_S/\hbar)), \quad (18)$$

which is the relation that is applicable to our experiments and is depicted in Figure 12(b).

Still, this is only the whole truth for the case of  $A(\omega, \varphi_i) = A(\omega - ec_i\varphi_i/\hbar)$ , which is only applicable over limited parameter ranges and only in the case that the energies of the isolated dot can be treated separately from the tunnel-coupling. The interesting effects of Coulomb interaction and a precise definition of the spectral density are discussed in Chapter 4.

### 2.5.1 Resolution of tunnel-spectroscopy

In the experiments, the resolution of this type of spectrometry is limited by the temperature  $T$  which can be as low as 50 mK corresponding to an energy of  $k_B T = 4.3 \mu\text{eV}$ . Another limit is the applied voltage modulation  $\Delta V_D$  which was chosen between  $1 \mu\text{V}$  and  $4.2 \mu\text{V}$ .

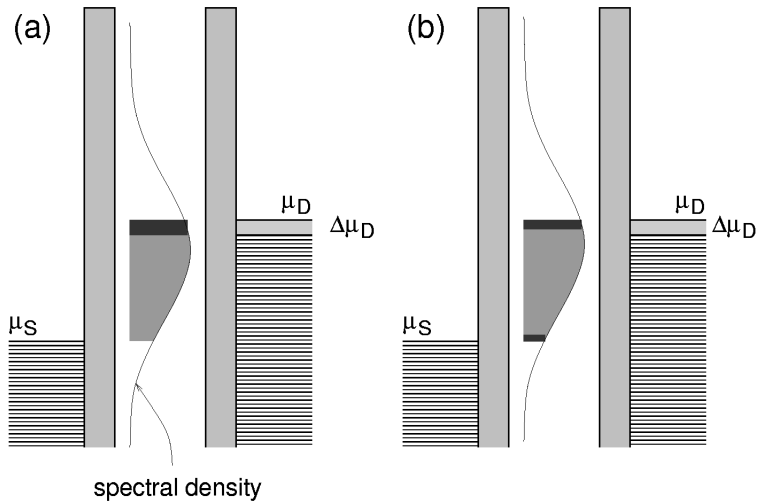


Figure 12: The shaded areas under the spectral density are proportional to the current, the black area under the spectral density corresponds to the change in current due to  $\Delta\mu_D$ , (a) for fixed spectral density (b) for the spectral density shifted by  $e c_D \varphi_D$ .

## 2.6 Analyzing a measurement for weak tunnel-coupling

It is instructive to apply the models presented thus far to a measurement in the case of weak tunnel-coupling. The position of the single-electron resonances can be used to get information about the energies of the dot and their dependence on the applied voltages. The width of these resonances is related to the transition rates  $\Gamma$  via Planck's constant  $h$ , whereas the current is related to the transition rates via the elementary charge  $e$ .

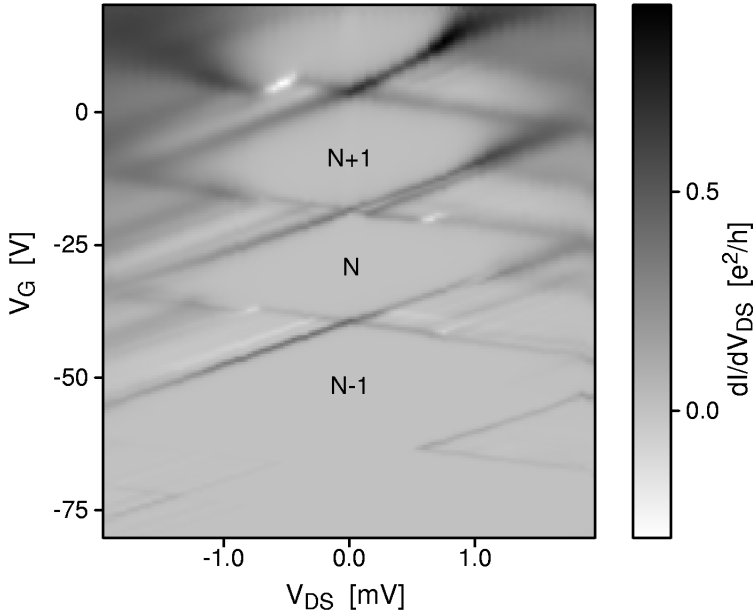


Figure 13: Differential conductance measured at the same time as the current in Figure 5.

### 2.6.1 Energies of the dot

**Boundaries of the  $N$ -electron Coulomb blockade region** For the data presented in Figure 13, the voltage  $V_{BG}$  applied to the back gate serves as the gate voltage  $V_G$ . The back gate is a metal layer of the chip carrier

onto which the sample is glued, i. e. it is  $\approx 0.5$  mm below the quantum dot. For the CB-region marked by  $N$  in Figure 13 one can extract the slopes and intercepts as given in Figure 6:

for ground state transitions towards  $N - 1$ :

$$V_{G,N} = -39.5 \text{ V} \pm 0.5 \text{ V},$$

$$m_{D,N} = 8.2 \cdot 10^3 \pm 0.2 \cdot 10^3,$$

$$m_{S,N} = -3.3 \cdot 10^3 \pm 0.2 \cdot 10^3;$$

for ground state transition towards  $N + 1$ :

$$V_{G,N+1} = -18.5 \text{ V} \pm 0.5 \text{ V},$$

$$m_{D,N+1} = 8.3 \cdot 10^3 \pm 0.2 \cdot 10^3,$$

$$m_{S,N+1} = -3.5 \cdot 10^3 \pm 0.2 \cdot 10^3.$$

### Interpreting these parameters in the constant interaction model

For the constant interaction model one expects  $m_{D,N+1} = m_{D,N}$  and  $m_{D,N+1} = m_{D,N}$ , which is fulfilled within the accuracy of the measurement and in the following the average value is used, i.e.  $m_D = (m_{D,N+1} + m_{D,N})/2 = 8.25 \cdot 10^3$  and  $m_S = (m_{S,N+1} + m_{S,N})/2 = -3.4 \cdot 10^3$ .

When interpreting the ground state transitions in the constant interaction model, i.e. using the relation (4) and (5), one obtains for the coupling to the drain contact

$$c_D = 1/(1 - m_D/m_S) = 0.29,$$

for the coupling to the gate contact

$$c_G = 1/(m_D - m_S) = 8.7 \cdot 10^{-5},$$

and for the maximum energy gap following from Equation (8)

$$E_G = e(b_{N+1} - b_N) \times c_G = 1.8 \text{ meV}.$$

Assuming that the gap is mostly due to Coulomb energy one can determine the total capacity :

$$C_\Sigma = e^2/E_G = 8.9 \cdot 10^{-17} \text{ F}.$$

The calculated peak positions from these extracted model parameters, agree not only in the limited parameter range shown in Figure 14(a) for which they were extracted, but even the extrapolation to different electron numbers in Figure 14(b) shows only slight deviations from the experimental data in the

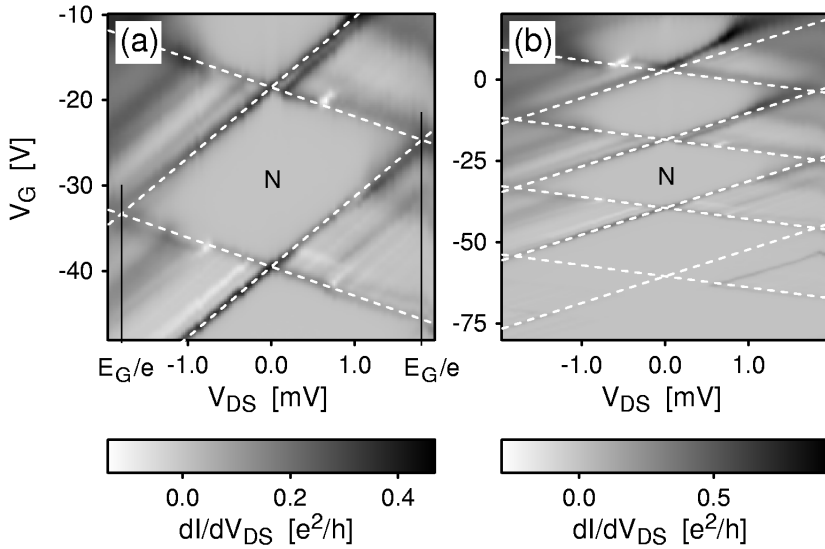


Figure 14: Differential measurement of the data in Figure 5: (a) Interpreting the ground-state transitions in the constant interaction model. (b) Extension to different electron numbers.

parameter  $V_{G,N+2}$ , which can be taken as an indication that the assumption of a gap dominated by Coulomb energy is valid.

It is interesting to look at the coefficients  $c_i$  and the associated capacitances  $C_i = C_\Sigma \cdot c_i$ . One sees immediately that the capacitance  $C_{BG}$  to the back gate — 0.5 mm away — does not contribute significantly to the total capacitance. The source and drain contacts combined (assuming a symmetric dot) make up almost two thirds of the total capacitance. From other measurements with a pair of top gates as the gate voltage the corresponding coefficients for the gate fingers are determined as  $c_M \approx c_R \approx c_L \approx 0.1$ . The normalized capacitances of the gates close to the quantum dot approximately add up to 1 as expected.

The agreement between the model and the boundaries of the  $N$  electron CB region does not necessarily mean that the model is correct. Any model for the dot energies that is both linear in the applied voltages and the electron number will result in this type of fit. The structure observed outside of the CB region indicates that excited states have to be taken into account.

**Analyzing the first excited state** The data in Figure 14 clearly show signatures of excited states. In the constant interaction model we can also interpret the signature of the first excited state of the  $N$  electron system using one additional parameter  $\Delta\mu = \mu_{N,0,1} - \mu_{N,0,0}$ . The pattern expected for this state is depicted in figure 10(a), signatures for other excited states visible in figure 14 are not evaluated. A comparison with the constant interaction model including a level at  $\Delta\mu = 258 \mu\text{eV}$  is given in Figure 15(a). This value was chosen to fit the light lines in the region where the occupation of the dot changes between  $N$  or  $N - 1$ , these lines are better visible in Figure 14(a). There is a noticeable deviation from this model, namely that the value of  $\Delta\mu$  seems to be smaller for the region where the occupation of the dot changes between  $N + 1$  and  $N$  electrons. In addition to this, the transitions involving the excited state have a slightly different slope than those involving only ground states. This can be modeled — in a deviation from the constant interaction model — by assuming different capacitances for the excited state. The candidates are  $C_G, C_\Sigma, c_D$ , i.e. there are more parameters than one has data. However, with  $c_G = 9.1 \times 10^{-5}$  one gets the best agreement as indicated in Figure 15(b). Different  $C_\Sigma$  leads qualitatively to a similar change in  $\Delta\mu$  across the CB region, but the slopes of the single-electron tunneling lines remain unchanged (see Figure 15(c)). Different  $c_D$  lead to a pattern that is not observed in the experiment:  $\Delta\mu$  does not change with  $V_G$  and the slopes of the single-electron resonances changes

differently from what is observed (Figure 15(d)).

In conclusion, one can see that a careful analysis gives additional information about the states involved. The constant interaction model is not sufficient to explain the data, the shape of the charge distribution or the level quantization are important.

### 2.6.2 Transition rates

To get information about the transition rates from the current using Equation (10) one needs the current value corresponding to transport involving only the ground states of the  $N$  and  $N - 1$  electron system. Due to temperature and tunnel-coupling the transition from Coulomb blockade to a constant current is not sharp, as seen in Figure 16. One has to identify the parameter range where  $V_{\text{DS}}$  is high enough that the current is saturated but low enough that no excited states are involved in transport. As long as no excited state is involved one expects the symmetry  $I(V_{\text{G}} - V_{\text{G},N}, V_{\text{DS}}) = -I(-V_{\text{G}} + V_{\text{G},N}, -V_{\text{DS}})$  from the argument leading to Equation (10) where  $V_{\text{G},N}$  is the position of the resonance. The curves in Figure 16(a) and (b) span the relevant parameter range: for low  $|V_{\text{DS}}|$  the current is not saturated and for high  $|V_{\text{DS}}|$  a shoulder appears that can be attributed to an excited state of the  $N$ -electron system due to its lack of symmetry.

The absolute value of the saturation current  $|I|$  in Figure 16(a) determines the “serial transparency”

$$\Gamma_{\text{s}} \equiv \Gamma_{\text{S}}\Gamma_{\text{D}}/(\Gamma_{\text{S}} + \Gamma_{\text{D}}) = |I|/e, \quad (19)$$

as can be seen from Equation (10). This is the rate at which electrons pass through one dot-level if they are not restricted by the distribution functions of the leads. The absolute value of the saturation current is indicated in Figure 16(a) by a dashed line at  $I = 1.9 \text{ nA}$  ( $I = 2 \text{ nA}$  in (b)). The rate at which electrons traverse the dot is  $\Gamma_{\text{s}} = I/e = 1.2 \times 10^{10} \text{ Hz}$  corresponding to a linewidth of  $\hbar\Gamma_{\text{s}} = I \times h/e^2 = 7.8 \mu\text{eV}$ .

The linewidth  $\hbar\Gamma$  of the single-electron resonances in the differential conductance can be used to determine the sum of the barrier transparencies

$$\hbar\Gamma = \hbar(\Gamma_{\text{S}} + \Gamma_{\text{D}}). \quad (20)$$

Again, one expects a symmetry  $dI/dV_{\text{DS}}(V_{\text{G}} - V_{\text{G},N}, V_{\text{DS}}) = dI/dV_{\text{DS}}(-V_{\text{G}} + V_{\text{G},N}, -V_{\text{DS}})$  as long as excited states can be neglected. This symmetry is

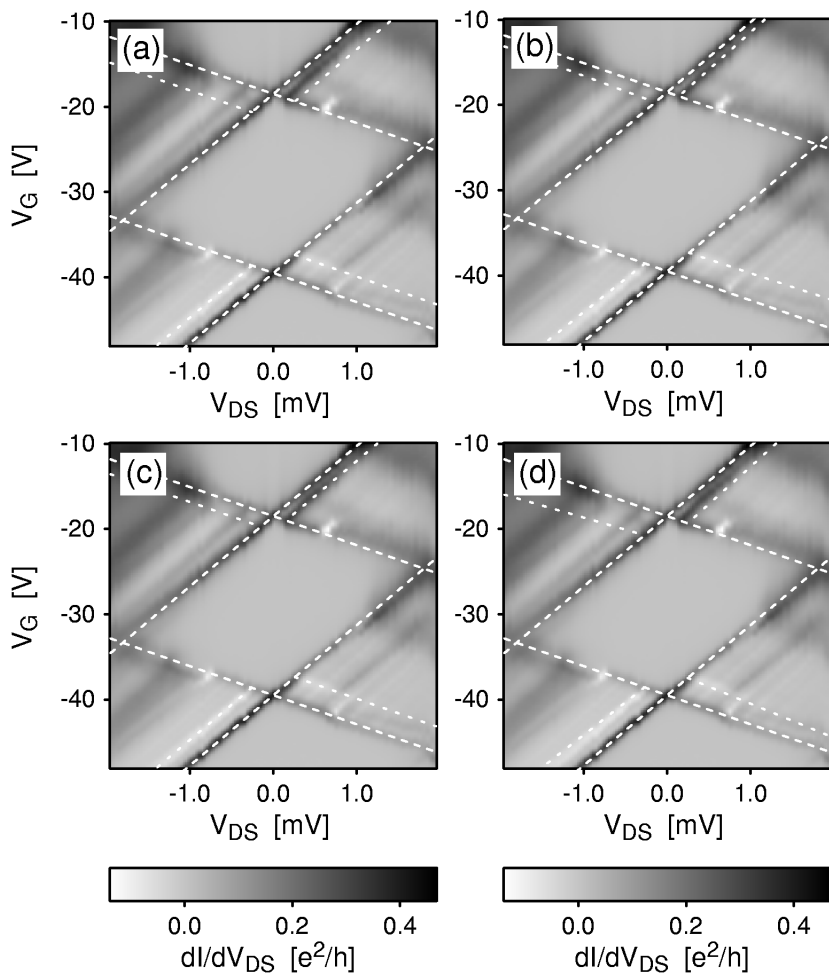


Figure 15: (a) First excited state, the position marked by a dotted line corresponds to  $\Delta\varepsilon = 258 \mu\text{eV}$  in the constant interaction model. (b) Using a different value of  $c_G$  for the first excited state. (c) Trying to fit the data with a different  $C_\Sigma$ . (d) Trying to fit the data with a different  $c_D$ .

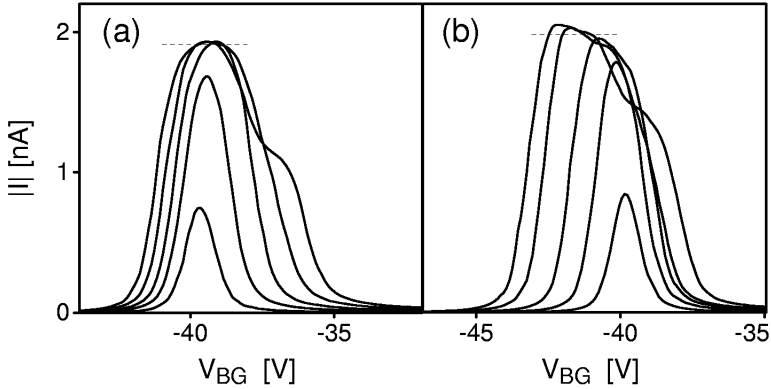


Figure 16: Absolute value of the current for (a) positive  $V_{DS}$  (b) negative  $V_{DS}$  in  $100 \mu\text{eV}$  steps.

not well fulfilled in the data in Figure 17. One possible explanation is that the excited state at  $\Delta\mu = 258 \mu\text{eV}$  can not be neglected at  $V_{DS} \approx 200 \mu\text{V}$ . The back gate voltage axis can be converted to an energy axis by multiplication with the normalized gate capacitance  $c_G$  and the electron charge  $e \times 8.7 \cdot 10^{-5}$ . Thus, the data in Figure 17 are used to obtain the linewidths in terms of energy, as given in the Figure caption.

The values obtained for  $\Gamma_s$  from the current and for  $\Gamma$  from the linewidths can be used to get information about the drain and source barriers and their transition rates  $\Gamma_S$  and  $\Gamma_D$ . Combining Equations (19) and (20) and solving for the transparency of the source barrier, one obtains a result that is not unique:  $\Gamma_s = \Gamma/2 \pm \sqrt{\Gamma^2/4 - \Gamma_s\Gamma}$ . Due to the symmetry of the equations, one obtains the same result for the drain barrier. One of the two solutions corresponds to the source and one to the drain barrier, however, one cannot determine from the data in Figures 16 and 17 which is which. The results are  $\Gamma_+ = 99 \mu\text{eV}$ ,  $\Gamma_- = 8.5 \mu\text{eV}$  for the widest peak in Figure 17 and  $\Gamma_+ = 83 \mu\text{eV}$ ,  $\Gamma_- = 8.6 \mu\text{eV}$  for the narrowest peak. Even though the intrinsic width of the peaks is overestimated due to temperature, one can see that the barriers are asymmetric and that the one with the smaller transparency limits transport through the whole system.

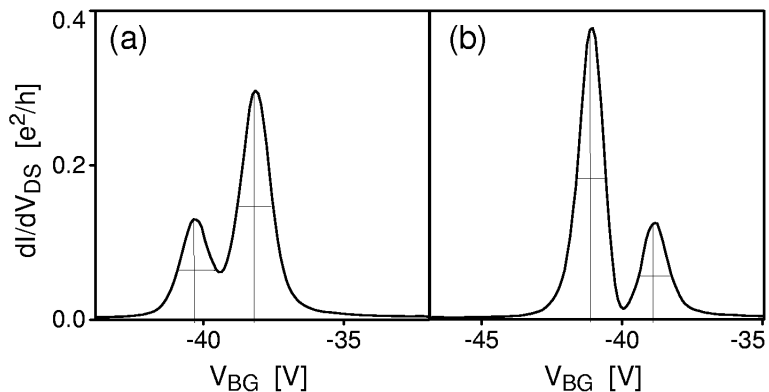


Figure 17: Differential conductance for (a)  $V_{DS} = 206 \mu\text{eV}$  and (b)  $V_{DS} = -194 \mu\text{eV}$ . The FWHM (full width at half maximum) of the peaks in the differential conductance are from left to right:  $108 \mu\text{eV}$ ,  $103 \mu\text{eV}$ ,  $92 \mu\text{eV}$ ,  $99 \mu\text{eV}$ .

## 2.7 Summary

In this chapter a quantum dot was studied for the case of weak tunnel-coupling to the leads. The constant interaction model for the energies of the quantum dot was introduced. In combination with the single-electron tunneling approximation it explains the observation of the Coulomb blockade effect — a characteristic suppression of transport due to a fixed number of electrons on the dot. The shape of these areas of suppressed conductance could be parameterized in terms of the constant interaction model. However, this model has already proven itself to be insufficient for the first excited state.

The tunnel-coupling between the quantum dot and the leads introduces a finite lifetime of the electrons on the dot. This leads to a broadening of the single-particle tunneling resonances which was modeled by Lorentzian shaped spectral densities. Using the sharp Fermi-edges of the leads for transport spectroscopy, these line-shapes could be studied. Even in the case of weak tunnel-coupling there were visible deviations from the symmetries expected in the — oversimplified — model of a single Lorentzian shaped resonance, which may be attributed to an excited state.

### 3 Resonances in the Coulomb blockade region

In the previous chapter the Coulomb blockade effect and transport spectroscopy were introduced. Here, we want to present observations that cannot be explained considering only single-electron tunneling. Peaks in the differential conductance that develop at low temperatures have previously been observed by Goldhaber-Gordon et al. [45]. This type of observation can be explained in terms of the Anderson impurity model as a correlation effect of the electrons on the quantum dot and in the leads [46, 47]. Simple arguments are presented that connect a feature at  $V_{\text{DS}} = 0$  with higher order transitions that involve the ground state.

In this chapter we want to introduce the phenomenology and emphasize the distinction from single-electron tunneling effects. A more detailed analysis will be done in Chapter 5 after the Anderson impurity model has been introduced in Chapter 4. It will become clear that these resonances are intimately related to the internal degree of freedom on the dot. This relation is studied in more detail in Chapter 6.

#### 3.1 Zero bias maximum for strong tunnel-coupling

It was already stated that the single-electron tunneling approximation and with it Coulomb blockade are limited to the case of high enough tunnel barriers. Glazman et al. and Ng et al. [46, 47] predicted a different type of deviation from single-electron tunneling in the case of a degenerate level on the dot. According to these predictions, deviations should become visible at low temperatures and strong tunnel-coupling prompting the following measurements.

The measurements of the differential conductance presented in Figure 18 are done at the base temperature<sup>1</sup> of 30 mK in a dilution refrigerator. Each set of data covers a voltage range of 30 V in the backgate voltage  $V_{\text{BG}}$ . However, the gate voltages defining the dot are chosen differently for each set of data as given in Table 1. With these parameters, the number of electrons on the dot is the same in the CB region shown in Figure 18(a)-(c), however, the height of the barriers is lowered from Figure 18 (a) to (c). This leads to a broadening of the single-electron peaks. The overall conductance increases with respect to (a).

As one can see in Figure 18(b) and more clearly in Figure 18(c), a new peak in the differential conductance develops at  $V_{\text{DS}} = 0$  V across the CB re-

---

<sup>1</sup>see measurement setup

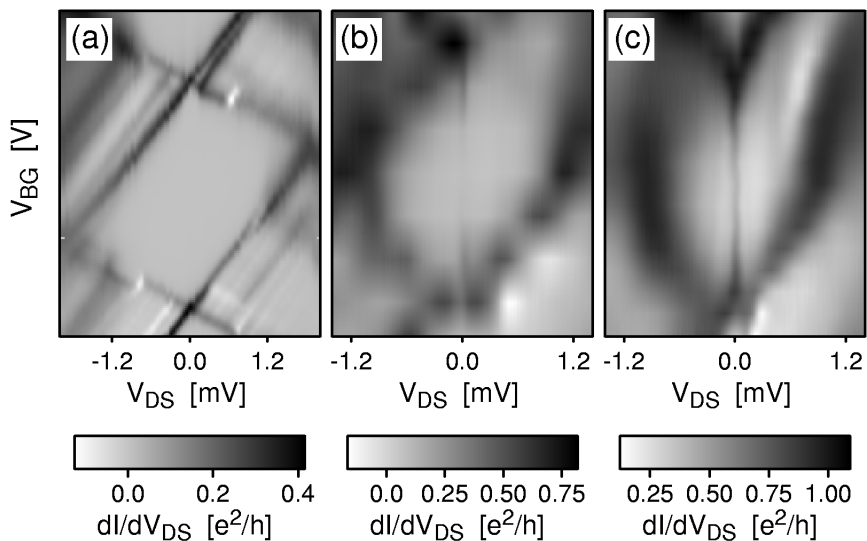


Figure 18: Differential conductance for the top gate voltages given in Table 1. The electron number is constant but the tunnel-coupling increases from (a) to (c). The range of the back-gate voltage is  $\Delta V_{BG} = 30$  V, the offset is given in Table 1.

	$V_{BG0}$	$V_L$	$V_M$	$V_R$
Figure 18(a)	-42 V	-0.625 V	-0.580 V	-0.621 V
Figure 18(b)	-33 V	-0.610 V	-0.658 V	-0.580 V
Figure 18(c)	-48 V	-0.585 V	-0.697 V	-0.560 V

Table 1: Gate voltage values for Figure 18.

gion. Single-electron tunneling introduced in the previous chapter predicted resonances that have two distinct slopes in the  $(V_G, V_{DS})$ -plane corresponding to an alignment of an addition energy with the electro-chemical potential of either the source or the drain lead. The maximum at  $V_{DS} = 0$ , therefore, requires a different explanation.

### 3.2 Deviation from single-electron tunneling

In the analysis of single-electron tunneling the main assumption that leads to the rhomb shaped areas of a stable electron configuration and vanishing conductance is:

*Electron configurations  $(N_S, N_i, N_D)$  are connected by a series of uncorrelated single-electron tunneling events  $\pm(0, 1, -1), \pm(1, -1, 0)$  and energy conservation is obeyed for each event.*

In non-equilibrium, i. e.  $V_{DS} \neq 0$ , any electron configuration is metastable. If one does not make the restriction to uncorrelated tunnel events, an infinite number of possible final states has to be considered when starting from the dot occupied with  $N$  electrons and applying energy conservation to the overall process:

$$0 = E_{N+\Delta N, F} - E_{N, I} + \sum_{i=0}^{|\Delta N_D|} \text{sgn}(\Delta N_D) \varepsilon_{D, i} + \sum_{i=0}^{|\Delta N_S|} \text{sgn}(\Delta N_S) \varepsilon_{S, i}.$$

In this equation  $\Delta N$  stands for the change in electron number on the dot,  $\Delta N_S, \Delta N_D$  for the changes in electron number in the source and drain leads. The electron number is conserved i. e.  $\Delta N + \Delta N_S + \Delta N_D = 0$ . Empty states in e. g. the drain leads are at  $T = 0$  available only at energies above the electro-chemical potential  $\varepsilon_{D, i} \geq \mu_D$  and occupied states only at energies below the electrochemical potential  $\varepsilon_{D, i} \leq \mu_D$ . When electrons are added to the drain lead in a process ( $\Delta N_D > 0$ ) one needs empty states, when electrons are removed ( $\Delta N_D < 0$ ) one needs occupied states, in both cases  $\text{sgn}(\Delta N_D) \varepsilon_{D, i} > \text{sgn}(\Delta N_D) \mu_D$  holds. Choosing  $\mu_S = 0$  one obtains

$$0 \leq E_{N+\Delta N, F} - E_{N, I} + \Delta N_D \mu_D.$$

Using the constant interaction model (equation 2) for the energies of the dot, considering only ground-state transitions and assuming  $\Delta N > 0$  one obtains:

$$V_G \leq \frac{(\Delta N_D / \Delta N) - c_D}{c_G} V_{DS} + e \frac{N + (\Delta N - 1) / 2}{C_G} - \Delta N \sum_i \frac{c_{i \notin \{D, G\}}}{c_G} V_i + \frac{E_0^{N+\Delta N} - E_0^N}{c_G}. \quad (21)$$

The inequality is inverted for  $\Delta N < 0$ . For  $\Delta N = 0$  the slope becomes infinite (there is a prefactor  $\Delta N_D / \Delta N$  in equation (21) before  $V_{DS}$ ) and the boundary coincides with the gate voltage number  $N$ . Again, the whole picture is periodic in the electron number  $N$ . Several examples of these boundaries are shown in Figures 19(a) and 20.

The result is that higher order transitions are possible in the region forbidden for single-electron tunneling. There is no region of stability against processes that do not change the number of electrons on the dot  $\pm(1, 0, -1)$ ,  $\pm(2, 0, -2)$ ,  $\dots$ . Not surprisingly, the instability changes from  $(1, 0, -1)$  to  $(-1, 0, 1)$  at  $V_{DS} = 0$  as can be seen in Figure 19(a), this coincides with the position of the new type of resonance.

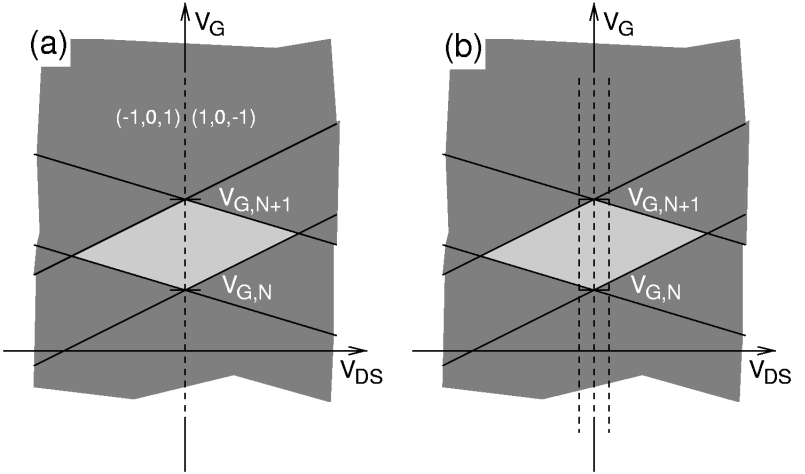


Figure 19: Regions of (in)stability of the  $N$ -electron system. Dark grey: instability against single-electron tunneling. Dashed lines correspond to two-barrier transitions: there is no region of stability against two-barrier tunneling. (a) Only the  $N$ -electron ground-state is considered. (b) The first excited state of the  $N$ -electron system leads to lines parallel to the  $V_G$ -axis at  $V_{DS} = \pm(E_{N,1} - E_{N,0})$ .

The boundaries of the region of instability against putting  $\Delta N \neq 0$  electrons on the dot have the same intercept with the gate voltage axis for each  $\Delta N$ , their slope depends on the number of electrons transferred from drain to source. This is depicted for some transitions in Figure 20(a) and (b). Three barrier transitions that change the electron number on the dot can fall into the region of stability against single-electron tunneling as can be seen in Figure 20(a).

It is important to note that these energy considerations cannot directly be put into a transport model and are only suggestive as to what may be important.

Thus far, we have only considered ground states. To introduce the effect of excited states, we assume for simplicity that there is one excited state of the  $N$ -electron system. This leads to an additional possibility of making a transition into this excited state as depicted in Figure 19(b) for finite voltages  $V_{DS}$ .

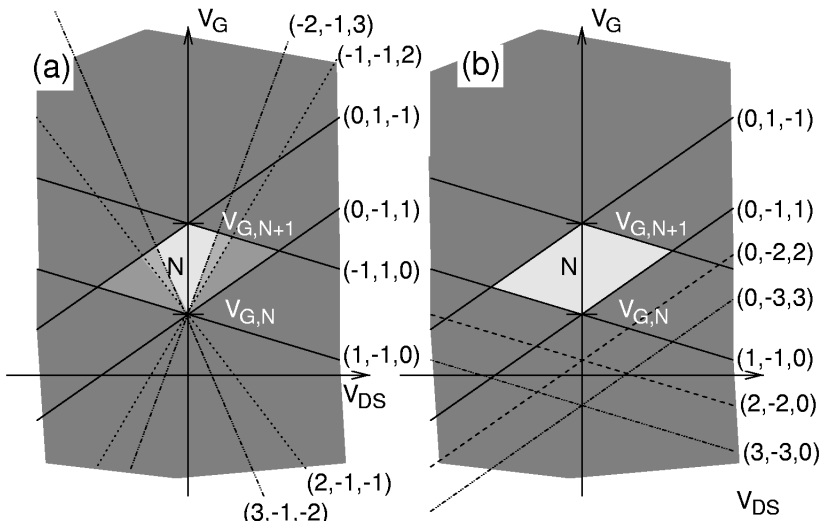


Figure 20: Regions of (in)stability of the  $N$ -electron system. Only ground-states are considered. Solid line: one barrier is tunneled; dashed line: two barriers; dotted lines: three barriers; dash-dotted: four barriers are tunneled. The relevant parameter  $c_D$  is chosen as 0.3. The other parameters in Equation (21) determine the scale and offset of the  $V_{DS}$  and  $V_G$  axis.

In conclusion, the position observed for the new resonance in Figure 18 in the  $(V_{DS}, V_G)$ -plane is characteristic for ground state transitions involving the same number of electrons on the dot.

### 3.3 Temperature dependence

In Figure 21, a Coulomb blockade region is shown at different temperatures. At 25 mK in Figure 21(a), a pronounced resonance is visible at  $V_{DS} = 0$ . This resonance has completely disappeared at  $T = 800$  mK in Figure 21(b) while the overall structure of Coulomb blockade is preserved.

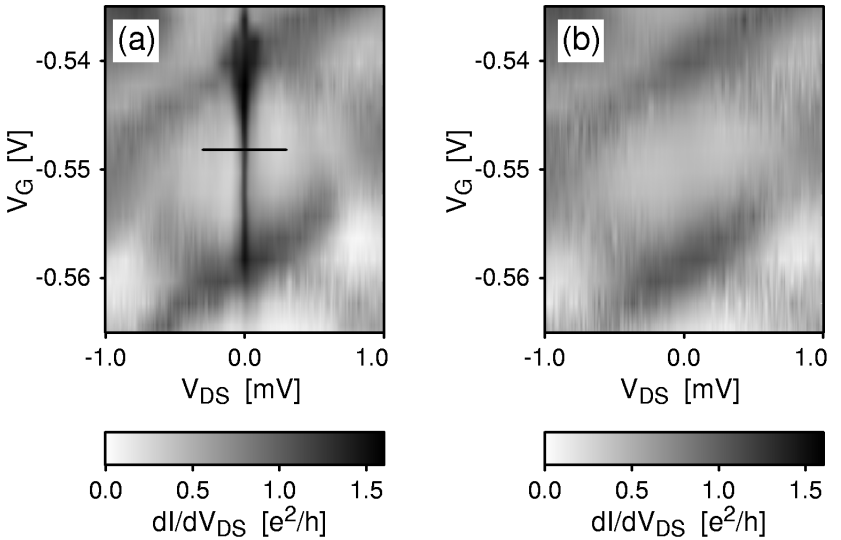


Figure 21: (a) CB region with a zero  $V_{DS}$  resonance at  $T = 25$  mK. (b) The same CB region at  $T = 800$  mK

In Figure 22(a), the same  $V_{DS} = 0$  resonances as in Figure 21 is shown (for a fixed  $V_G$  as indicated by the line in Figure 21(a)) at three different temperatures. This is compared to what one would expect for thermal broadening: The experimental curve for the lowest temperature in Figure 22(a) is broadened artificially by Fermi-functions at the indicated temperatures and the result is shown in Figure 22(b). The resonance disappears faster in the experiment, which cannot be explained by a temperature independent spectral density.

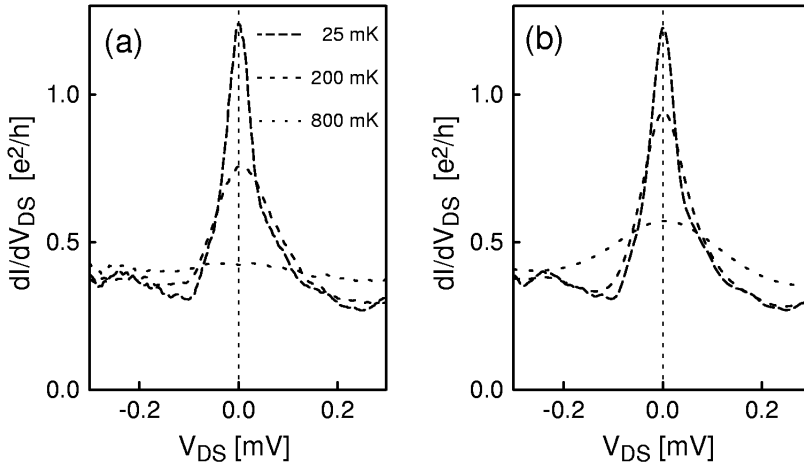


Figure 22: (a) Differential conductance for different temperatures at the gate-voltage indicated in Figure 21(a) by the horizontal line. (b) The curve for 25 mK in (a) broadened by a Fermi-distribution of the corresponding temperatures.

### 3.4 Splitting with magnetic field

This new type of resonance splits with a magnetic field applied parallel to the plane of the 2DES as seen in Figure 23; a similar splitting was also observed by Goldhaber-Gordon et al. and Cronenwett et al. [45, 48]. At finite fields, two resonances occur symmetrically around  $V_{DS} = 0$  parallel to the  $V_G$ -axis. This would be expected for a feature due to an excited state of the  $N$ -electron system as indicated in Figure 19(b). The fact that these resonances merge at  $V_{DS} = 0$  for a magnetic field of  $B = 0$  can be seen as an indication of a degeneracy on the dot for zero magnetic field.

### 3.5 Other features in the Coulomb blockade regime

In all cases where  $V_{DS} = 0$  resonances were observed, side-peaks were visible, as for the resonance in Figure 24(a). Sometimes these side-peaks were more pronounced as in Figure 24(b). A feature that was observed on two samples is a resonance in the Coulomb blockade regime that is not exactly parallel to the  $V_G$ -axis as shown in Figure 25. Similar observations have been reported by Simmel et al. [49].

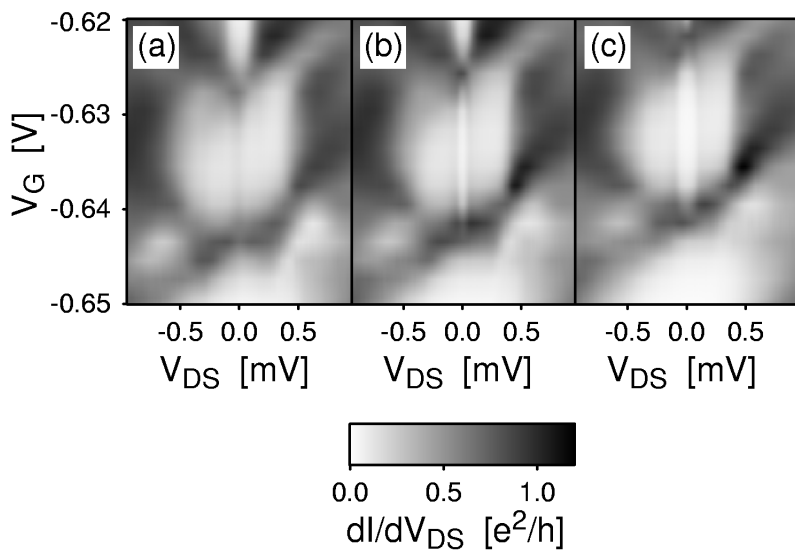


Figure 23: Splitting of a  $V_{DS} = 0$  resonance with a magnetic field  $B_{\parallel}$  in the plane of the 2DES (a)  $B_{\parallel} = 0$  T (b)  $B_{\parallel} = 2$  T (c)  $B_{\parallel} = 4$  T.

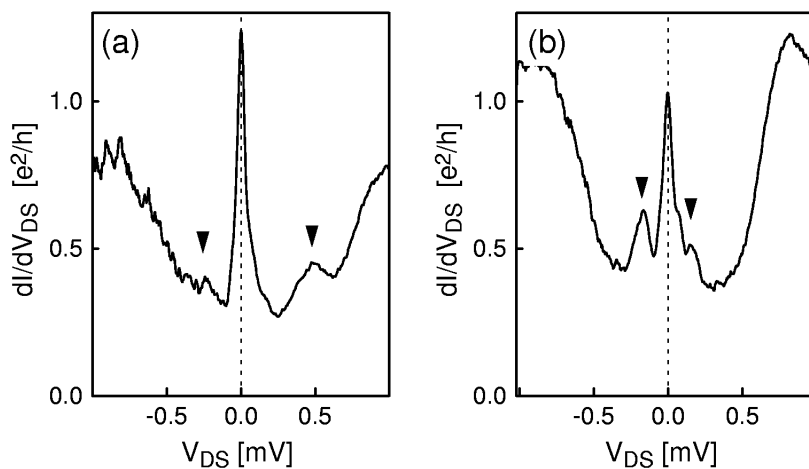


Figure 24: Side peaks for different  $V_{DS} \neq 0$  are marked by arrows.

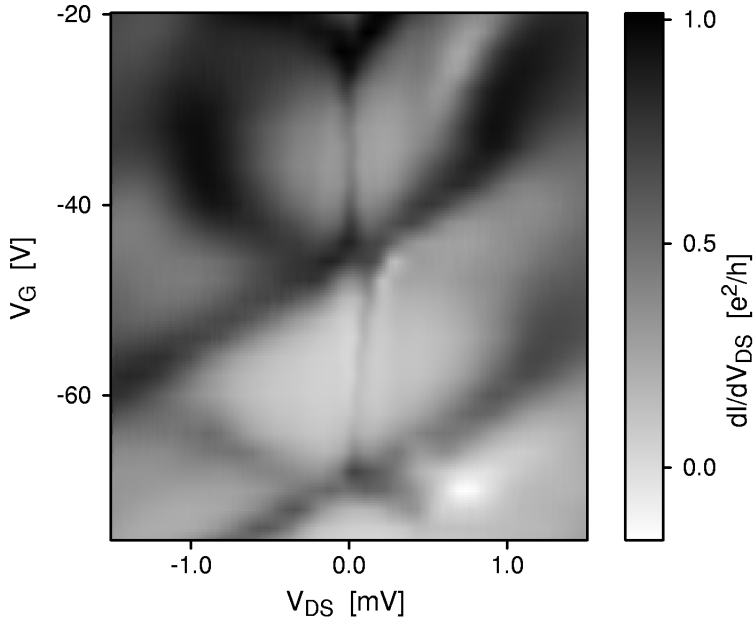


Figure 25: Two Coulomb blockade regions. The upper one shows a resonance at  $V_{DS} = 0$ , the lower one a similar resonance not exactly at  $V_{DS} = 0$  and changing with  $V_G$ .

### 3.6 Coulomb blockade lifted by strong tunnel-coupling

Of course the strength of the potential landscape for the electrons in the 2DES can be varied almost arbitrarily by using the top gates. This includes the possibility to generate potential landscapes that cannot at all be described by “tunnel-barriers” and a “dot”. The corresponding experiments are shown in Figures 26 and 27. For the most negative gate voltages in Figure 26, Coulomb blockade regions are visible whereas the pattern looks more irregular for more positive gate voltages and the overall conductance is high. There are still structures, that look like an inverted Coulomb blockade, i. e. regions of higher conductance are surrounded by “resonances” of lower conductance. The data in Figure 27 near the transition from closed dot to open dot show this more clearly, in particular Figure 27(b) shows a beautiful symmetry. The appropriate theories needed in the parameter-range of Figures 26 and 27 are unclear at this point, an approach for a situation of a localized level coupled to a free channel was given by Göres et al. [50].

This is an area in which further —especially theoretical work — is needed.

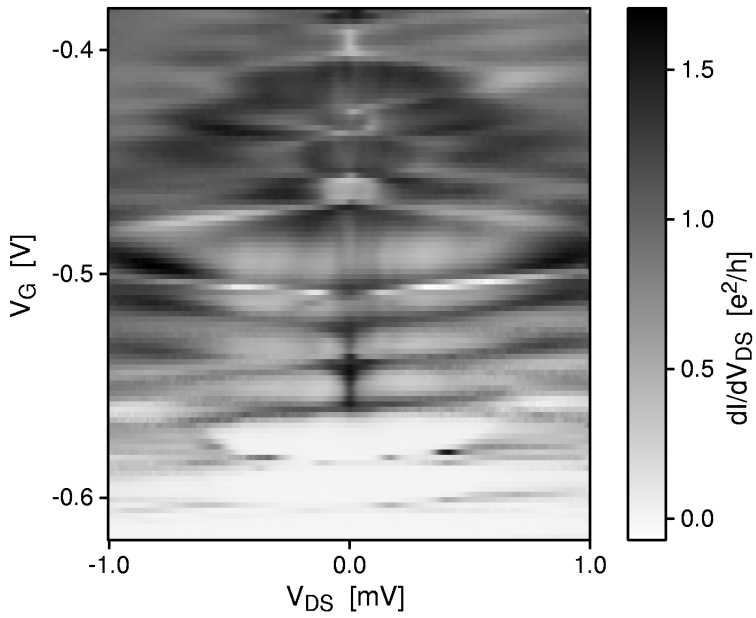


Figure 26: Differential conductance for a large gate-voltage range. For  $V_G > -0.5$  V the picture of an isolated island is no longer valid.

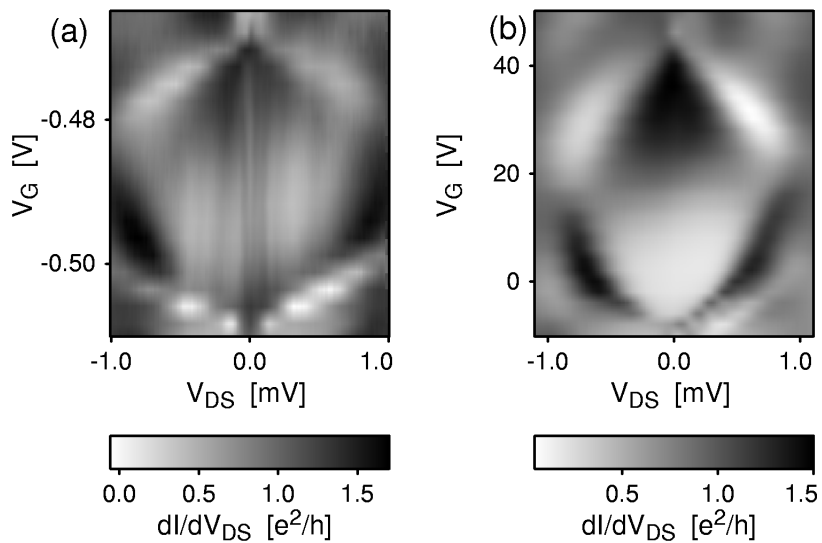


Figure 27: The transition between a dot and an open system. (a) Detail of Figure 26. (b) Similar point in a different quantum dot.

## 4 The Anderson Impurity model

In this section the Anderson Impurity Model [22] — with an extension to two reservoirs — is introduced and the predictions for this model are summarized. The applicability to our quantum dots is discussed and it is found that small quantum dots with large level spacing are needed to be able to observe Kondo resonances experimentally. The observation of resonances in the differential conductance at zero drain-source voltage reported in Chapter 3 can be interpreted as the Kondo resonances predicted for the Anderson impurity model.

### 4.1 History of the Anderson impurity model

The Anderson impurity model was introduced in 1961 to describe the effects of magnetic impurities embedded in non-magnetic metals (dilute magnetic alloys). This simple model describes one (spin-)degenerate level coupled to the conduction band electrons of the host metal and includes Coulomb interaction. The low-temperature anomalies found for the resistivity of these systems [51, 52] were first explained by Kondo in terms of correlations in the scattering from localized spins [53]. Schrieffer et al. [54] showed that the Anderson impurity model can be mapped to the Kondo model for appropriate parameters (the impurity has to be singly occupied for the mapping to work), thus the name “Kondo resonances” for the key prediction for the Anderson impurity model. Even though the Anderson impurity model has been studied by various methods, theoretical work is still in progress to make quantitatively accurate predictions.

This model could be equally successfully applied to tunnel-junctions with an ensemble of embedded impurities (see for example [55, 56]) and an experiment on a point contact with one single impurity was reported [57]. In 1988, Glazman, Raïkh, Ng and Lee [46, 47] came to the conclusion that this model could also be relevant for quantum dots, the quantum dot playing the role of a controlled impurity. Subsequently, a large number of theoretical papers worked out details of the Anderson impurity model applied to quantum dots. In 1998, the first observations of Kondo resonances for quantum dots were reported [45, 48, 58] and a scanning tunneling microscope (STM) experiment [59] was carried out on atoms adsorbed to a metal surface showing signatures of Kondo resonances.

What makes this model interesting is its simple Hamiltonian that, nevertheless, leads to non-trivial predictions which carry strong experimental

signatures: The main effect predicted is a resonance in the differential conductance at  $V_{\text{DS}} = 0$ , with a logarithmic temperature dependence for appropriate parameters. This effect is non-perturbative in the tunnel-coupling to the leads: For arbitrarily small tunnel-coupling the spectral density reaches unity as temperature approaches 0 K, in contrast to the system without tunnel-coupling, in which the spectral density is zero in this limit. This leads to a conduction of  $2e^2/h$  in the presence of tunnel-coupling and no conductance in the absence of tunnel-coupling. This fact can also be formulated differently: It is impossible to make a “non-invasive” measurement of a quantum dot by attaching leads.

## 4.2 The Hamiltonian of the Anderson impurity model

The Hamiltonian of the Anderson impurity model was introduced to describe a single spin-degenerate level tunnel-coupled to two reservoirs. It can be divided into a dot part  $H_{\text{d}}$ , a tunneling part  $H_{\text{t}}$ , and a reservoir part  $H_{\text{r}}$ . The dot part introduces the energies  $\varepsilon_{\pm 1/2}$  for the spin degenerate level and the Coulomb energy  $U$  in the case of double occupancy. The tunneling part introduces the tunnel matrix elements  $t_{rks}$  that parameterize the exchange of electrons between dot and reservoirs. The reservoirs are described as a set of closely spaced levels at the energies  $\varepsilon_{rks}$ ; Coulomb interaction between electrons in the reservoirs is neglected. The formal expression is:

$$H = H_{\text{d}} + H_{\text{t}} + H_{\text{r}} , \quad (22)$$

where

$$\begin{aligned} H_{\text{d}} &= \sum_s \varepsilon_s c_s^\dagger c_s + U c_{1/2}^\dagger c_{-1/2}^\dagger c_{1/2} c_{-1/2} , \\ H_{\text{t}} &= \sum_{rks} t_{rks} a_{rks}^\dagger c_s + h.c. , \\ H_{\text{r}} &= \sum_{rks} \varepsilon_{rks} a_{rks}^\dagger a_{rks} . \end{aligned}$$

This Hamiltonian is depicted schematically in Figure 28. The indices  $r$  stand for S, D, i.e. electrons in the source and drain reservoirs.  $k$  is a momentum index that counts the states in the reservoirs. The index  $s$  stands for a spin index which can take the values  $\pm 1/2$ . The electron spin is conserved in this Hamiltonian; nevertheless, the Coulomb interaction on

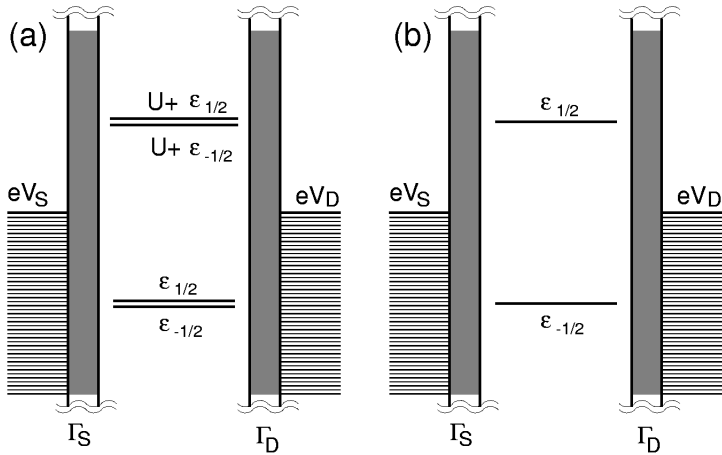


Figure 28: Schematic Anderson impurity model for different parameters. The dark areas stand for the tunnel-barriers. The closely spaced horizontal lines on the left and right side represent the closely spaced levels in the reservoirs that are filled with electrons. The vertical axis is an energy axis. (a) The double lines in the middle symbolize the addition energies of a spin degenerate level with Coulomb interaction on the dot. (b) The lines in the middle symbolize the addition energies into non-degenerate levels in the absence of Coulomb interaction.

the impurity site couples electrons with different spin. Even though  $s$  was introduced as a spin index, the Hamiltonian does not make explicit use of the  $s$  being related to spin and the prediction are directly applicable to any system with two localized levels, interaction and two separate electron populations [60, 61]. One example for a different realization is a system with two electrostatically coupled quantum dots that is studied in [62].

In addition to the Hamiltonian one has to specify the distribution functions for the electrons in the source and drain reservoirs. These are Fermi functions corresponding to the temperature  $T$  with the electro-chemical potential determined by the applied voltage  $V_T$ :

$$\langle a_{rks}^\dagger a_{rks} \rangle = f_F(\varepsilon_{rks} + eV_T/k_B T).$$

This expectation value is not influenced by the existence of the dot, i. e. the reservoirs are assumed to be large enough to “swallow” all the excitations coming from the dot.

The Hamiltonian still has a large number of parameters  $\varepsilon_{rks}$  and  $t_{rks}$ . These can be combined in the following way into the transparencies  $\Gamma_{rs}$  of the barriers:

$$\Gamma_{rs} = 2\pi \sum_{ks} |t_{rks}|^2 \delta(\varepsilon_{ks}/\hbar - \omega).$$

Note that the argument  $\omega$  on the right side of this equation does not appear on the left side, corresponding to the assumption of an energy independent product of tunnel-coupling and density of states.

The model given here differs from the original Anderson impurity model [22] with the presence of two reservoirs. In the case that these are not at the same voltage, it is possible to study the model out of equilibrium. For  $V_{DS} = 0$  the original model is recovered, the reservoir index has no meaning.

### 4.3 Spectral density

The spectral density  $A_s(\omega)$  can be understood as a local density of states, i.e. the answer to the question “Can an electron with spin  $s$  be put onto the island or removed from the island at the energy  $\hbar\omega$ ?”. It can be defined in terms of the operators given in the previous section [44]. It reduces to the addition spectrum in Figure 28 in the absence of tunnel-coupling (the lines standing for  $\delta$ -functions) and forms the bridge to the single-electron-tunneling picture given in Chapter 2

$$A_s(\omega) = \frac{1}{2\pi} \int_{-\infty}^{\infty} dt e^{i\omega t} \langle c_s^\dagger(t)c_s(0) + c_s(t)c_s^\dagger(0) \rangle.$$

For a non-interacting system (Figure 28(a)), this quantity is independent of the distribution functions of the reservoirs, for an interacting system — as is the case in the experiments — it is not.

The spectral density is closely related to the current [44]:

$$I_{DS} = \sum_s \frac{e}{\hbar} \int_{-\infty}^{\infty} d\omega \frac{\Gamma_R \Gamma_L}{\Gamma_R + \Gamma_L} (f(\omega + eV_S/\hbar) - f(\omega + eV_D/\hbar)) \times A_s(\omega), \quad (23)$$

a relation already used in Chapter 2 and depicted in Figure 29.

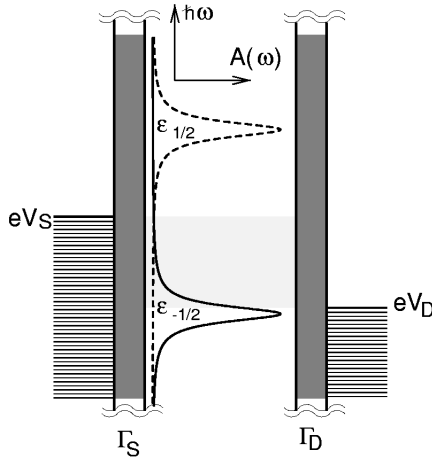


Figure 29: Graphical representation of Equation (23). At zero temperature the integration is restricted to the shaded area due to the Fermi functions and picks up the weight of the spectral densities that falls into this area. There is an additional pre-factor due to the transparencies of the left and right barrier.

#### 4.4 Properties for different parameter sets

Here we compare solutions for limiting parameter sets with the single-electron-tunneling approximation. In the first case, we assume that the

Coulomb energy does not contribute to the energy gap  $E_G$  between adding the first and the second electron. In the second case, we assume that the Coulomb energy is the only energy contributing to this energy gap. In reality, the energy gap can have contributions from both Coulomb energy and the spin degree of freedom. This is the last case studied.

The model is valid for an arbitrary choice of units for the energy, we have chosen to use parameters and units that correspond to our experimental parameters. Moreover, we have chosen the point of zero energy by setting  $\mu_S = 0$ .

#### 4.4.1 System without interaction $U = 0$ and finite level splitting $\Delta\varepsilon \neq 0$

This case — depicted in Figure 28(b) — is somewhat artificial because in the experiments the Coulomb energy is the largest energy scale. Still, it is instructive to compare the conductances for different approximations [44] as presented in Figure 30. In these plots, the conductance is given as a function of the level positions  $\varepsilon_{\pm 1/2}$ , the linear dependence on  $V_G$  corresponds to the experimental situation.

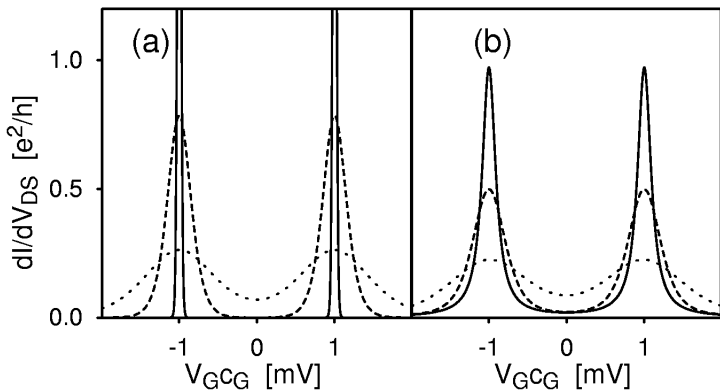


Figure 30: Conductance through an Anderson impurity for the following parameters:  $U = 0$  meV,  $\varepsilon_{1/2} = 1$  meV +  $e c_G V_G$ ,  $\varepsilon_{-1/2} = -1$  meV +  $e c_G V_G$ ,  $\hbar\Gamma_L = \hbar\Gamma_R = 0.1$  meV. (a) Conductance in the single-electron-approximation for the temperatures  $T = 0.01$  meV/ $k_B = 116$  mK (solid),  $T = 0.1$  meV/ $k_B = 1.16$  K (dashed),  $T = 0.3$  meV/ $k_B = 3.48$  K (dotted), (b) exactly calculated conductances for the same parameters.

It is immediately evident, that the main feature, i. e. the suppressed conductance for  $V_{DS} = 0$  in the gate voltage range  $c_G V_G$  between  $-1$  mV and  $1$  mV is present in both the exact solution and the single-electron tunneling approximation. This suppression corresponds to the energy gap between adding the first and the second electron. In this situation one electron on the dot forms a stable dot configuration as can be seen in comparison with Figure 31.

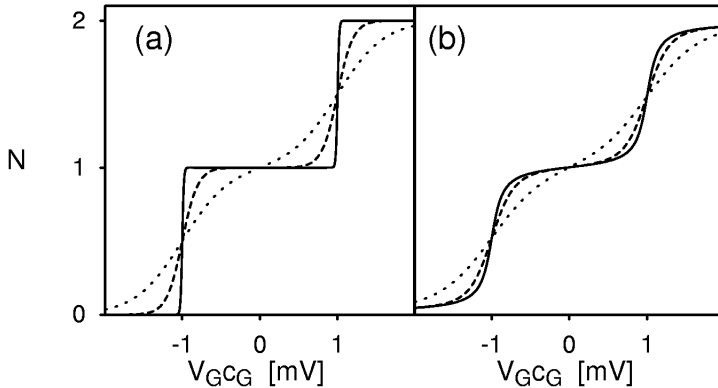


Figure 31: Expectation value for the number  $N$  of electrons on the dot. The parameters and approximations are the same as in Figure 30.

The single-electron-tunneling approximation fails most noticeably close to the single-particle tunneling resonances when the temperature becomes small compared to the tunnel-coupling  $\Gamma$  (solid lines in Figure 30). The exact solution consists of two Lorentzian lines with a maximum of  $1e^2/h$  and a broadening of  $\hbar\Gamma$ , whereas the peaks in the single-electron-tunneling-approximation have a width determined solely by the temperature and approach  $\delta$ -functions as the temperature goes to zero. Thus in this case, the tunnel-coupling  $\Gamma$  is the energy scale below which the single-electron approximation breaks down.

The result can also be understood in terms of the spectral densities  $A$ . These can be described by one curve for  $A_{1/2}$  and one for  $A_{-1/2}$  shifting linearly with  $V_G$ . This is shown in Figure 32. In addition to this symmetry, the spectral densities are independent of temperature and of the position of the electro-chemical potential of the drain reservoir  $\mu_D$ .

The Fermi edges of the reservoirs only determine the resolution with

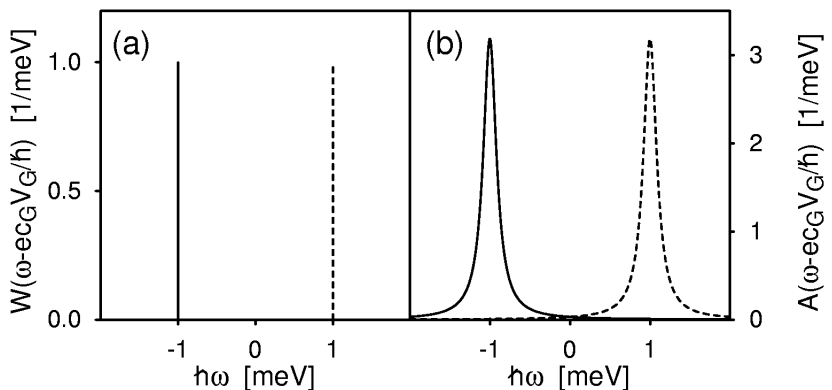


Figure 32: Spectral densities for the parameters given in Figure 30 (dashed corresponds to spin  $1/2$ , solid to spin  $-1/2$ ). The spectral densities in the single-electron-approximation are  $\delta$ -functions, in (a) their weight  $W_s(\omega) = \int_{\omega-\tau}^{\omega+\tau} dx A_s(x)$  ( $\tau$  is an infinitesimal quantity) is plotted over their position. In (b) the exact spectral densities are given, they are Lorentz curves at the energies of the level.

which the spectral densities are probed. At  $T = 0\text{K}$  no broadening is introduced and in the exact solution the sum of the spectral densities  $A_{1/2}(\omega) + A_{-1/2}(\omega)$  and the conductance are the same except for a prefactor and a scale  $ec_G$  that maps the energy axis  $\hbar\omega$  to the gate voltage axis.

#### 4.4.2 Coulomb gap $U \neq 0$ and degeneracy $\varepsilon_{1/2} = \varepsilon_{-1/2}$

The energy gap  $E_G = U$  is chosen to have the same value as before and the level is assumed to be degenerate, i.e.  $\varepsilon_{1/2} = \varepsilon_{-1/2}$ , which is the “classical” situation for the Anderson impurity model as depicted in Figure 28(a). In Figure 33, conductances at finite temperatures calculated in the single-electron tunneling approximation are compared to zero temperature results obtained from Friedel’s sum rule [63, 64]. The single-electron approximation yields qualitatively the same result as in the case of a single-particle gap  $E_G = \Delta\varepsilon$ . There are quantitative differences: The conductance is higher and the peak position shifts with temperature in Figure 33(a).

The exact result differs, however, in a non-intuitive way from the single-electron approximation. At zero temperature and  $V_{\text{DS}} = 0$ , Kawabata [64]

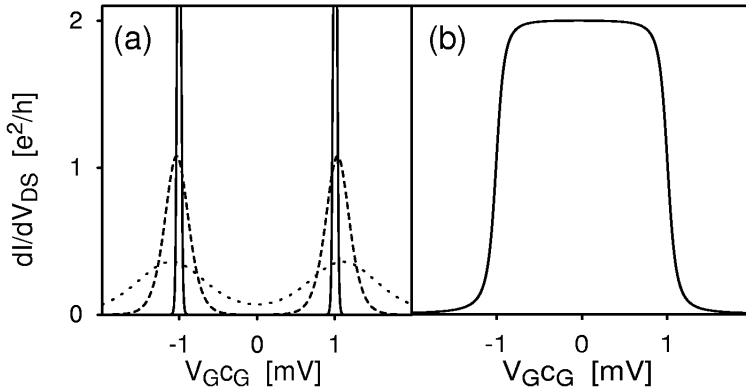


Figure 33: Conductance through an Anderson impurity for the following parameters:  $U = 2 \text{ meV}$ ,  $\varepsilon_{1/2} = \varepsilon_{-1/2} = -1 \text{ meV} + e c_G V_G$ ,  $\hbar\Gamma_L = \hbar\Gamma_R = 0.1 \text{ meV}$ . (a) In the single-electron approximation for the temperatures as given in Figure 30. (b) According to Equation (24) at  $T = 0$  with the electron number  $\langle N \rangle$  taken from the non-interacting case.

obtained for the conductance or equivalently for the differential conductance

$$dI/dV_{DS} = \frac{2e^2}{h} \cos^2\left\{\frac{\pi}{2} + \frac{\pi}{2} \langle N \rangle\right\}. \quad (24)$$

This means the system is perfectly conducting over a parameter range where the dot is occupied by one electron. One would expect a Coulomb gap and vanishing conductance in the single-electron approximation as seen in Figure 33(a) for this parameter range. To evaluate the Equation (24) one still needs the expectation value of the electron number  $\langle N \rangle$ . To get the qualitative picture of Figure 33(b) as an illustration, the values for  $\langle N \rangle$  of the non-interacting case were taken. This gives, qualitatively, the correct behavior, but more accurate calculations show [65] that the single-particle resonances are shifted (“renormalized”) slightly due to the correlations, leading to a narrower parameter range of perfect conduction.

This property of the model can be overlooked [22] if one does not include correlations between tunneling events in the calculations. These correlations introduce a new temperature scale and lead to so-called Kondo resonances that are pinned to the Fermi-energies of the reservoirs.

Again, this can be discussed in terms of spectral densities; however, the form of spectral densities is no longer independent of the level position.

Spectral densities for three values of the level position are depicted in Figure 34, both in the single-electron approximation and in an approximation that takes higher order processes into account [66].

If the energy  $\varepsilon$  of the level is larger than the Fermi energy, the spectral density has one peak at the position of this level, both in the single-electron approximation (Figure 34(a)) and broadened in the more accurate calculation shown in Figure 34(b). In this situation, the number of electrons on the dot is zero and the peak position corresponds to the energy for adding the first electron. At the energy for adding a second electron  $\varepsilon + U$ , which would be at 2.8 meV in this example, there is no spectral weight due to the fact that it is unlikely to find the dot singly occupied.

For the energy range  $-U/2 < \varepsilon < 0$ , the minimum of energy corresponds to the singly occupied dot. In this situation, it is possible to remove an electron paying the energy  $|\varepsilon|$  or to add an electron paying the energy  $U + \varepsilon$ . Accordingly, there are two peaks in the spectral densities as can be seen from Figures 34(c) to (f). However, there is an additional peak in the more accurate calculation of Figure 34(d) and (f) that is not present in the single-electron approximation. This peak is called Kondo resonance, it develops at low temperatures and is pinned to the Fermi energies of the reservoirs (at  $\omega = 0$  in Figure 34). This property makes it easy to distinguish from the single-particle resonances: A Kondo resonance is expected at  $V_{\text{DS}} = 0$  for a degenerate  $N$ -electron system, in contrast to the single-particle resonances with a position  $V_{\text{DS}}$  that depends on the level energy, i. e. the gate voltage in the experiment.

#### 4.4.3 Master equation for the Anderson impurity model

The case of a degenerate level with Coulomb interaction is the most interesting one. We want to mention some simple results for sequential tunneling that are necessary for the evaluation of our experimental data. The idea is that at high temperatures or high drain-source voltages electron correlations can be neglected and one can use the results from the single-electron approximation to extract the model parameters.

The master equation for the Anderson impurity model in the case of  $\mu_{\text{S}} < \mu_1 < \mu_{\text{D}} < \mu_2$  reads:

$$\begin{aligned} \text{d} p_0 / \text{d} t &= \Gamma_{\text{S}} p_{1/2} + \Gamma_{\text{D}} p_{-1/2} - \Gamma_{\text{D}} p_0 \\ \text{d} p_{1/2} / \text{d} t &= -\Gamma_{\text{S}} p_{1/2} + \Gamma_{\text{D}} p_0 \\ \text{d} p_{-1/2} / \text{d} t &= -\Gamma_{\text{S}} p_{-1/2} + \Gamma_{\text{D}} p_0 \end{aligned}$$

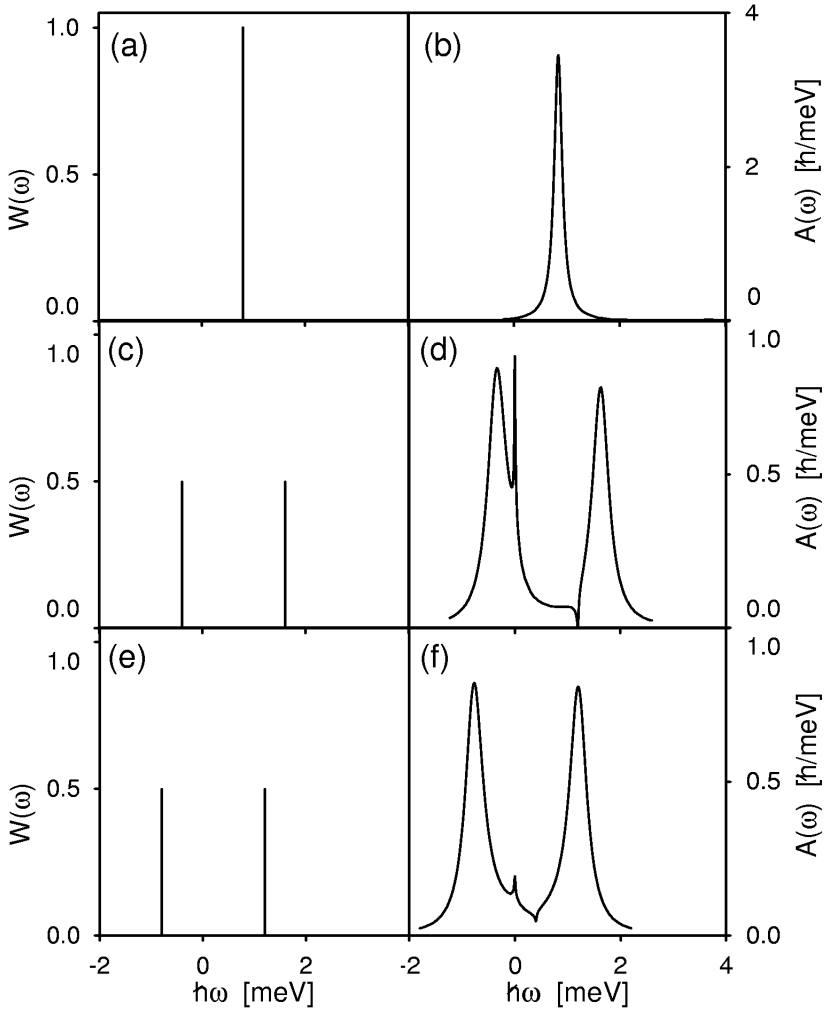


Figure 34: Spectral densities for the parameters given in Figure 33 for different values of the level energy  $\epsilon$  (a, b:  $\epsilon = 0.8 \text{ meV}$ ; c, d:  $\epsilon = -0.4 \text{ meV}$ ; e, f:  $\epsilon = -0.8 \text{ meV}$ ). The spectral densities for both spins are the same due to the degeneracy. (a, c, e) Single-electron tunneling approximation. (b, d, f) Approximation used in [66].

which leads to the probability  $p_{1/2}$  of finding the dot occupied by an electron with spin 1/2 of:

$$p_{1/2} = \frac{\Gamma_D}{\Gamma_S + 2\Gamma_D}.$$

Due to symmetry  $p_{1/2} = p_{-1/2}$  and with the normalization  $1 = p_0 + p_{1/2} + p_{-1/2}$  one gets  $p_0 = 1 - 2p_{1/2}$ . The current for negative source drain voltage is:

$$I_- = -2e\Gamma_S p_{1/2} = -e \frac{2\Gamma_S \Gamma_D}{\Gamma_S + 2\Gamma_D}. \quad (25)$$

The current  $I_+$  for the opposite polarity has the different sign and the indices S and D are interchanged. The absolute value of the current  $I_+$  is not the same as  $I_-$ , if  $\Gamma_S$  and  $\Gamma_D$  differ (in contrast to the case of a single level). In the case of a degenerate level, the measurement of  $I_-$  and  $I_+$  can be solved for  $\Gamma_S$  and  $\Gamma_D$ :

$$\Gamma_S = -\frac{3}{2e} \frac{I_- I_+}{2I_+ - I_-} \quad (26)$$

and

$$\Gamma_D = -\frac{3}{2e} \frac{I_- I_+}{2I_- - I_+}. \quad (27)$$

If  $I_- = I_+$  one can conclude that the barriers have the same height and one obtains

$$\Gamma = \Gamma_S + \Gamma_D = 3 \frac{I}{e}.$$

#### 4.4.4 Spectral densities in the Anderson impurity model

While neglecting correlation effects, one still has to include occupation effects. One can presume that for high energies ( $V_{DS}$ ,  $T$ ) the spectral density can be described using Lorentzian line shapes:

$$A_s(\omega) = (p_0 + p_s) \frac{1}{\pi} \frac{\Gamma/2}{(\omega - \mu_N/\hbar)^2 + (\Gamma/2)^2}. \quad (28)$$

The pre-factor due to the occupation probabilities changes when one goes through a single-electron resonance. When the dot is empty the pre-factor is 1. In the situation of Figure 28(a), the pre-factor is given by the occupation probabilities  $p_0$  and  $p_{1/2}$ , which can as the simplest approximation be taken from the master equation above. If the dot is occupied by one electron the pre-factor is 0.5, because spin up and spin down have the same probability.

#### 4.4.5 Finite Coulomb interaction and finite level splitting

The situation where  $U \neq 0$  and  $\varepsilon_{1/2} \neq \varepsilon_{-1/2}$  is the most general case of this model. It leads to an energy gap  $E_G = U + |\varepsilon_{1/2} - \varepsilon_{-1/2}|$  for the isolated dot. In this case, correlation effects are also important and Kondo resonances develop, but the position of the Kondo resonances is shifted off the electrochemical potential by  $\pm\Delta\varepsilon$ . The resonances are only visible in non-equilibrium which can be achieved when two reservoirs are connected to the dot [67, 68]. Therefore, the extension of the Anderson impurity model to two reservoirs is crucial.

### 4.5 Non-equilibrium properties and finite temperatures

The calculations are more difficult in this case and one has to keep in mind that all theoretical results are approximations. A number of different methods, including the non-crossing approximation [69], equation of motion technique [67] and a re-summation technique [70, 68] give qualitatively the same results, so that there is no serious doubt about the qualitative behavior. In this section the results are discussed in terms of the spectral density of the dot, which is closely related to the differential conductance.

#### 4.5.1 Temperature dependence

As mentioned above, a new energy or temperature scale appears in the solution of the Anderson impurity model. This so-called Kondo temperature is given by Haldane [71] as:

$$k_B T_K = \frac{1}{2}(U\hbar\Gamma)^{\frac{1}{2}} \exp\left(\pi \frac{\varepsilon(U + \varepsilon)}{\hbar\Gamma U}\right) \quad (29)$$

for  $\varepsilon < 0$  and  $U + \varepsilon > 0$ . This temperature is not related to a phase transition, but rather to a smooth transition and in the original work there is no equality, but a proportionality in Equation (29). It has become a common practice [65, 72, 73] to quote Haldane [71] and write an equality in Equation (29). This should be seen as a definition of the Kondo temperature in the sense that it is possible to choose other definitions that differ by a pre-factor on the order of 1. The general and important feature is, though, that the Kondo temperature depends exponentially on the inverse lifetime  $T_K \propto \exp\{-1/\Gamma\}$  and on the level position  $T_K \propto \exp\{\varepsilon(U + \varepsilon)/U\}$  which reduces to  $T_K \propto \exp\{\varepsilon\}$  in the case of infinite  $U$  that is used for many calculations.

The most interesting parameter range is the one, in which the system is in the Coulomb blockade regime at “high” temperatures, i. e.  $\{\hbar\Gamma, k_B T\} \ll \min\{\varepsilon, U - \varepsilon\}$ . In this regime one expects no conductance at “high” temperatures  $T \gg T_K$  and perfect conductance at low temperatures. An approximate equation that was given by Hamann [74] (4.3) interpolates between these regimes for the spectral densities. For a twofold degeneracy it reads

$$A(0) \propto \frac{1}{2} \left( 1 - \frac{\ln \frac{T}{T_{KH}}}{\sqrt{(\ln \frac{T}{T_{KH}})^2 + \frac{3}{4}\pi^2}} \right). \quad (30)$$

This equation was derived from a perturbative approach and should be accurate for higher temperatures  $T > T_K$ , the continuation to temperatures  $T < T_K$  is not necessarily correct. At lower temperatures, Nozières [75] suggested a Fermi liquid description of the problem that leads to the following equation for temperatures much lower than  $T_K$ :

$$A(0) \propto \left( 1 - \frac{\pi^4 T^2}{16 T_K^2} \right)^{-1}. \quad (31)$$

A numerical treatment of the crossover has been introduced by Krishnamurthy, Wilkins and Wilson [76, 77] under the name “numerical renormalization group”. More recent numerical results for the transport coefficients are available from Costi et al. [65]. From this work we take  $T_{KH} = T_K/1.2$  and also the factor  $\pi^4/16$  in Equation (31) (Equation 44 in [65]).

The most important result of these theories is that in the Kondo regime the Kondo temperature is the only relevant energy scale, meaning that one expects a universal behavior of the spectral density  $A(0)$  as function of a reduced temperature  $T/T_K$ .

#### 4.5.2 Finite bias voltage

Finite bias voltage corresponds to the situation where  $\mu_S \neq \mu_D$  and represents a true extension of the original model. It was found by several works [78, 72], that in this case a Kondo resonance develops at the position of both electro-chemical potentials for low temperatures. There is no simple relation between the observed differential conductance and the spectral density, still, the Kondo resonance has a finite width and if the Kondo temperature

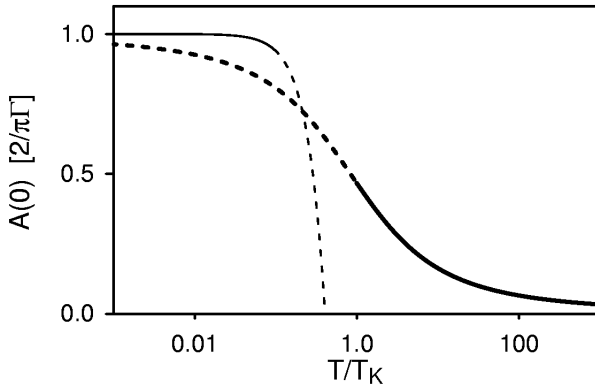


Figure 35: Different approximations for the spectral density  $A$  at  $\omega = 0$  as function of the reduced temperature  $T/T_K$ . This curve is called universal because it does not depend on the individual model parameters  $\Gamma$ ,  $U$  and  $\varepsilon$ . The thick curve represents Equation (30), the thin curve Equation (31). The dashed parts of the curves represent the parameter range where the respective approximations are not valid.

is the only remaining energy scale for  $T \rightarrow 0$  this width is determined by the Kondo temperature.

## 4.6 Extension to multiple states

This extension is relevant for our experiments because we definitely have more than one (nearly degenerate) state. It has been theoretically studied in [79, 80, 81, 82]. However, the number of parameters to model a multi-state system increases rapidly and is different from dot to dot and electron number to electron number. The predictions are not very surprising, additional levels lead to Kondo resonances at  $V_{DS}$ -values corresponding to the respective energy differences. Thus, we concentrate on the  $N$ -electron systems that can be understood in terms of one nearly degenerate state like in the Anderson impurity model and keep in mind that the model will not be applicable for higher energies (large  $V_{DS}$ ,  $T$ ).

## 4.7 Application to quantum dots

The first way to map the Anderson impurity model to quantum dots is by assuming that there is a degeneracy (or near degeneracy) of the ground state

of the  $N$  electron system on the dot. In this case it makes sense to neglect all other excited states at higher energies and the Anderson impurity model is recovered. The parameters are identified in the following way:

$$\begin{aligned} \mu_{N,0} &\equiv \varepsilon_{-1/2}, \\ \mu_{N,1} &\equiv \varepsilon_{1/2}, \\ \Gamma_r &\equiv \Gamma_r, \\ U &\equiv \mu_{N+1} - \mu_N. \end{aligned}$$

This is shown in Figure 36. The electron number  $N$  on the dot is identified with the electron number 1 of the Anderson impurity model. The approximation consists of neglecting all but the two lowest lying states of the  $N$ -electron system. These are indicated by dotted lines in Figure 36(b).

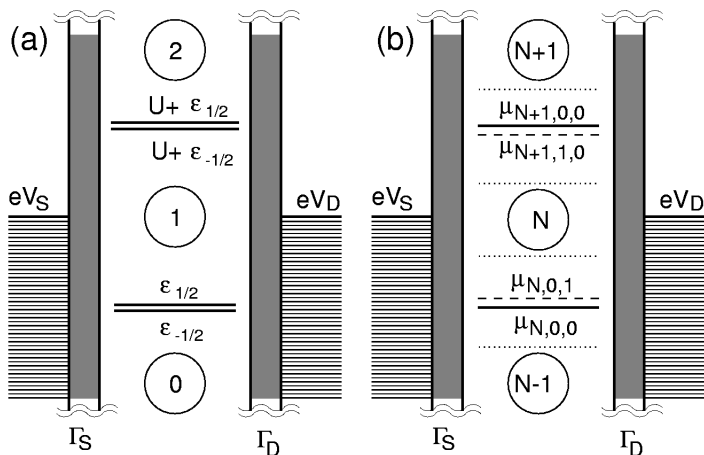


Figure 36: Mapping between the Anderson impurity model (a) and a quantum dot (b). The excited states of the dot that are neglected are shown as dotted lines.

There is a second way to do the mapping: Assume that there is one (strongly) tunnel-coupled spin-degenerate level on the dot and that for all other levels the coupling is exactly zero. Then the Anderson model is implemented exactly, with the peculiarity that the occupation of all the other levels depends on the initial condition.

This case is the academic limit of a realistic situation. We will see in Chapter 6 that the tunnel-coupling can be very different for different levels.

### 4.7.1 Relation of the spectral density to the observed differential conductance

The relation of the spectral density  $A$  to the observed quantity  $dI/dV_{DS}$  is given by Equation (16). The second term in this expression contains information about  $A$  at different energies making it impossible to solve this equation for  $A$  except in the special case that the second term vanishes. This happens for  $\mu_S = \mu_D$  and also when the derivative of the spectral density is zero i. e.  $dA/d\mu = 0$ . For a Kondo resonance at the position of the chemical potentials, one obtains the simple form from Equation (17):

$$A(0) = \frac{\hbar}{e^2} \frac{\Gamma_S + \Gamma_D}{\Gamma_S \Gamma_D} dI/dV_{DS}. \quad (32)$$

## 4.8 Observability of the signatures

For the signatures of the above-mentioned properties of the Anderson model to be observable, two conditions have to be met:

- *There is a degeneracy on the dot.*  
This cannot be expected for every electron number  $N$ ; the nature and occurrence of degeneracies will be discussed in detail in the experimental sections in Chapters 5 and 6.
- *The temperature is below the Kondo temperature.*  
This requirement is more stringent than it seems at first. The Kondo resonances are predicted for any set of parameters and low enough temperatures, but what is low enough depends exponentially on the tunnel-coupling as can be seen from Equation (29).

To give an example, the parameters used in Figure 33 would result in a Kondo temperature — in the middle of the Coulomb gap — of  $T_K \approx 1.4$  mK, well below the experimentally accessible range of  $\approx 50$  mK. A better chance of observing Kondo resonances is given close to the single-particle resonances, for  $\varepsilon = -0.4$  meV the Kondo temperature is already  $T_K \approx 24$  mK (getting closer to the single-particle resonance would mean that the effect is obscured by the single-particle resonance). This means, that for a given experimentally accessible temperature, the tunnel-coupling has to be large, on the order of  $\Gamma = 0.4$  meV, to obtain Kondo temperatures of  $T_K \approx 100$  mK.

Even though  $\Gamma$  is a continuously tunable parameter in the experiment, the condition for charge quantization  $\hbar\Gamma < \Delta\varepsilon$  due to Heisenberg's uncer-

tainty relation where  $\Delta\varepsilon$  is the “average” level spacing limits the useful range for  $\Gamma$  and makes small quantum dots with large  $\Delta\varepsilon$  necessary.

## 4.9 Deviations from the model

There is a number of reasons why the sample we study is not a clean realization of the Anderson impurity model. These reasons are summarized in the following:

- **Distribution function:** The distribution functions for the electrons in the leads may deviate from a Fermi distribution due to experimental imperfections and due to insufficient relaxation close to the barriers. This is especially relevant for high perpendicular magnetic fields, where the reservoirs shrink to few one-dimensional channels.
- **Spin conservation** — as assumed in the model — may not be perfect. In the Anderson impurity model there is no term that changes the number of electrons with a certain spin, i. e. spin is conserved. In reality, an electron on the dot may be able to flip its spin, e. g. due to interaction with other electrons or the nuclei.
- **Tunnel-coupling:** Assuming an energy independent tunnel-coupling  $\Gamma$  is wrong for two reasons. The density of states in the conduction band is not constant, the band bottom is  $\approx 5$  meV below the Fermi energy and there are additional sub-bands (see Figure 2) at higher energies; this deviation is not significant, since the energy  $U$  is smaller and, therefore, determines the high-energy behavior of the system. The tunnel matrix-element is not constant; for a single level it is most likely higher at higher energies as indicated in Figure 37. In addition to this, an overlap factor from the many-body system may enter [83].
- **Spectrum of the isolated dot:** The spectrum of the isolated dot differs from that of the Anderson impurity model. There are more than two states of the  $N$ -electron dot as mentioned when the mapping was introduced.

## 4.10 Summary of the predictions for the Anderson impurity model

Here we want to give a short summary of the consequences that would follow from applying the Anderson impurity model to a quantum dot. This sum-

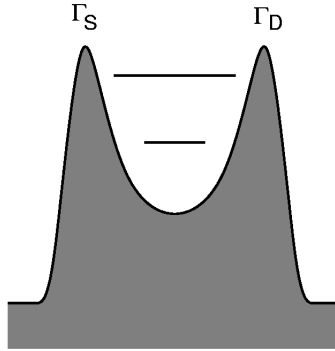


Figure 37: The barrier transparency can not be expected to be energy independent. It will be different for levels at different energies.

mary coincides nicely with some of the observations reported in Chapter 3. The quantitative comparison of our experimental data and these predictions is made in Chapter 5.

#### 4.10.1 Prediction 1: Resonance in the differential conductance at zero $V_{DS}$

The Kondo effect leads to a maximum in the differential conductance at  $V_{DS} = 0$  in the parameter range where one expects Coulomb blockade from the single-electron approximation if there is a degeneracy and the temperature is low enough.

#### 4.10.2 Prediction 2: Splitting of this resonance for finite level splitting

Resonance should appear at

$$V_{DS} = \pm \Delta \varepsilon / e \quad (33)$$

if the degeneracy is lifted by  $\Delta \varepsilon$ .

#### 4.10.3 Prediction 3: Universal temperature dependence

In the Kondo regime, the differential conductance at  $V_{DS} = 0$  is described by one universal curve if scaled with a pre-factor that is given by the asymmetry

of the tunnel-barriers and plotted as function of a reduced temperature  $T/T_K$ .

## 5 Evaluation of the Kondo resonances

In Chapter 3 the phenomenon of resonances in the Coulomb blockade region was introduced. Peaks in the differential conductance at zero drain-source voltage across a Coulomb blockade region that develop at low temperatures and split with magnetic field shall be called Kondo resonances from now on. In this chapter the temperature and magnetic field dependencies of Kondo resonances are compared with the theories for the Anderson impurity model presented in Chapter 4. This chapter is the central part of this thesis. We find that the Kondo resonances are due to a spin-degeneracy in our system. The scaling of the differential conductance at  $V_{DS} = 0$  shows a universal behavior as predicted by theory, however, the Kondo temperature observed is slightly higher than what is predicted for the Anderson impurity model.

At the end of this chapter, speculations about the other features are presented. Correlation effects will most likely also be important to explain these, but more complicated models than the Anderson impurity model might be required.

### 5.1 Magnetic field

The Anderson impurity model does not include the magnetic field directly, but the energies of the levels may have a different magnetic field dependence  $\varepsilon_{1/2}(\mathbf{B})$  and  $\varepsilon_{-1/2}(\mathbf{B})$ . A level-splitting  $\Delta\varepsilon(\mathbf{B}) = \varepsilon_{1/2}(\mathbf{B}) - \varepsilon_{-1/2}(\mathbf{B})$  leads to maxima in the differential conductance at  $V_{DS} = \pm\Delta\varepsilon/e$ . In the experiment, the Kondo resonance splits with magnetic field and the observed dependence can be well described by a Zeeman splitting  $\Delta\varepsilon = g_{\text{GaAs}}\mu_B B$  over a limited magnetic field range pointing to a spin-degeneracy. Here  $g_{\text{GaAs}} = -0.44$  is the Landé g-factor of electrons in bulk Gallium Arsenide. In the experiment, there are more than two levels and it is possible that the character of the lowest-energy level changes with the magnetic field. Therefore, it is not surprising that this result is only valid for a limited magnetic field range.

#### 5.1.1 Field in the plane of the 2DES

Figure 38 shows a series of data taken from a Coulomb blockade region with a Kondo resonance at different magnetic fields. Some of these data have already been presented in Figure 23 in a gray scale plot. The field direction is parallel to the plane of the 2DES to minimize the effect of the magnetic field on the spatial wave-functions on the dot. It can be observed

that the Kondo resonance in Figure 38(a) is split into two resonances as the field is increased from (b) to (f), the position of the split resonances is symmetric with respect to  $V_{\text{DS}} = 0$ . Each of the plots in Figure 38 contains traces for different values of  $V_{\text{G}}$  inside the Coulomb blockade region and it can be observed that the position of these split resonances is independent of the gate voltage  $V_{\text{G}}$ .

These features coincide with the prediction of the Anderson impurity model, and one can use Equation (33) to extract the splitting of the underlying level. To do this, Figure 39(a) depicts traces in the middle of the Coulomb blockade region for different magnetic fields. In Figure 39(b) the peak-to-peak distance  $\Delta V_{\text{DS}}$  over the magnetic field is shown together with a linear fit. From the slope  $0.053 \text{ mV/T} \pm 0.002 \text{ mV/T}$  of this fit one can extract the absolute value of the  $g$ -factor of the splitting for the underlying level

$$|g| = \frac{e}{\mu_{\text{B}}} \frac{1}{B} \frac{\Delta V_{\text{DS}}}{2} = 0.46 \pm 0.02$$

which coincides closely with the bulk GaAs  $g$ -factor of  $g = -0.44$ . A similar value has been reported in [48], a slightly smaller value was reported in [45].

### 5.1.2 Constant magnetic field at different angles

The lifting of a spin degeneracy should not depend on the angle between the magnetic field and the sample. This expectation can be verified by tilting the sample with respect to the magnetic field, the experimental result is shown in Figure 40. The dashed lines at  $V_{\text{DS}} = \pm 51 \mu\text{V}$  correspond to the  $V_{\text{DS}}$ -values where a spin-split Kondo resonance is expected. It has been checked that no transitions in the electron configuration take place even when the magnetic field is perpendicular to the sample in a measurement similar to the one in Figure 55.

## 5.2 Temperature dependence

In previous work [73] the temperature dependence of  $dI/dV_{\text{DS}}$  at  $V_{\text{DS}} = 0$  was fitted using three fit parameters for *each value of the level energy*  $\varepsilon$  relative to the electro-chemical potentials of the leads. Two of these parameters have a physical meaning. As the result was close to a straight line for the extracted “universal” curve found, the relevance of the result is not exceptionally high. Here, we want to extract the physical parameters ( $V_{\text{G},N}$ ,  $V_{\text{G},N+1}$ ,  $E_{\text{G}}$ ,  $\Gamma_{\text{S}}$ ,  $\Gamma_{\text{D}}$ ) from data taken at  $eV_{\text{DS}} \gg k_{\text{B}}T_{\text{K}}$ , where

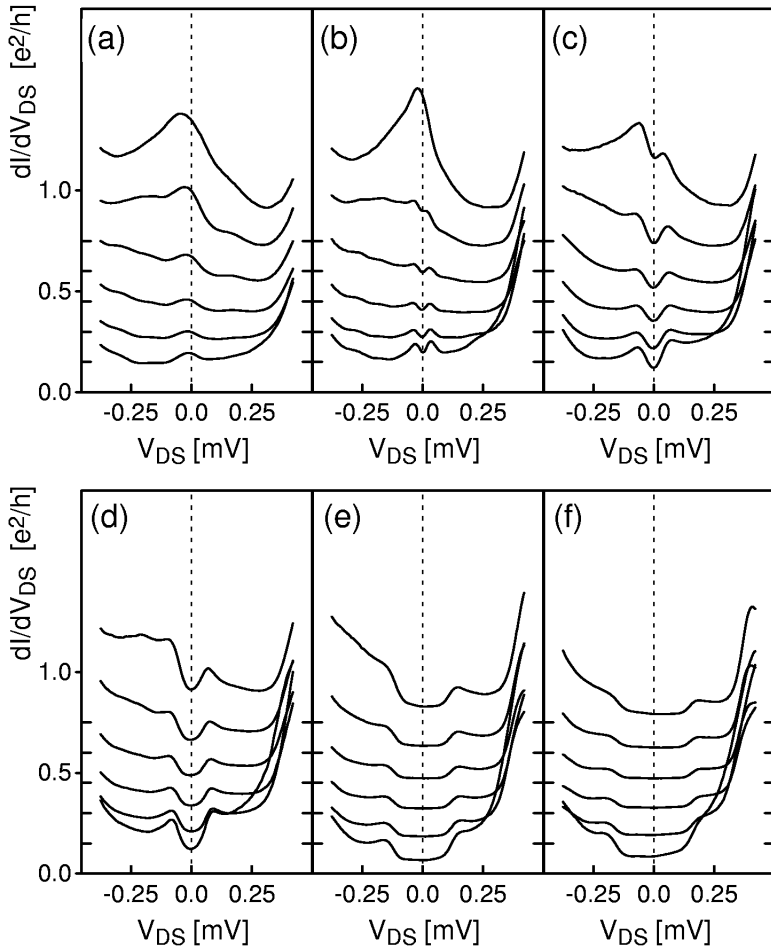


Figure 38: Differential conductance as function of the drain-source voltage  $V_{DS}$ . Each plot contains traces for different gate voltages  $V_G$  inside the CB region ((a-d)  $V_G = -0.64 \text{ V} \dots -0.63 \text{ V}$ ; (e,f)  $V_G = -0.63 \text{ V} \dots -0.62 \text{ V}$ , see also Figure 23); these curves are offset for clarity. The plots are taken for different magnetic fields: (a) 0 T (b) 1 T (c) 2 T (d) 3 T (e) 6 T (f) 8 T.

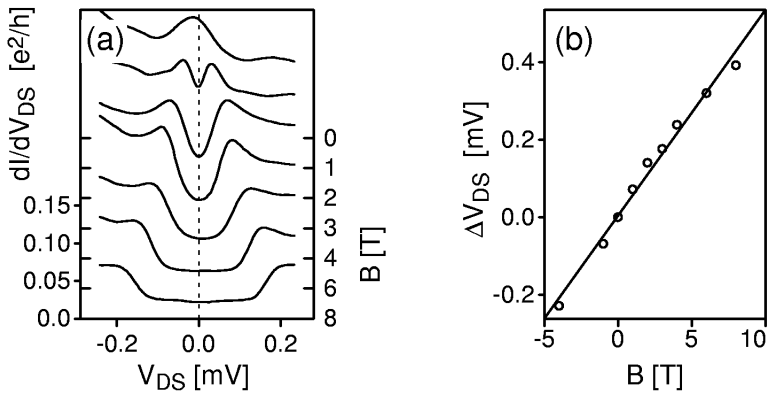


Figure 39: (a) Splitting of the Kondo resonance with magnetic field, curves are offset. (b) Peak-to-peak distance as function of the magnetic field.

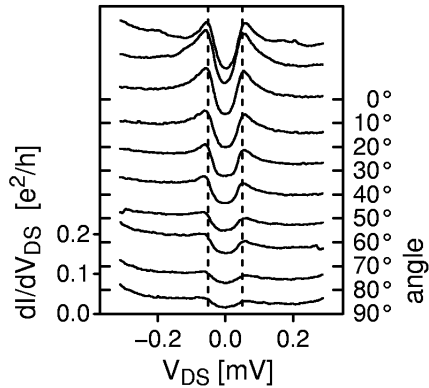


Figure 40: Differential conductance as function of  $V_{DS}$  at a constant magnetic field of 2 T. The curves for different angles are offset.

correlation effects are assumed to be less relevant and then compare to the predictions for the Anderson impurity model.

As, e. g., the Kondo temperature depends exponentially on the parameters of the system, large deviations from the predictions are expected.

### 5.3 Physical parameters and high energy behavior

To compare the experiment to the Anderson impurity model we need the physical parameters of the underlying system, which can be determined from the high energy behavior (large  $V_{\text{DS}}$  or large  $T$ ). In Figure 41(a), the differential conductance as function of the gate voltage  $V_{\text{G}}$  and the drain-source voltage  $V_{\text{DS}}$  is used to determine the energies of the dot. For the parameters  $c_{\text{D}} = 0.35$ ,  $c_{\text{G}} = 0.077$ ,  $V_{\text{G},N} = -0.5195 \text{ V}$ ,  $V_{\text{G},N+1} = -0.4995 \text{ V}$  and  $E_{\text{G}} = 1.54 \text{ meV} \pm 0.2 \text{ meV}$  the alignment of addition energies  $\mu_N = ec_{\text{G}}(V_{\text{G}0} - V_{\text{G}}) - ec_{\text{D}}V_{\text{DS}}$  and  $\mu_{N+1} = E_{\text{G}} + \mu_N$  with the source and drain electro-chemical potentials is indicated by dashed lines in Figure 41(a), in good agreement with the observed single-electron transitions. In the data in Figure 41(b) a saturation of the current for positive and negative  $V_{\text{DS}}$  with very similar values  $I_+ = 21 \text{ nA} \pm 2 \text{ nA}$  and  $I_- = 19 \text{ nA} \pm 2 \text{ nA}$  is observed, however, the data do not show a nice plateau, as in Figure 16. This symmetry means, that the barriers have approximately the same height and one can extract the barrier transparencies from Equations (26) and (27)  $\Gamma_{\text{D}} = 162 \text{ GHz} = 0.11 \text{ meV}/\hbar$  and  $\Gamma_{\text{S}} = 220 \text{ GHz} = 0.14 \text{ meV}/\hbar$ . The reasonable errors in the saturation currents translates into large errors for the barrier transparencies such that values as different as  $112 \text{ GHz} < \Gamma_{\text{D}} < 266 \text{ GHz}$  and  $144 \text{ GHz} < \Gamma_{\text{S}} < 411 \text{ GHz}$  are compatible with our measured saturation currents.

This information determines all model parameters and it is principally not necessary to use the linewidth of the single-particle resonances to determine  $\Gamma$  as in the case of a non-degenerate level. Rather one can use the comparison with the line-shapes to see if these parameters are consistent with the high energy behavior of the system. However, the line-shapes are intrinsically a higher order effect and we do not know for sure how and whether the degeneracy enters into the linewidth. We assume that at a “high” voltage  $|V_{\text{DS}}| = 0.6 \text{ mV}$  correlation effects between spin up and down can be neglected and assume that  $\Gamma$ , the sum of the transparencies of the source and drain barriers determines the width of the Lorentzians in Figure 42 (we want to explicitly warn the reader that this assumption may be wrong and that  $\Gamma$  may be smaller by a factor of two than what we use in the following!).

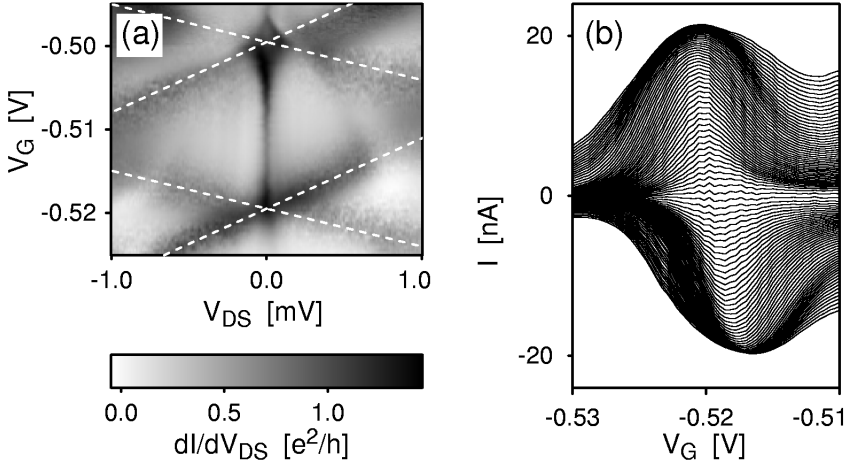


Figure 41: (a) Experimental data and the position of the single-particle resonances. (b) Current traces for different values of  $V_{DS}$  between  $-1$  mV and  $1$  mV.

With this assumption, the data in Figure 42 are compared to Equation (18) with a Lorentzian line-shape as given in Equation (28). Even though this comparison has no free parameters, Equation (28) has unphysical discontinuities when one crosses the single-particle resonances and for a better comparison a more detailed theory would be necessary. The agreement for  $\Gamma = 460$  GHz  $\equiv 0.32$  meV/ $\hbar$  shown in Figure 42(c,d) does not agree perfectly with the data. The results for smaller tunnel-coupling are depicted in Figure 42(a,b) and for stronger tunnel-coupling in Figure 42(e,f) to give an idea of the quality of the fit. The deviation may in part be due to neighboring resonances and in part to a dependence of the model parameters on the applied voltages.  $\Gamma = 0.32$  meV is used in the following evaluation.

### 5.3.1 Temperature dependence of the differential conductance at $V_{DS} = 0$

In Figure 43, the temperature dependence of the differential conductance at  $V_{DS} = 0$  is shown for two adjacent Kondo valleys. The left valley in Figure 43 corresponds to the valley for which the parameters were extracted in the previous section. It is clearly visible that the valley conductance decreases with increasing temperature.

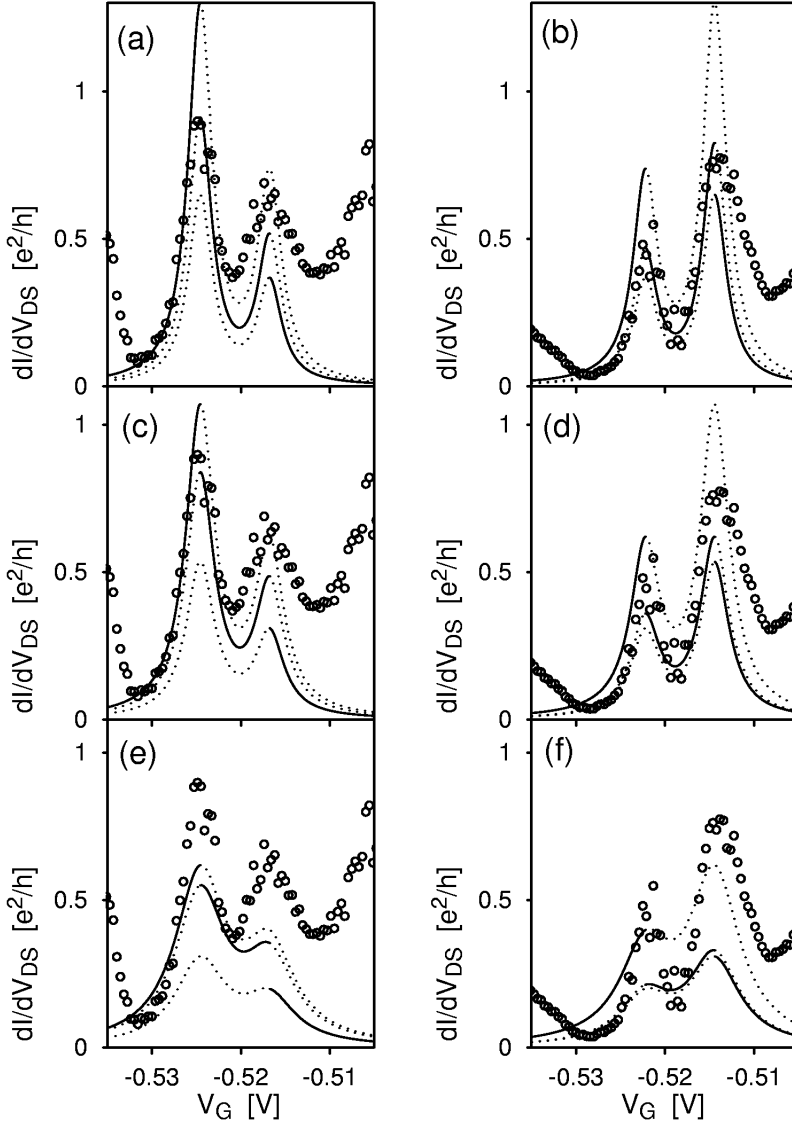


Figure 42: Differential conductance at  $V_{DS} = 0.6 \text{ mV}$  (a, c, e) and  $V_{DS} = -0.6 \text{ mV}$  (b, d, f). The rings are experimental data, the solid line is the approximation as described in the text. (a, b) are calculated for  $I_{\pm} = \{21 \text{ nA}, 19 \text{ nA}\} \Leftrightarrow \Gamma = 380 \text{ GHz}$ , (c, d) for  $I_{\pm} = \{23 \text{ nA}, 17 \text{ nA}\} \Leftrightarrow \Gamma = 460 \text{ GHz}$ , (e, f) for  $I_{\pm} = \{25 \text{ nA}, 15 \text{ nA}\} \Leftrightarrow \Gamma = 800 \text{ GHz}$ .

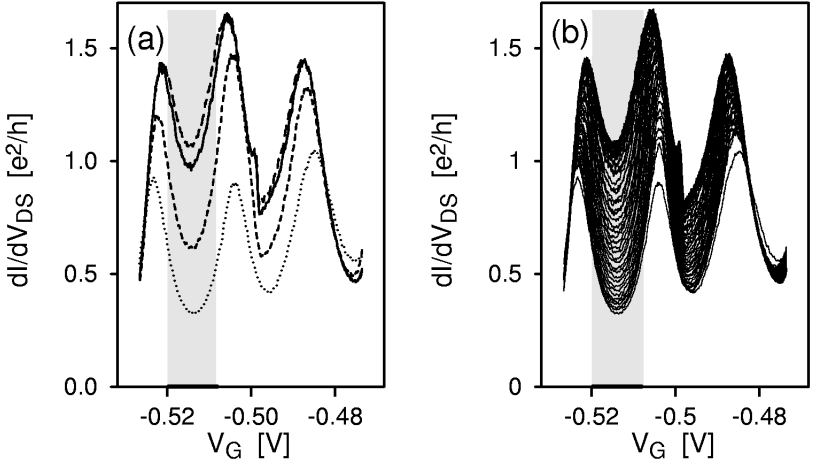


Figure 43: (a) Differential conductance at  $V_{DS} = 0$  for base temperature (long dashed), 49 mK (solid), 190 mK (short dashed) and 800 mK (dotted). (b) The same data for more temperatures. The curves are not offset.

At temperatures between 50 mK and base temperature this behavior saturates which we do not attribute to a physical effect but to a difference between sample and bath temperatures. Therefore, we exclude data below 50 mK from the following evaluation. The predicted universal behavior for the differential conductance at  $V_{DS} = 0$  as a function of a reduced temperature  $T/T_K$  only applies to the gate-voltage range, where there is one electron on the degenerate level; we, therefore, restrict the analysis to gate-voltages that are away from the single-particle resonances by one linewidth  $\Gamma$ .

With the parameters determined in the previous section one can calculate the predicted universal behavior for the data selected according to the above criteria. For this we introduce the scaled differential conductance

$$dI/dV_{\text{scaled}}(T/T_K(V_G)) = dI/dV_{DS}(T, V_G) / \gamma.$$

The pre-factor  $\gamma = (\Gamma_S + \Gamma_D)^2 / 4\Gamma_S\Gamma_D$  takes care of the asymmetry in the barriers. The dependence of the Kondo temperature  $T_K$  on the gate voltage  $V_G$  is given by the combination of Equation (29) and a linear dependence of the level energy — which is identified with the addition energy  $\mu_N$  — on the gate voltage:  $\varepsilon(V_G) \equiv \mu_N(V_G) = -U(V_{GN} - V_G) / (V_{GN+1} - V_{GN})$ . The Kondo temperature thus obtained is plotted in Figure 44 as a function

of the gate voltage  $V_G$  and used for the scaling in the following paragraph.

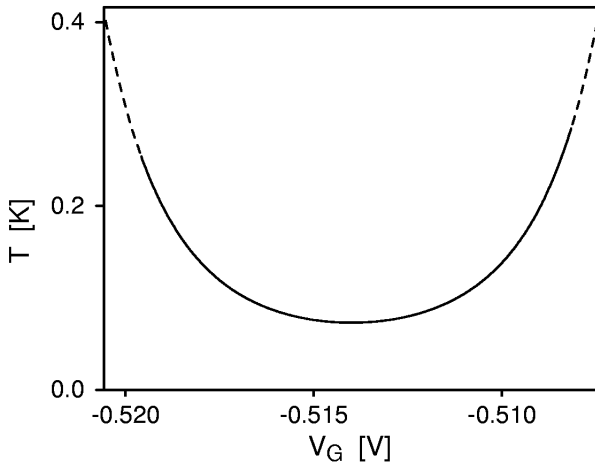


Figure 44: Calculated Kondo temperature as a function of the gate voltage. The solid line corresponds to the gate voltage range used in the scaling, here the calculated Kondo temperature lies between 0.073 K and 0.28 K. As one gets closer to the single-particle resonances, the concept of a Kondo temperature is no longer valid, Equation 29 grows exponentially as indicated by the dashed curve.

The result for the scaled differential conductance is shown in Figure 45. This result depends on  $U \equiv E_G = 1.54$  meV and  $\Gamma = 460$  GHz, which are of physical interest as well as the parameters necessary for the comparison to the experiment, i. e.  $\gamma = 1.25$  and  $V_{G,N} = -0.524$  mV,  $V_{G,N+1} = -0.504$  mV. It is immediately evident that the 12059 data points taken at 31 different temperatures and 389 different values of  $V_G$  from the gate voltage range marked by a grey background in Figure 43 are scaled to a narrow region. This region splits into two branches at low reduced temperatures, which correspond to data points taken close to the left and middle peak in Figure 43. These have different heights indicating that the system deviates from the Anderson impurity model. Since the parameters  $\gamma$  and  $\Gamma$  were determined at the position of the left resonance, the lower branch should be considered more accurate. Nevertheless, the form of the curve and the prediction by Hamann [74] (Equation (30)) are similar.

In Figure 46 we depict our data together with modifications of the Hamann curve for which there is no theoretical or experimental justifica-

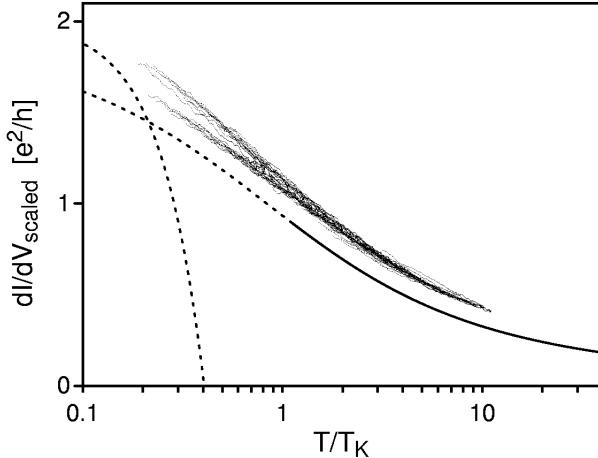


Figure 45: Comparison of the scaled data with theory as described in the text.

tion. In Figure 46(a), an offset of  $0.17 e^2/h$  is added to the Hamann curve to simulate some sort of “parallel channel” in the experiment, the agreement at higher temperatures is not convincing. In Figure 46(b), the Hamann result is multiplied by 1.21 to simulate an error in the pre-factor  $\gamma$ . In Figure 46(c), the Kondo temperature used for the Hamann curve is multiplied by a factor of 1.66. This change in the theory gives the nicest agreement and seems to indicate that the Kondo temperature in the experiment is higher than what we expect from theory.

### 5.3.2 Relevance

In the previous section we have found the expected scaling behavior, but there are quantitative differences between our experimental data and theory. At the same time, some of the five parameters, especially  $\Gamma$ , used for the scaling bear a large uncertainty and it requires further discussion as to whether this deviation is significant. In particular, the questions that have to be addressed are: Is the scaling unique or are there other parameter sets which scale the  $V_{DS} = 0$  data to a single curve? If so, are these parameter sets compatible with our other measured data?

To answer these questions we show the data scaled for different param-

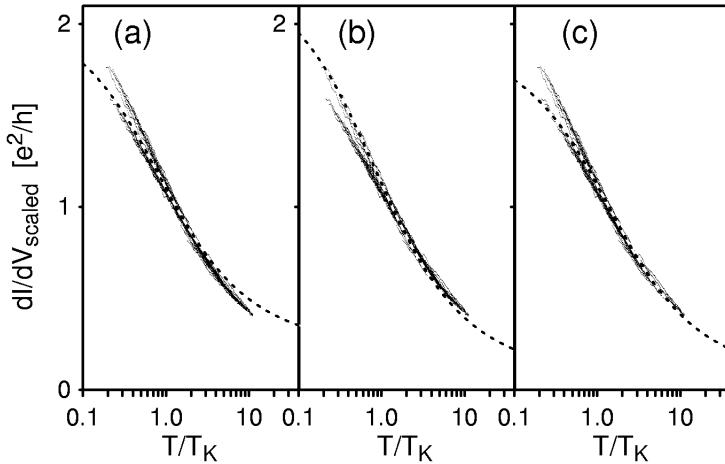


Figure 46: Data scaled as in Figure 41, but the Hamann curve is offset in (a), scaled vertically in (b) and offset horizontally in (c).

eter sets. In the following figures, the Figure 45 is added as plot (b) for comparison.

### Shifting the valley:

In Figure 47, the gate voltages  $V_G$  at which the “first” and the “second” electron are added are shifted by 10% of the valley width  $V_{G,N+1} - V_{G,N}$  simultaneously. This error destroys scaling.

### Changing the width of the valley:

In Figure 48, the above used addition voltages  $V_G$  are used in a different combination corresponding to a narrower valley in (a) and a wider valley in (c). In both cases scaling is destroyed.

Now we want to illustrate the effect of changes to the important model parameters  $\Gamma$  and  $U$  on the scaling behavior to give a feeling for the relevance of the observed scaling. Since  $\Gamma$  has the largest uncertainty we start out by using the  $\Gamma$  values from Figure 42 that bracket the correct value and leave all other parameters the same as in Figure 41.

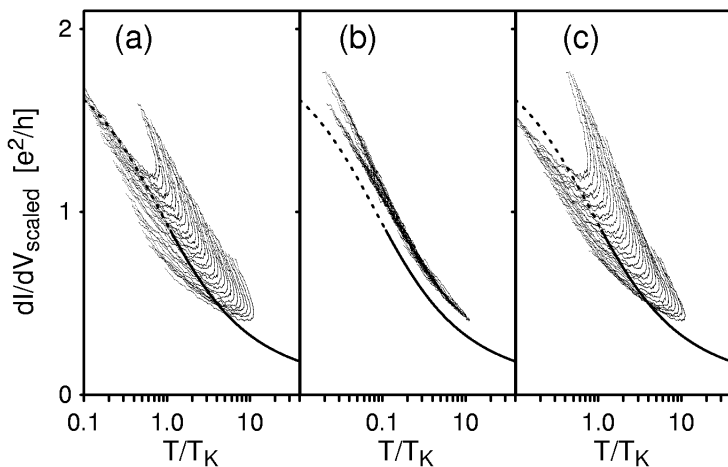


Figure 47: Shifting the valley: (a)  $V_{G,N} = -0.526$  V,  $V_{G,N+1} = -0.506$  V; (b)  $V_{G,N} = -0.524$  V,  $V_{G,N+1} = -0.504$  V; (c)  $V_{G,N} = -0.522$  V,  $V_{G,N+1} = -0.502$  V.

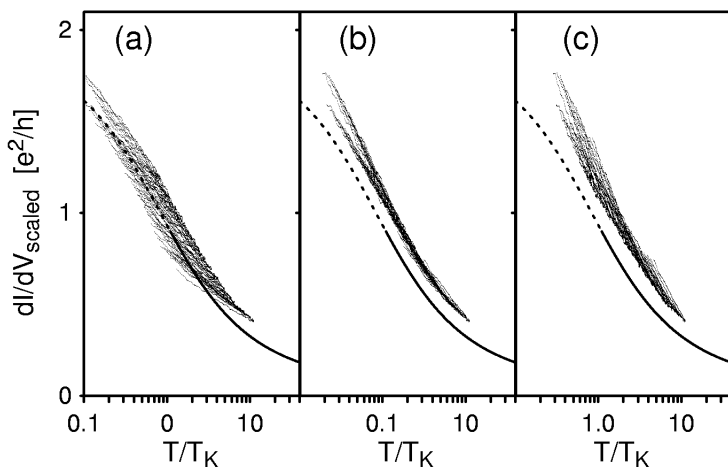


Figure 48: Changing the width of the valley: (a)  $V_{G,N} = -0.522$  V,  $V_{G,N+1} = -0.506$  V; (b)  $V_{G,N} = -0.524$  V,  $V_{G,N+1} = -0.504$  V; (c)  $V_{G,N} = -0.526$  V,  $V_{G,N+1} = -0.502$  V.

### Changing $\Gamma$ and $\gamma$ :

In Figure 49, both the linewidth  $\Gamma$  and the pre-factor  $\gamma$  are varied. The case (a) corresponds to the value extracted from the saturation currents  $I_{\pm}$ . Case (b) is still compatible with  $I_{\pm}$  within the estimated error and was determined as the best value by comparison with the line-shapes. Case (c) corresponds to twice the estimated error in  $I_{\pm}$ . While the small difference in the saturation currents leads to a large uncertainty in  $\Gamma$ , the value of  $|I_+| + |I_-|$  is kept constant by changing  $\gamma$  to stay compatible with the saturation values of the current. The dependence on  $\gamma$  only scales the differential conductance axis, and the apparent better agreement in (a) is due to the value of  $\gamma$  close to 1 (similar to just rescaling the differential conductance axis).

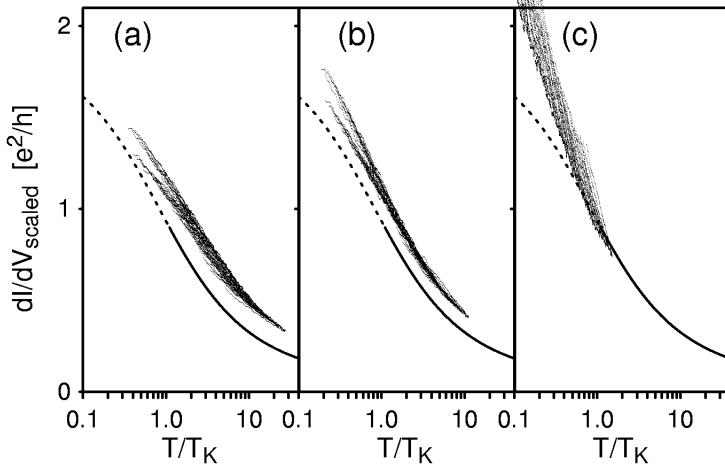


Figure 49: Changing the barrier transparencies: (a)  $\Gamma = 380$  GHz,  $\gamma = 1.02$ ; (b)  $\Gamma = 460$  GHz,  $\gamma = 1.25$ ; (c)  $\Gamma = 800$  GHz,  $\gamma = 2.3$ .

### Changing the Coulomb interaction $U$ :

In Figure 50 on the facing page, the Coulomb energy is varied. It is immediately noticeable that the Kondo temperature goes down for the low value of  $U$  in (a) the scaling, though, gets

slightly worse. The values of  $U$  used are already outside the estimated error for  $U$ .

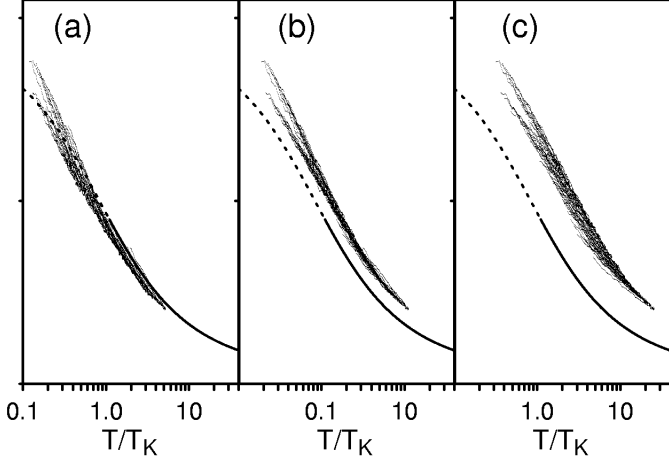


Figure 50: Changing the Coulomb interaction: (a)  $U = 1.2$  meV, (b)  $U = 1.54$  meV, (c)  $U = 1.9$  meV.

We have seen that a smaller value of  $U$ ,  $\Gamma$  and  $\gamma$  might lead to better agreement with the predictions by Hamann. We, therefore, have varied all of these parameters to get a good scaling for a different parameter set. The result in Figure 51 does show a nice scaling, but we can exclude that the parameter set used is correct: The value of  $U$  is too small in comparison to the pattern of single-particle resonances observed. In addition to this, the small value of  $\gamma = 1.02$  is not compatible with the expected saturation of the scaled differential conductance close to the single-particle resonances at  $V_{\text{DS}} = 0$  towards  $2e^2/h$ . The value of  $\gamma = 1.25$  taken for the best fit is much better in this respect, nevertheless, this argument breaks the logic of not using the  $V_{\text{DS}} = 0$  results to determine the model parameters.

### 5.3.3 Conclusions on the scaling

In the previous section, we have seen that the universal scaling of the differential conductance in the Kondo regime seems to hold. As it was possible to scale the data to a curve for different parameter sets, it is not possible to determine the system parameters from the scaling behavior alone and to verify

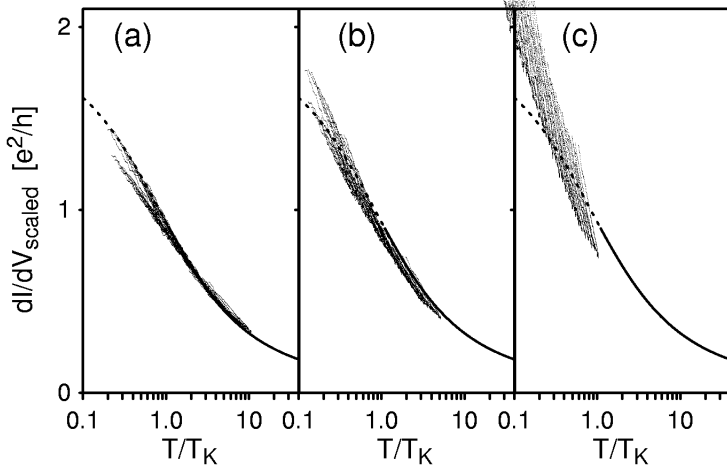


Figure 51: Changing Coulomb interaction and barrier transparencies: (a)  $U = 1.2$  meV,  $\Gamma = 380$  GHz,  $\gamma = 1.02$ ; (b)  $U = 1.54$  meV,  $\Gamma = 480$  GHz,  $\gamma = 1.25$ ; (c)  $U = 1.9$  meV,  $\Gamma = 800$  GHz,  $\gamma = 2.3$ .

or disprove the theory. However, when using the parameters extracted from the high energy behavior of the system, there are quantitative deviations from the predicted scaling that are significant. These can be best modeled by assuming that the Kondo temperature obtained from Equation (29) is too low by a factor of 1.66. This deviation could be attributed to two different origins: There is no fully accurate theory and the Kondo temperature is related to a smooth transition. The temperature in the Hamann curve used in our comparison contains a factor of 1.2 introduced by Costi based on a comparison with his numeric calculations.

Another possible origin could be the deviation of the quantum dot from the Anderson model. There are calculations that additional levels can lead to higher Kondo temperatures [80]. The difference from the Anderson model can possibly be absorbed into a different Kondo temperature and this may be the case here. Further theoretical studies are needed if one wants to describe these effects, the next level seems to be located at  $\Delta\mu \approx 650 \mu\text{eV}$ .

Additional experimental data would also be very useful in determining whether this deviation is an effect different for every dot and electron number, or whether it is a general effect. Even though I have data for several Kondo resonances, the one studied here was the only one that had a well

enough developed Coulomb blockade region to make a quantitative comparison.

## 5.4 Speculations on the other features

One feature observed in two samples was a resonance in the Coulomb blockade region deviating from  $V_{\text{DS}} = 0$  with  $V_{\text{G}}$  (see Figure 25). At this point, we can only speculate about its origin, but one possible explanation is the following:

The Kondo resonances at  $V_{\text{DS}} = 0$  can be attributed to a single spin-degenerate electronic level. If, by chance, two different levels become (nearly) degenerate for different spin, the predictions of the Anderson impurity model still hold, but the dependence of the model parameters on the applied voltages may be different: In the case of a single level, all coefficients  $c_i$  are the same for spin up and spin down and the degeneracy is independent of the gate voltages as long as the electron number does not change. These coefficients can be different for different levels as suggested by the evaluation in section 2.4.3. Then there will be an energy splitting that depends on the gate voltages similar to the splitting of a spin degenerate level with magnetic field.

## 6 Kondo resonances and electron configuration

In the previous chapters, Kondo resonances associated with one Coulomb blockade region were attributed to a spin degeneracy of the electrons on the dot. However, for each quantum dot several Coulomb blockade regions associated with different electron numbers can be observed. Here we want to study the question, for which electron numbers Kondo resonances occur. For this a detailed study of the dot spectrum is necessary; the transitions observed in magnetic fields provide information about this spectrum. A regular pattern in the occurrence of Kondo resonances is found, these resonances are split at finite magnetic fields.

### 6.1 Previous work

In 1928 Fock [84] and in 1930 Darwin [85] calculated the spectrum of non-interacting electrons in two dimensions confined in a parabolic potential in the presence of a magnetic field. This simple system can be solved analytically and one obtains an energy spectrum, as well as different sets of quantum numbers. Even though this model can only be a crude approximation for our quantum dots as the potential is not harmonic and the electrons interact, the quantum numbers obtained from these calculations are useful to label the levels on the dot.

In experiments on split-gate quantum dots [86], Mc Euen et al. observed transitions in the electronic states. These were explained in terms of a self-consistent Thomas-Fermi approximation. One interesting point to note is that the Landau index was used as a quantum number in much the same way as in the exact solution for a parabolic confinement potential.

In a different system, namely vertical quantum dots, transport experiments [11, 12, 13] have lead to beautiful data that could be interpreted well in terms of single-particle spectra slightly modified by Coulomb interaction. Capacitive measurements by Ashoori et al. [87] show similar behavior. The interpretation introduced by these previous experiments is used here to determine the electron number and electron configuration.

In the context of Kondo resonances, this knowledge has been ignored and an odd-even effect for the occurrence of Kondo resonances was expected [64] from the very simple picture of filling single-particle levels consecutively with one and two electrons as depicted in Figure 53(a) and expected from the constant interaction model presented in Chapter 2. Of course, levels are not filled consecutively in the presence of an orbital degeneracy, Coulomb inter-

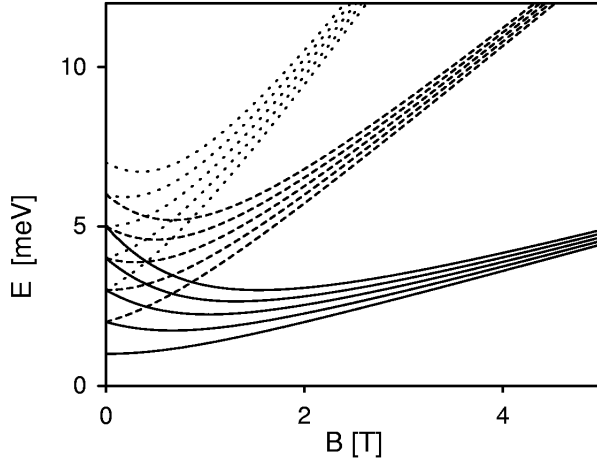


Figure 52: Fock Darwin energy-spectrum as calculated from Equation (34) in Appendix B. The confinement potential is taken as  $\hbar\omega_0 = 1$  meV. Solid lines: states with Landau index  $N_+ = 0$ , dashed and dotted lines states with Landau index  $N_+ = 1$  and  $N_+ = 2$  respectively.

action between the electrons leads to Hund's rules for the filling. Assuming there are three nearly degenerate levels on the dot, a sequence of adding electrons as indicated in Figure 53(b) is more realistic. Goldhaber-Gordon et al. claim to see an odd-even behavior based on experiments where two Kondo valleys are observed [45]. In the interpretation of their experiments Cronenwett et al. [48] claim to have found the Kondo effect for odd electron numbers based on seven Coulomb blockade valleys, but the temperature dependence they used as the criterion is inconsistent across their data. The valley labeled with "2" (corresponding to  $N + 2$  electrons on the dot where  $N$  is unknown in this experiment) shows a zero bias resonance, whereas 2 is not commonly considered to be an odd number. In addition to this, no connection is made with the electron numbers and the statement could, at most, be that of an alternation in the occurrence of Kondo resonances.

## 6.2 Kondo resonances and electron configuration

To understand how the filling of levels is related to the occurrence of Kondo resonances, it is instructive to mention the assumptions underlying the odd-even expectation [64, 45, 48]:

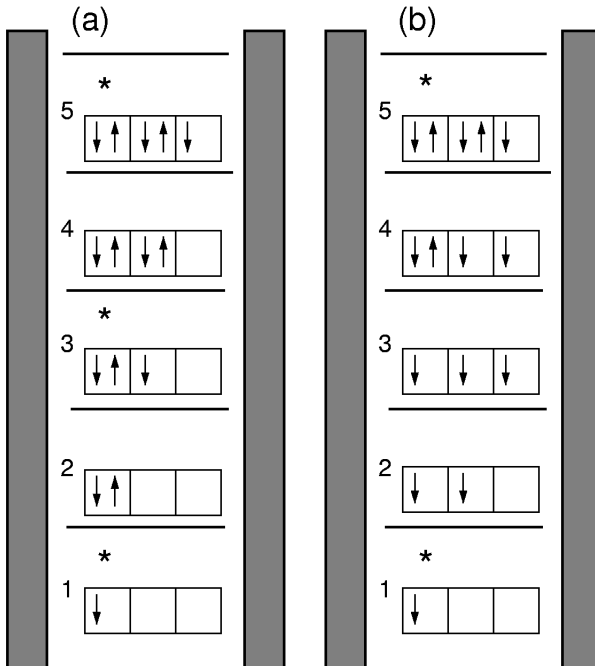


Figure 53: Putting electrons into single-particle levels on the quantum dot. Each box represents a level that can be filled with a spin-up and a spin-down electron symbolized by arrows. (a) For non-degenerate levels and non-interacting electrons. (b) Hund's rule will favor spin parallel occupation for (nearly) degenerate levels.

- A spin degeneracy leads to a Kondo resonance.
- For odd electron numbers there is an unpaired spin on the dot and thus a degeneracy.

The first assumption is incomplete in that it neglects the importance of tunnel-coupling: Even in the presence of a degeneracy the observability of a Kondo resonance depends exponentially on the tunnel-coupling and there is not necessarily a one to one correspondence between degeneracy and the observation of a Kondo resonance in the experiment.

The second assumption is wrong for quantum dots as shown by a large number of experiments, e. g. [11, 88, 13]. Our experimental observation (Figure 54) of Kondo resonances in two adjacent CB valleys immediately disproves this expectation. However, in the presence of an orbital degeneracy, it may be necessary to study extensions to the Anderson impurity model like the Coqblin-Schrieffer model [89] to get an accurate description of the quantum dot.

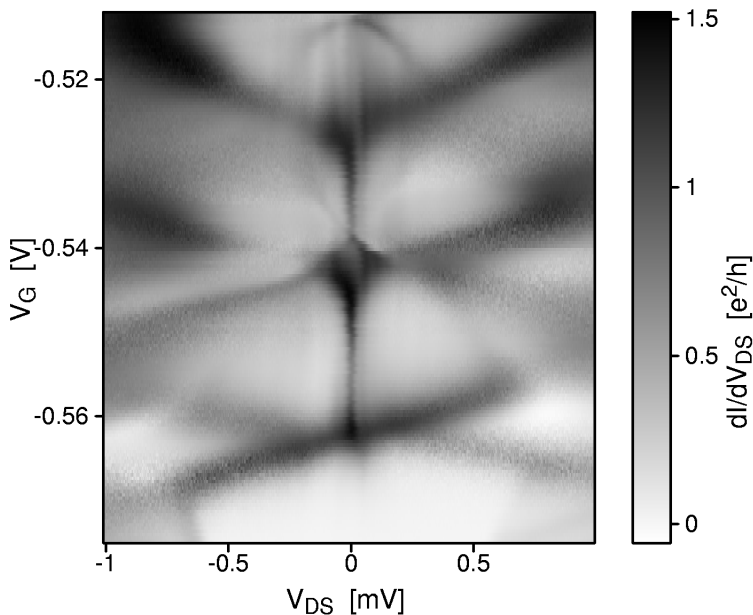


Figure 54: Kondo resonances in two adjacent Coulomb blockade valleys.

In our experiments it turns out that a simple picture of Kondo resonances being due to a strongly tunnel-coupled singly-occupied level is sufficient to qualitatively describe the observations. The question raised, namely how the levels on the dot are filled with electrons, does not have to rely on assumptions, but is directly accessible to experiment as shown in the next subsection.

### 6.3 Interpretation of the transitions observed in a magnetic field

In Figure 55(a), a measurement of the differential conductance through the quantum dot at  $V_D \approx 0$  is presented as a function of the magnetic field  $B$  and the gate voltage  $V_G \equiv V_M$  applied to the middle gate fingers. The magnetic field is applied perpendicular to the plane of the 2DES. In these data, the Coulomb blockade peaks correspond to maxima that can be traced horizontally. These transitions have kinks that have to be related to transitions of the electronic states on the dot. In our data these transitions can be grouped into a series of transitions observed at higher fields (group I, connected by dotted lines in Figure 56) and a series observed at lower fields (group II, dashed lines in Figure 56).<sup>2</sup>

For sufficiently high magnetic fields, the electrons on the dot will be spin-polarized in electronic states which converge towards the lowest Landau level at high magnetic fields as seen in Figure 52. These states, therefore, carry a Landau index of 0. When lowering the magnetic field, the spin polarization decreases leading to a series of kinks in the position of the single-electron tunneling peak [86]. Counting these kinks gives direct access to the electron number on the dot as indicated in Figure 56. The two adjacent Coulomb blockade valleys for which Kondo resonances appear are marked by arrows in Figure 55 and correspond to the electron numbers 7 and 8.

This type of counting relies on the correct identification of where the quantum dot is fully spin-polarized, where the quantum dot is fully spin-unpolarized, and the identification of all intermediate spin flips. One possible source of error is the occurrence of spin flips at higher fields. It can be ruled out from well-resolved data not shown here that the regular pattern of spin flips continues to higher fields. Another source of error could be that the electrons are not fully depolarized at the point where the transition of

---

<sup>2</sup>Additional structure in the Coulomb blockade peaks that is especially visible at  $B \approx 3$  T can be attributed to the 2DES areas in the source and drain leads. See also appendix C.

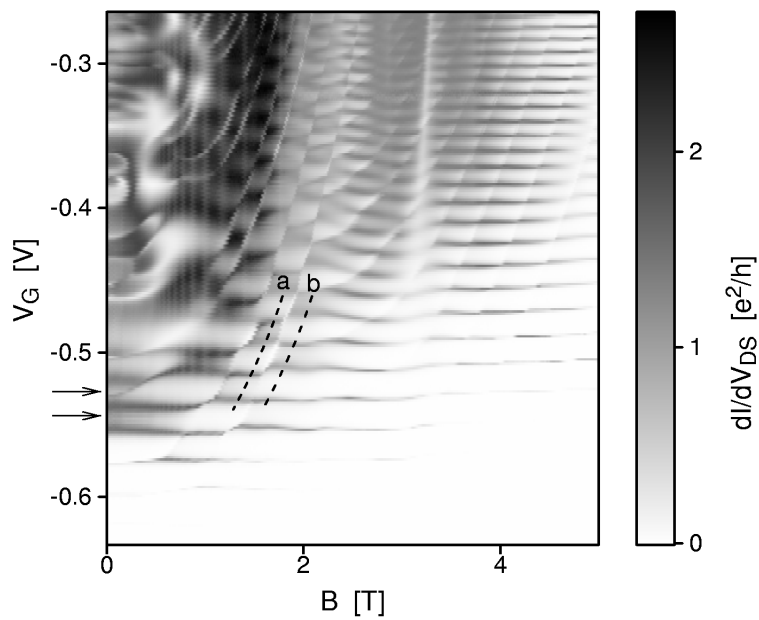


Figure 55: Differential conductance at  $V_{DS} \approx 0$  in a perpendicular magnetic field  $B$ .

group II starts. Measurements on our quantum dot in tilted magnetic fields have shown that this can indeed happen: It can be identified by lines of group I intersecting those of group II. This is not observed in Figure 55 and, therefore, this source of error can be excluded for the interpretation.

The interpretation that spin flips are responsible for the transitions of group I is supported by the fact that the lines of group I end on the outermost line of group II at each second single-electron tunneling peak: the number of electrons has to be increased by two electrons to see an additional spin flip.

One likely interpretation of the transitions of group II is that the electrons are transferred to levels with a higher Landau index. For the most negative gate voltage region of Figure 55, the electron configuration is depicted in Figure 56, in accordance with the picture described above: Between dotted or dashed lines connecting transitions of group I and group II, respectively, the electrons are added in a spin-up/spin-down fashion with increasing gate voltage. Following one Coulomb blockade region of fixed electron number, the electrons are fully spin-polarized at sufficiently high fields and are depolarized one by one with decreasing magnetic field. At even lower fields, the electrons are transferred from levels with Landau index 0 to levels with higher Landau index.

## 6.4 Kondo effect in different Coulomb blockade regions

The Kondo effect observed in quantum dots leads to an increased conductance in the Coulomb blockade valleys for small drain-source voltages  $V_{DS} \approx 0$ . In Figure 55 an alternation in the valley conductances at low fields can be observed as one crosses either a transition belonging to group II (dashed line in Figure 56) or a single-electron tunneling peak, leading to a checkerboard pattern between the group II transitions. By comparing with the electron configuration derived before and depicted in Figure 56, the high conductance valleys correspond to electron configurations where the highest level with Landau index 0 of the quantum dot is occupied by a single electron.

To study this further we have measured the differential conductance as a function of the source-drain voltage and the gate voltage, adjusting the magnetic field at the same time to follow one of the two lines depicted in Figure 55. Along these lines we expect electrons to be added to the dot in a spin-up/spin-down fashion to levels with Landau index 0. The difference between line (a) and line (b) is that there is an additional electron in a

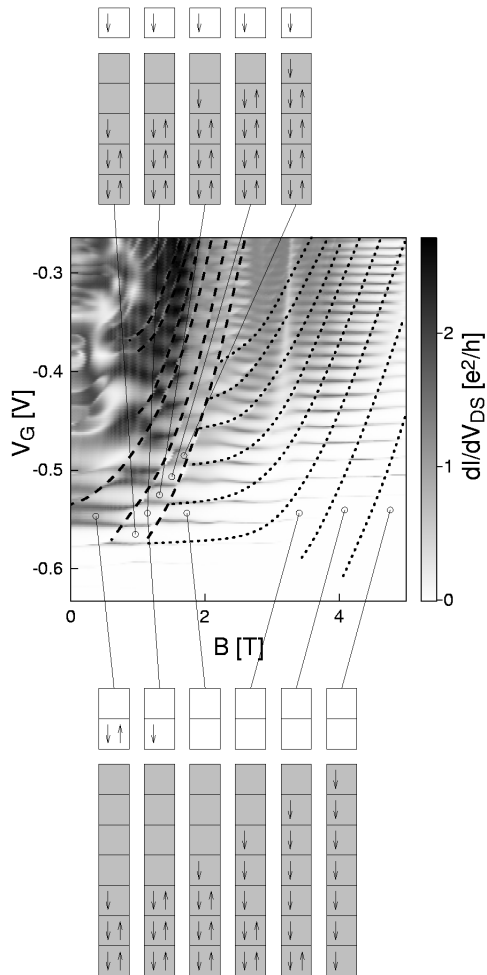


Figure 56: Identification of the states on the dot. Each box corresponds to one level, the boxes with grey background stand for levels with Landau index 0. Top: Within a regular region the electrons are added spin down - spin up to levels with Landau index 0. Bottom: The arrangement of seven electrons on the dot changes with magnetic field.

level with higher Landau index along line (a). In both cases, there is one unpaired spin on the dot for an odd *total* number of electrons and the system can be directly mapped to the Anderson impurity model. Along line (a) the situation is more complicated for even numbers of electrons with two unpaired spins on the dot.

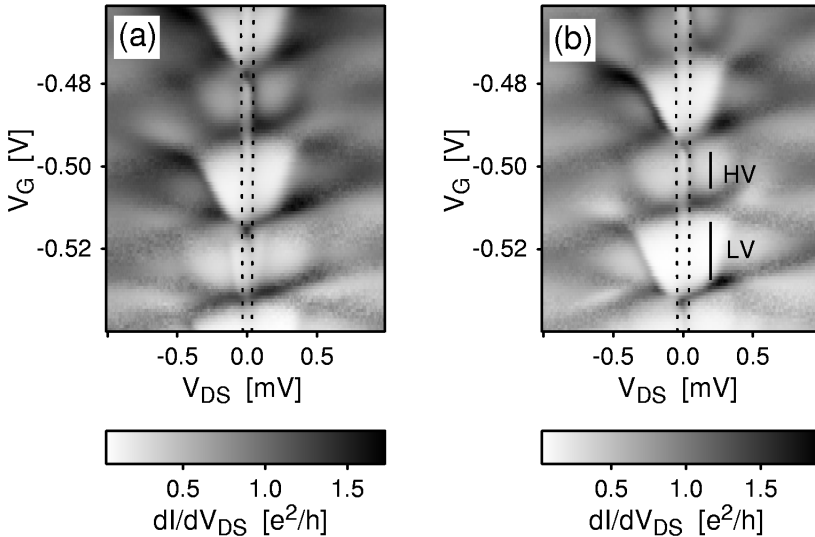


Figure 57: (a) Differential conductance in gray-scale as a function of  $V_{DS}$  and  $V_G(B)$ . The magnetic field is adjusted to follow the dashed lines in Figure 55. Maxima in the high conductance valleys at the position of the spin splitting (dashed lines) are visible.

The experimental results are shown in Figure 57. In both cases, resonances are visible at  $V_{DS} = \pm g_{\text{GaAs}} \mu_B B / e$  in the high conductance valleys as expected for Kondo resonances due to a level spin-split by the Zeeman energy (better visible in the details in Figure 58). For the low conductance valleys, a split Kondo resonance is seen in the case (a) — where it could be attributed to the singly occupied level with higher Landau index — but also in the case (b). To explain this observation, one has to observe that the data in Figure 57(a) look very similar to those in Figure 57(b), but are shifted by one Coulomb blockade region along the gate voltage axis. This similarity can be easily explained if the tunnel-coupling for exchanging the electron on the level with higher Landau index is small: In such a case, correlation

effects involving the electron on this level can be neglected and it causes only a shift in the gate voltage. It is, therefore, reasonable to interpret both sets of data in Figure 57 in terms of the electrons with Landau index 0 and the coincidence of a high conductance valley with an odd number of electrons with Landau index 0 is understood. However, the occurrence of split resonances in the low conductance valleys visible in Figure 6(b) remains to be explained.

Analyzing the data in Figure 57 (and also in Figure 60(a)) more carefully by looking at the line-plots in Figure 58, the following details become evident: The height of the split resonances is approximately constant in the high conductance valleys. The height of the split resonances decays towards more negative gate voltages in the low conductance valleys. In one high conductance valley additional structure is clearly visible at low  $V_{DS}$  (Figure 59) and the split Kondo resonance is not well developed. This is similar to the observation presented in Figure 24 and is most likely due to an excited state at low energies.

An additional observation in Figure 57 can be made: At the gate voltages where the single-particle resonances for adding an even electron cross the  $V_G$ -axis one sharp peak is observed that looks remarkably like the Kondo resonances observed in the absence of magnetic fields within a Coulomb blockade region. At the gate voltages where the single-particle resonances for adding an odd electron cross the  $V_G$ -axis a dip is observed with a width corresponding to the spin-splitting. The temperature dependence of these features is studied in the next section.

## 6.5 Temperature dependence of the split Kondo resonances

The overall temperature dependence of these effects is given in Figure 60 and temperature dependencies for the details just described in Figures 61 and 62. In Figure 60 we present data comparable to Figure 57(b) at a temperature of  $T = 25$  mK (Figure 60(a)) and at  $T = 400$  mK (Figure 60(b)). The overall structure of Coulomb blockade is preserved in this temperature range including the high and low valley conductances. However, the split resonances attributed to the Kondo effect has disappeared at 400 mK. This is shown in more detail in Figure 61. The split resonance for the high conductance valley in (a) have disappeared at 200 mK, the split resonances in the low conductance valleys in (b) already disappear at 100 mK leaving a slightly enhanced conductance at  $V_{DS} = 0$  behind. The structures close

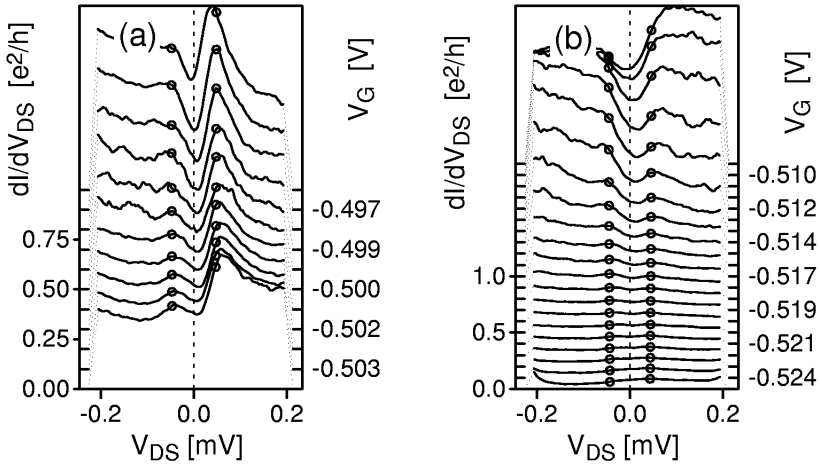


Figure 58: Details of the data in Figure 57(b), the curves are offset for clarity. The curves in (a) correspond to the gate voltage range marked “HV” in Figure 57, in (b) they correspond to the gate voltage range marked “LV” in Figure 57. The circles mark the position at which a spin-split Kondo resonance would be expected.

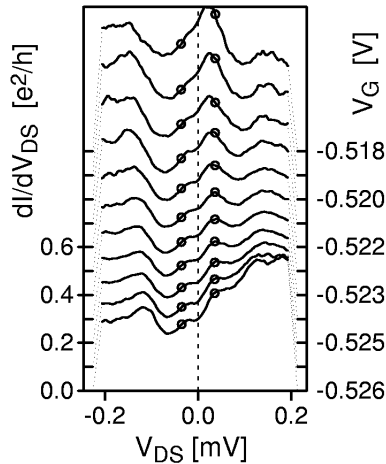


Figure 59: Details of the data in Figure 57(a). For this high conductance valley, a resonance at the value of the spin splitting is only weakly developed and there is a further feature at  $\approx 150 \mu\text{eV}$ .

to the single-electron resonances in Figure 62 display a similarly strong temperature dependence and probably also require correlation effects as an explanation. The minimum in the differential conductance at  $V_{DS} = 0$  for adding an odd electron in Figure 62(a) is no longer present at  $T = 200$  mK and the maximum in Figure 62(b) is strongly reduced.

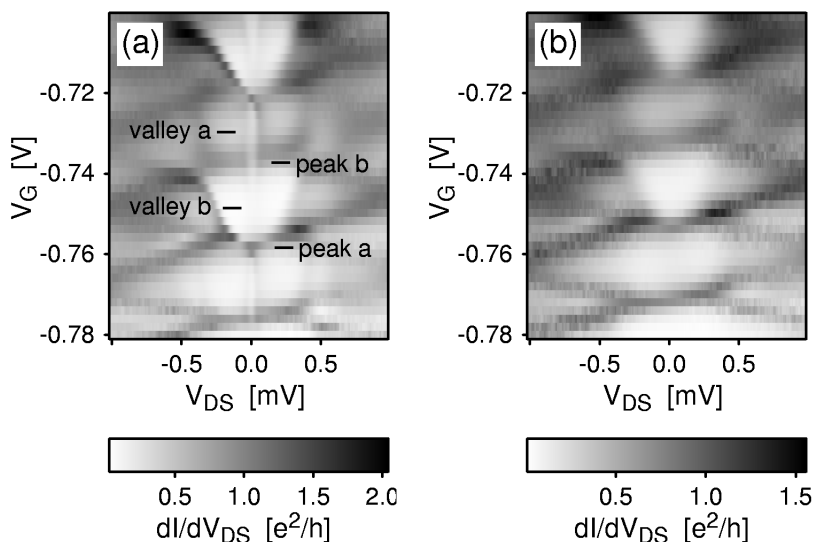


Figure 60: Temperature dependence of the split resonances. (a) At 25 mK the resonances are visible for parameters corresponding to Figure 57(b). At 400 mK the split resonances are gone.

These observations are at present not understood, however, the system is sufficiently well controlled to warrant further analysis. This analysis would have to include more than one level and different tunnel-couplings, otherwise the qualitatively different single-particle resonances and the asymmetry of the low conductance valleys can not be explained, i. e. the analysis has to go beyond the Anderson impurity model.

## 6.6 Other observations

Thus far, we have studied the typical case, the observation of spin-split Kondo resonances, in a situation in which the dot is far away from a transition in its internal state. However, we do not want to disregard measure-

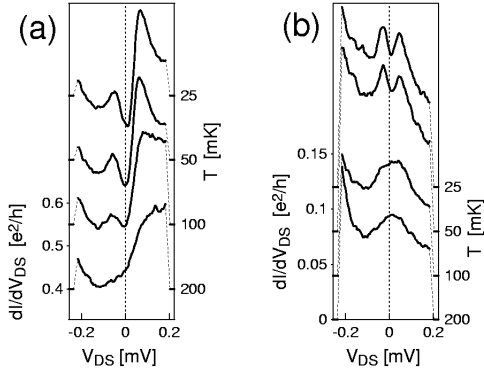


Figure 61: Temperature dependence of the split resonances for gate voltages as indicated in Figure 60; (a) for a high conductance valley (“valley a”), (b) for a low conductance valley (“valley b”). The  $dI/dV_{DS}$  scale belongs to the  $T = 200\text{mK}$  data, the other traces are offset as indicated by the temperature value.

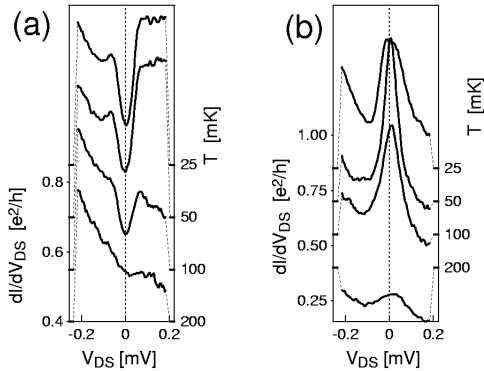


Figure 62: Temperature dependence for gate voltages corresponding to the single-particle resonances at the gate voltages indicated in Figure 60; (a) for singly occupying a new level with Landau index 0 (“peak a”), (b) for adding the second electron to a level with Landau index 0 (“peak b”).

ments that were taken closer to transitions in the electron configuration. A set of data covering a parameter range between adding the first and the second electron to a higher Landau level is given in Figure 64. The gate voltage  $V_G$  and the magnetic field  $B$  were varied together along the lines indicated in Figure 63. The total electron numbers in the central CB valley is ten, there is one electron in a level with higher Landau index, such that the valley has an odd number of electrons in the lowest Landau level and is a high conductance valley. It can be seen that over some parameter range, i. e. Figure 64(d-h), the picture given above holds. As one gets close to (Figure 64(b,i)) or across (Figure 64(a)) the transition in the electron configuration, the behavior is much more complicated.

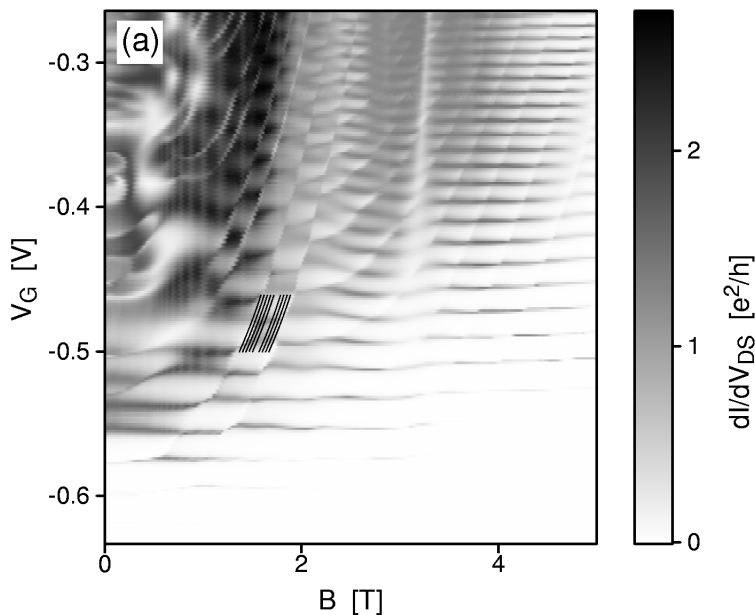


Figure 63: Same data as Figure 55. The lines mark the curves along which the data in Figure 64 are taken. The two valleys correspond to 10 and 11 electrons on the dot according to the evaluation presented in section 6.3.

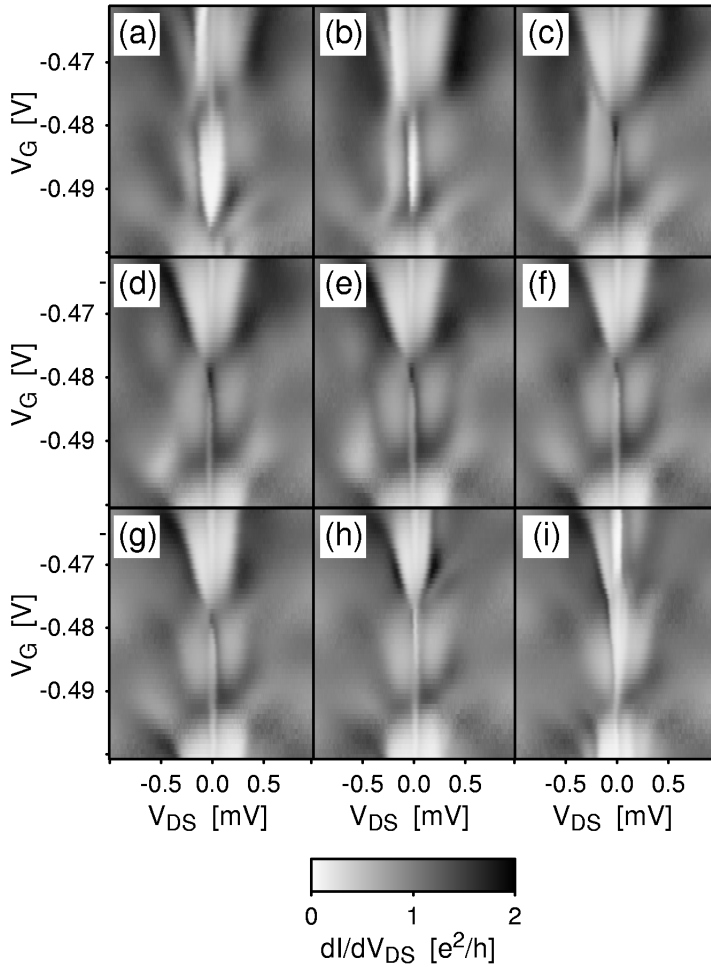


Figure 64: Evolution of a high and a low conductance valley between two transitions in the occupation of a level with higher Landau index. (a) corresponds to the curve for the lowest magnetic field in Figure 63, (i) to the highest.

## 6.7 Summary

The data presented in this chapter relate transitions in the internal state of a quantum dot — induced by the magnetic field — to a regular pattern in the conductance of the Coulomb blockade valleys. High conductance valleys occur for an odd number of electrons with Landau index 0 and *not* for an odd *total* number of electrons. To understand this observation it is essential to take into account that the tunnel-coupling is not the same for different states. The occurrence of Kondo resonances in two consecutive valleys with the electron numbers seven and eight could be understood.

Split Kondo resonances are observed across the high conductance valleys and into the neighboring low conductance valley at temperatures below 200 mK. The data also exhibit a marked difference between the single-particle resonances for adding an odd electron to the dot and adding an even electron to the dot. If one assumes the same tunnel-coupling for all states with the lowest Landau index, this is not consistent with the expected symmetry.

## 7 Conclusion

In this thesis, electrical transport through split gate quantum dots was studied with a special emphasis on the case of strong tunnel-coupling to the leads. The main objective of this thesis, the study of correlations predicted for the Anderson impurity model and the non-perturbative effects on the transport properties of the quantum dots, could be reached.

Resonances in the differential conductance through the quantum dot at zero drain-source voltage were identified as Kondo resonances as predicted for the Anderson impurity model. It was found by studying their splitting with magnetic fields, that the Kondo resonances are due to a spin degeneracy.

The temperature dependence of one Kondo resonance could be compared to theoretical predictions and it was found that the predicted universal scaling is applicable to our data, but that there are quantitative differences that can be described in terms of a deviation in the Kondo temperature.

Previous work [64, 45, 48] expected and reported an odd-even behavior in the total number of electrons on the dot for the occurrence of Kondo resonances based on a simple model of consecutively filling single-particle levels. This was in contradiction to other previous experiments reporting the importance of Hund's rules for the occupation of levels in quantum dots and could be disproved by our experiments. Instead, we have been able to identify the electronic states on the dot and come to the conclusion that an odd number of electrons in a strongly tunnel-coupled "outer shell" is responsible for the Kondo resonances observed. This observation has been verified in the meantime on a larger quantum dot [90].

Of course, this thesis also leaves open questions. One very interesting point is the quantitative comparison of our results to the universal temperature dependence predicted for the Anderson impurity model. The exact knowledge of this curve is needed for many experiments and it is still under theoretical investigation. In particular it would be interesting to know, whether the observed quantitative deviation in the Kondo temperature is due to a deviation of the quantum dot from the model — such a deviation should be different for different quantum dots — or if there is a more fundamental problem. In addition to this, it would be desirable to extend the range of available data to lower reduced temperatures. In the experiment, this translates to a call for smaller dots and lower electron temperatures.

A more detailed study of the regions where the internal state of the dot undergoes a transition would also be feasible in our samples. This

potentially allows studying more complicated systems like the two channel Kondo model, which is of theoretical interest. However, as we have seen in our experiments, it is necessary to consider different tunnel-couplings of the different states involved.

Finally, a point that is easy to realize in experiment and hard to consistently describe in theory is the transition from a closed dot with an integer number of electrons to an open system. Some of the data we have taken in this parameter range show a beautiful symmetry, but we were not able to give a good explanation for these observations.

## 8 Deutsche Zusammenfassung

### 8.1 Einleitung

In den letzten Jahren ist es gelungen, Einzel-Elektronen-Transistoren zu untersuchen. Der technologische Fortschritt in zwei Gebieten hat wesentlich dazu beigetragen, daß dies möglich wurde: Die Lithographie erlaubt heute die Herstellung von Strukturen im Nanometerbereich und in  $^3\text{He} - ^4\text{He}$  Mischungskryostaten sind Temperaturen von einigen Millikelvin erreichbar. Der wesentliche Effekt, der im Transport durch Einzel-Elektronen-Transistoren beobachtet wird, ist die diskrete Natur der elektrischen Ladung auf einer mikroskopischen Insel, was zu Coulomb-Lücken im Energiespektrum und zur Coulomb-Blockade des elektrischen Transports führt. Verschiedene Inseltypen wurden in der Literatur untersucht, kleine Metallpartikel, Nanotubes aus Kohlenstoff, sowie Inseln aus Halbleitermaterialien. Bei Inseln aus Halbleitermaterialien ist es möglich Strukturen herzustellen, deren Größe mit der Fermi-Wellenlänge vergleichbar ist und das diskrete Energiespektrum der Zustände im Einschlußpotential wird im elektrischen Transport sichtbar. Proben, die Coulomb-Blockade und ein diskretes Energiespektrum zeigen, werden im folgenden Quantenpunkte ("quantum dots") genannt und bilden die Grundlage dieser Arbeit.

Coulomb-Blockade ist gut verstanden für den Fall, daß die Insel schwach an die Zuleitungen angekoppelt ist. Inzwischen gibt es sogar schon Anwendungen von Einzel-Elektronen-Transistoren, und zwar als Stromnormal und als empfindliche Elektrometer. In dieser Arbeit soll ein Einzel-Elektronen-Transistor verwendet werden um grundlegende physikalische Fragestellungen zu untersuchen: Hauptziel dieser Arbeit ist es, einen Quantenpunkt als experimentelle Realisierung des Anderson-Störstellen-Modells zu verwenden und Korrelationseffekte zwischen den Elektronen auf dem Quantenpunkt und den Elektronen in den Zuleitungen im Stromtransport zu untersuchen. Das Anderson-Störstellen-Modell ist einfach. Es beschreibt ein spinentartetes Niveau, das an ein Reservoir von Elektronen tunnelgekoppelt ist. Es wurde in der Festkörperphysik ausgiebig untersucht, wobei ein atomares Niveau die Störstelle bildete. In unserem Fall wird der Quantenpunkt die Rolle einer kontrollierbaren Störstelle übernehmen.

Das Interesse an diesem Modell ist darauf zurückzuführen, daß es trotz seiner Einfachheit unerwartete Lösungen hat. Experimentell wurde in den 30er Jahren eine Tieftemperaturanomalie im Widerstand von Edelmetallen mit Verunreinigungen gefunden. Dieser Effekt heißt heute Kondo-Effekt

nach Jun Kondo, der ihn als Korrelationseffekt von Leitungsbandelektronen aufgrund von lokalisierten Spins erklärte. Dies geschah im Kondo-Modell, das eng mit dem Anderson-Störstellen-Modell verwandt ist.

Bei tiefen Temperaturen werden nämlich Korrelationen zwischen den Elektronen auf dem Quantenpunkt und in den Zuleitungen wichtig, der Übergang geschieht auf einer neuen Energieskala, der Kondo-Temperatur, die nicht-trivial von den Modellparametern abhängt. Trotz 40 Jahren theoretischen Interesses, bleibt die numerische Renormierungsgruppe, für die Wilson 1982 seinen Nobelpreis bekam, die einzige Methode, um den gesamten Temperaturbereich auf einer einheitlichen Grundlage zu untersuchen.

Auf einer grundlegenden Ebene berührt unser System die Frage nach dem Meßprozeß in der Physik. Die Zuleitungen, die an den Quantenpunkt tunnelgekoppelt werden, stellen den Meßaufbau dar und können als Störung des zu untersuchenden Systems — des Quantenpunkts — gesehen werden. Wenn man diese Störung klein macht, würde man naiverweise erwarten, daß man mit zunehmender Genauigkeit das Spektrum des ungestörten Quantenpunkts beobachten kann. Die Rechnungen zum Anderson-Störstellen-Modell sagen aber, daß dies am absoluten Temperatur-Nullpunkt nicht zutrifft; selbst eine verschwindend kleine Störung aufgrund der Tunnelkoppelung verändert das System qualitativ.

## 8.2 Übersicht über die einzelnen Kapitel

### 8.2.1 Probenstruktur und Coulomb-Blockade

In Kapitel 2 wird die Probenstruktur beschrieben und das Konzept des Einzel-Elektronen-Tunnels sowie der Transportspektroskopie eingeführt.

Als Probensubstrat dient eine GaAs/AlGaAs-Heterostruktur mit einem zweidimensionalen Elektronensystem (2DES) 50 nm unter der Oberfläche. Dieses 2DES wird lateral durch selektive Verarmung strukturiert, d. h. es werden metallische Elektroden (*gates*) mit Abmessungen im Bereich von 100 nm, aufgebracht. Beim Anlegen genügend hoher negativer Spannungen an diese Elektroden werden die Elektronen aus den 2DES-Bereichen unterhalb der Elektroden verdrängt. Auf diese Weise erhält man einen nahezu isolierten 2DES-Bereich (*Quantenpunkt*), der über kontrollierbare Tunnelbarrieren an zwei große 2DES Bereiche (*source* und *drain*) angekoppelt ist, die als Zuleitungen dienen. Dies ist in Abbildung 3 dargestellt.

Im Folgenden wird der Transport durch eine solchen fast Quantenpunkt diskutiert. Dazu wird die Einzelektronen-Näherung eingeführt, die die Annahme macht, daß das Tunneln in Form von unabhängigen Tunnelereignis-

sen einzelner Elektronen geschieht, wobei jedes Tunnelereignis die Energieerhaltung erfüllen muß. Außerdem braucht man ein Modell für die Energien der Elektronen in dem isolierten Bereich. Wir verwenden das sogenannte *Constant interaction model*, das die Energien der Elektronen in einen äußeren Beitrag aufgrund ihrer Ladung (Coulomb-Energie) und einen inneren Beitrag aufgrund von Einteilchenniveaus unterteilt. Solange die Coulombenergie der dominierende Beitrag ist, ergeben sich aus diesen Annahmen regelmäßige rautenförmige Bereiche, in denen eine bestimmte Elektronenzahl stabil gegen Einzelelektronentunneln ist. Dies stimmt gut mit den Beobachtungen für schwach tunnelgekoppelte Quantenpunkte überein. Die Einzelelektronennäherung setzt aufgrund der Heisenbergschen Unschärfere-lation ausreichend hohe Tunnelbarrieren voraus, was nach Ungleichung (11) abgeschätzt werden kann. Außerdem muß die Temperatur niedrig sein damit thermische Anregungen nicht zu einer Änderung der Elektronenzahl auf dem Quantenpunkt führen können.

Die Energien, bei denen ein zusätzliches Elektron auf den Quantenpunkt gebracht werden kann, lassen sich als Linien in einem Energiespektrum des Quantenpunkts darstellen. Die Tunnelkopplung an die Zuleitungen führt zu einer endlichen Lebensdauer und damit zu einer Verbreiterung dieser Linien. Als einfachste Annahme kann man davon ausgehen, daß es sich um eine Lorentz-artige Verbreiterung handelt (für ein einziges Niveau wäre das exakt). Wenn nun die Fermikanten schmal sind im Vergleich zu dieser Verbreiterung, kann man mit ihnen die Form dieser Linie abtasten. Der Strom stellt dabei eine integrierte Größe dar. Seine Ableitung nach der Transportspannung, der differentielle Leitwert, ist eng mit dem Spektrum des Quantenpunkts verwandt.

### 8.2.2 Resonanzen im Bereich der Coulomb-Blockade

In Kapitel 3 werden Messungen gezeigt, die qualitative Abweichungen vom typischen Bild des Einzel-Elektronen-Tunnels zeigen. Diese treten im Bereich starker Tunnelkopplung auf. Wiederholt wurde eine Resonanz bei verschwindender Transportspannung (d.h. die Position ist unabhängig von der "gate"-Elektroden Spannung, im Gegensatz zu den Einteilchenresonanzen) beobachtet. Diese erstreckt sich über einen Coulomb-Blockade-Bereich, zeigt eine ungewöhnlich Temperaturabhängigkeit und spaltet mit dem Magnetfeld auf. Dieser Typ von Resonanz wird im Folgenden als Kondo-Resonanz identifiziert und näher untersucht. Daneben gab es bei zwei Proben Resonanzen im Coulomb-Blockade-Bereich, die ein ähnliches Verhalten

zeigen aber eine leichte “gate”-Spannungsabhängigkeit haben. Außerdem zeigen wir Messungen, die eine ausgeprägte Symmetrie an dem Punkt zeigen, wo die Ladungsquantisierung verloren geht.

### 8.2.3 Das Anderson-Störstellen-Modell

In Kapitel 4 wird das Anderson-Störstellen-Modell [22] mit einer Erweiterung auf zwei Zuleitungen beschrieben, die Vorhersagen für dieses Modell werden zusammengefaßt. P. W. Anderson führte das nach ihm benannte Modell 1961 ein, um die Auswirkungen von magnetischen Fremdatomen auf nichtmagnetische Metalle zu beschreiben (*dilute magnetic alloys*). Die Elemente des Modells sind ein einzelnes (spin-)entartetes Niveau des Fremdatoms, die Tunnelkopplung dieses Niveaus an die Leitungsbandelektronen des Wirtsmetalls und die Coulombwechselwirkung zwischen zwei Elektronen auf dem lokalisierten Niveau. Die Anomalien im Widerstand solcher verunreinigter Metalle [51, 52] konnten zunächst von Jun Kondo [53] als Korrelationseffekt aufgrund von Streuung an lokalisierten Spins erklärt werden und tragen seinen Namen. Schrieffer et al. [54] konnten zeigen, daß das Kondo-Modell für bestimmte Parameter dem Anderson-Störstellen-Modell äquivalent ist, daher der Name “Kondo-Effekt” für die Hauptvorhersagen für das Anderson-Störstellen-Modell.

Es stellte sich heraus, daß dieses Modell auch auf Tunnelbarrieren mit einem Ensemble von Störstellen ([55, 56]) angewandt werden kann und es wurde von einem Experiment mit einer einzelnen Störstelle berichtet [57]. 1988 erkannten Glazman, Raïkh, Ng und Lee [46, 47], daß dieses Modell auch für Quantenpunkte relevant ist, wobei der Quantenpunkt die Rolle einer kontrollierbaren Störstelle übernimmt. Über die ersten Beobachtungen von Kondo-Resonanzen an Quantenpunkten wurde 1998 von anderen Autoren [45, 48] und im Zusammenhang mit dieser Arbeit [58] berichtet.

In dieser Zusammenfassung soll nur bemerkt werden, daß sich das Anderson-Störstellen-Modell bei niedrigen Temperaturen unterhalb der sogenannten Kondo-Temperatur grundsätzlich anders verhält als man es für Einzel-Elektronen-Tunneln erwarten würde. Dieses qualitativ unterschiedliche Verhalten führt zu klaren experimentellen Signaturen:

- Eine neue Resonanz erscheint im differentiellen Leitwert bei verschwindender Transportspannung,  $V_{DS} = 0$ , wenn das entartete Niveau einfach besetzt ist.
- Diese Resonanz im differentiellen Leitwert als Funktion von  $V_{DS}$  spal-

tet auf, wenn die zugrunde liegende Entartung aufgehoben wird.

- Im Kondo-Regime, dem Parameterbereich wo nur die Besetzung mit einem Elektron eine Rolle spielt, läßt sich der Leitwert bei  $V_{DS} = 0$  durch eine universelle Kurve beschreiben.

Allerdings sind diese Korrelationseffekte nur bei sehr tiefen Temperaturen beobachtbar, die Temperaturskala wird durch die Kondo-Temperatur festgelegt, die exponentiell von der Tunnelkopplung abhängt. Im Experiment muß man also zum Bereich starker Tunnelkopplung gehen, jedoch geht für zu starke Tunnelkopplung die Ladungsquantisierung verloren.

Es ist auch wichtig, die Unterschiede zwischen einem Quantenpunkt und dem Anderson-Störstellen-Modell zu betonen. Insbesondere können sich auf einem Quantenpunkt mehr als 0, 1 oder 2 Elektronen befinden. Das Modell sollte für alle Elektronenzahlen anwendbar sein für die es eine Entartung gibt. Allerdings gibt es mit Sicherheit angeregte Zustände für diese Elektronenzahlen, die nicht im Modell berücksichtigt werden.

### 8.2.4 Auswertung der beobachteten Kondo-Resonanzen

Aufgrund der Übereinstimmung zwischen den Vorhersagen für das Anderson-Störstellen-Modell und einigen der in Kapitel 3 vorgestellten Beobachtungen nennen wir von nun an Resonanzen im differentiellen Leitwert bei  $V_{DS} = 0$ , die sich bei tiefen Temperaturen entwickeln und die in einem Magnetfeld aufspalten, Kondo-Resonanzen.

Kapitel 5 gliedert sich in zwei Teile. Im ersten Teil wird die Aufspaltung der Kondo-Resonanzen im Magnetfeld untersucht, im zweiten Teil wird die Temperaturabhängigkeit des differentiellen Leitwerts ausgewertet.

Im Magnetfeld ist bei unseren Proben eine starke Richtungsabhängigkeit zu erwarten: Eine Magnetfeldkomponente senkrecht zu der Ebene des 2DES wird einen starken Einfluß auf die Bahnbewegung der Elektronen haben, während das gesamte Magnetfeld an den Elektronenspin ankoppelt. Die ersten Experimente wurden daher in einem Magnetfeld parallel zu dem 2DES durchgeführt, um den einfachst möglichen Fall einer Kopplung ausschließlich an den Spin zu realisieren. Dabei stellte sich heraus, daß die beobachtete Aufspaltung der Kondo-Resonanzen der Zeemannenergie entspricht, die für den Landé  $g$ -Faktor von Galliumarsenid zu erwarten ist. Als nächstes wurde untersucht, wie diese Aufspaltung vom Winkel zwischen Probe und Magnetfeld abhängt. Es stellte sich heraus, daß keine Abhängigkeit

der Aufspaltung vom Winkel zwischen Probe und Magnetfeld besteht, woraus folgt, daß die beobachteten Kondo-Resonanzen auf eine Spinentartung zurückzuführen sind.

Im zweiten Teil von Kapitel 3 wird dann eine Kondo-Resonanz quantitativ mit der Vorhersage einer universellen Temperaturabhängigkeit für das Anderson-Störstellen-Modell verglichen. Dazu werden die Parameter des Systems, insbesondere die Coulomb-Wechselwirkung  $U$ , die Tunnelkopplung  $\Gamma$  und die Energie  $\varepsilon$  des Niveaus aus den Daten bei hohen Transportspannungen  $V_{\text{DS}}$  gewonnen (dies setzt eine wohldefinierte Coulomb-Blockade-Raute voraus, weshalb eine solche Auswertung bei anderen Kondo-Resonanzen nicht möglich war). Dabei wird angenommen, daß Korrelationseffekte bei diesen hohen Energien vernachlässigt werden können. Damit sind die Parameter des Anderson-Störstellen-Modells festgelegt und die Vorhersage des Modells für  $V_{\text{DS}} = 0$ , die universelle Temperaturabhängigkeit, kann mit den Beobachtungen bei  $V_{\text{DS}} = 0$  verglichen werden. Dazu wird die Kondo-Temperatur nach Gleichung (29) für jeden Wert der “gate”-Spannung berechnet und die Daten über der reduzierten Temperatur  $T/T_K$  aufgetragen. Das Ergebnis in Abbildung 45 zeigt, daß zwar die Skalierung der Daten auf eine universelle Kurve möglich ist, daß es jedoch eine Abweichung zwischen Theorie und Experiment gibt. Diese Abweichung kann gut durch eine um einen Faktor 1.66 höhere Kondo-Temperatur im Experiment beschrieben werden. Die Ursache für die Abweichung ist zu diesem Zeitpunkt unklar. Eine mögliche Erklärung sind Unterschiede zwischen dem Quantenpunkt und dem Anderson-Störstellen-Modell. Es gibt Rechnungen, die zeigen, daß weitere Zustände auf dem Quantenpunkt zu höheren Kondo-Temperaturen führen können [80].

### 8.2.5 Kondo-Resonanzen und Elektronenkonfiguration auf dem Quantenpunkt

In Kapitel 6 wird die Frage untersucht, für welche Elektronenzahlen auf dem Quantenpunkt Kondo-Resonanzen auftreten. Im vorhergehenden Kapitel wurde festgestellt, daß die beobachteten Kondo-Resonanzen auf eine Spinentartung für eine bestimmte Elektronenzahl auf dem Quantenpunkt zurückzuführen sind. Jedoch können für jeden Quantenpunkt mehrere Coulomb-Blockade-Bereiche mit verschiedenen Elektronenzahlen beobachtet werden. Um eine Aussage über die Entartung zu machen, muß man das Energiespektrum des Quantenpunkts im Detail untersuchen. Wir finden ein regelmäßiges Muster im Auftreten von Kondo-Resonanzen, diese

sind bei endlichem Magnetfeld aufgespalten.

In diesem Zusammenhang gibt es zwei Gruppen von früheren Arbeiten. Zum einen wurden die Energiespektren von Quantenpunkten untersucht [11, 12, 13, 87, 86] und festgestellt, daß sich bestimmte Quantenpunkte durch ein mehr oder weniger kompliziertes Füllen von Einteilchenzuständen beschreiben lassen, wobei die Hund'schen Regeln eine Rolle bei der Reihenfolge spielen. Zum anderen werden Kondo-Resonanzen für eine ungerade Zahl von Elektronen auf dem Quantenpunkt erwartet [64] und es gibt auch zwei Experimente, die diese Erwartung zu bestätigen scheinen. Allerdings basiert die Aussage im ersten Experiment [45] nur auf zwei Coulomb-Blockade-Bereichen mit Kondo-Resonanzen und die Temperaturabhängigkeit im zweiten Experiment [48] ist nicht eindeutig. Die Erwartung von Kondo-Resonanzen für ungerade Elektronenzahlen widerspricht den früheren Experimenten, denn sie basiert auf folgenden Annahmen:

- Eine Spinentartung führt zu einer Kondo-Resonanz.
- Für eine ungerade Elektronenzahl gibt es einen ungepaarten Spin auf dem Quantenpunkt und daher eine Spinentartung.

Die erste Annahme ist unvollständig, da sie die Bedeutung der Tunnelkopplung vernachlässigt. Selbst für den Fall einer Spinentartung entscheidet die Kondo-Temperatur, die exponentiell von der Tunnelkopplung abhängt, darüber, ob eine Kondo-Resonanz beobachtet wird. Die zweite Annahme ist falsch, wie die früheren Experimente zu den Quantenpunktspektren zeigen.

Unsere experimentelle Beobachtung von zwei Kondo-Resonanzen in aufeinanderfolgenden Coulomb-Blockade-Bereichen (Abbildung 54) zeigt direkt, daß Kondo-Resonanzen nicht an eine ungerade Zahl von Elektronen gebunden sind.

Um das Auftreten von Kondo-Resonanzen zu verstehen, muß man wissen, in welchen Zuständen sich die Elektronen auf dem Quantenpunkt befinden. Dazu braucht man zunächst Namen für die Zustände. Dafür gehen wir von den Einteilchenzuständen in einem zweidimensionalen harmonischen Oszillator im Magnetfeld aus. Dieses Problem wurde schon 1928 von Fock [84] gelöst und man kann als eine Quantenzahl den Landau-Index wählen. Unsere Messungen in einem Magnetfeld senkrecht zum Quantenpunkt (Abbildungen 55 und 56) lassen sich anhand dieser Quantenzahlen interpretieren. Mit ansteigendem Magnetfeld werden zunächst alle Elektronen in Zustände mit Landau-Index 0 umverteilt. In diesem Bereich gibt

es ein Schachbrettmuster für den differentiellen Leitwert in den Coulomb-Blockade-Tälern. Die Täler mit hohem Leitwert zeigen deutliche aufgespaltene Kondo-Resonanzen. Diese Täler können einer ungeraden Anzahl von Elektronen mit Landau-Index 0 zugeordnet werden. Wird das Magnetfeld weiter erhöht, so bleiben die Elektronen in Zuständen mit Landau-Index 0, aber die Spinpolarisation nimmt zu. Anhand dieser Spinflips kann die Elektronenzahl bestimmt werden.

Untersuchungen von McEuen [86] haben gezeigt, daß Zustände mit Landau-Index 0 größeres Gewicht am Rand des Quantenpunktes haben und damit stärker an die Zuleitungen tunnelgekoppelt sind. Damit wird das Muster im Auftreten von Kondo-Resonanzen verständlich: Verantwortlich sind Spinarten in stark tunnelgekoppelten "äußeren" Zuständen.

### 8.3 Zusammenfassung und Ausblick

In dieser Arbeit wurde der Transport durch Quantenpunkte untersucht mit besonderem Augenmerk auf den Bereich starker Tunnelkopplung an die Zuleitungen. Das Hauptziel, die Untersuchung von Korrelationseffekten, wie sie für das Anderson-Störstellen-Modell vorhergesagt werden, wurde erreicht.

Resonanzen im differentiellen Leitwert durch den Quantenpunkt bei verschwindender Transportspannung konnten als Kondo-Resonanzen identifiziert werden. Die Aufspaltung der Kondo-Resonanzen im Magnetfeld ließ darauf schließen, daß eine Spinartung den beobachteten Kondo-Resonanzen zugrunde liegt.

Die Temperaturabhängigkeit einer der beobachteten Kondo-Resonanzen konnte mit theoretischen Vorhersagen verglichen werden, und es stellte sich heraus, daß das vorhergesagte Skalierungsverhalten auf unsere Daten anwendbar ist. Allerdings gibt es quantitative Abweichungen, die als eine Abweichung in der Kondo-Temperatur um einen konstanten Faktor beschrieben werden können.

Vorausgehende Arbeiten haben Kondo-Resonanzen für eine ungerade Zahl von Elektronen auf dem Quantenpunkt vorhergesagt und von entsprechenden experimentellen Ergebnissen berichtet. Diese Erwartung basiert auf einer zu starken Vereinfachung für die Besetzung der Niveaus auf dem Quantenpunkt und steht im Widerspruch zu anderen Untersuchungen an Quantenpunkten, in denen die Hund'schen Regeln wichtig sind. Die Kopplung von Kondo-Resonanzen an eine ungerade Zahl von Elektronen auf dem Quantenpunkt konnte durch unsere Ergebnisse widerlegt werden. Stattdes-

sen stellte sich heraus, daß das Auftreten von Kondo-Resonanzen mit einer ungeraden Zahl von Elektronen in einer stark tunnelgekoppelten äußeren Schale korreliert werden kann. Dies wurde inzwischen in Experimenten an einem anderen Typ von Quantenpunkt bestätigt [90].

Selbstverständlich lassen die hier vorgestellten Ergebnisse auch noch Fragen offen. Ein sehr interessanter Punkt ist der quantitative Vergleich unserer Ergebnisse mit der für das Anderson-Störstellen-Modell vorhergesagten universellen Temperaturabhängigkeit. Die genaue Kenntnis dieser Kurve ist für viele Experimente von Bedeutung und wird immer noch theoretisch untersucht. Insbesondere wäre es interessant zu wissen, ob die beobachtete quantitative Abweichung von den Vorhersagen auf eine Abweichung unseres Quantenpunkts vom Modell zurückzuführen ist — eine solche Abweichung sollte von Quantenpunkt zu Quantenpunkt verschieden sein — oder ob es sich um ein grundlegenderes Problem handelt. Außerdem wäre es wünschenswert, zu niedrigeren reduzierten Temperaturen vorzustoßen. Experimentell bedeutet dies kleinere Quantenpunkte und niedrigere Elektronentemperaturen.

Das Thema, das einer eingehenderen Untersuchung bedarf, ist der Bereich der Übergänge der inneren Zustände des Quantenpunktes. An diesen Übergangspunkten kommt es nämlich neben der Spinentartung zu einer einstellbaren orbitalen Entartung und es ist denkbar, ein Zweikanal-Kondoproblem experimentell zu realisieren, was vom theoretischen Standpunkt aus interessant wäre. Allerdings ist anzumerken, daß in unseren Experimenten die Tunnelkopplung an die beteiligten Orbitale unterschiedlich ist.

In unseren Experimenten läßt sich der Übergang von einem quasi-isolierten Quantenpunkt mit diskreter Elektronenzahl zu einem offenen System leicht verwirklichen, allerdings gibt es keine Theorie, die diesen Parameterbereich konsistent beschreibt. Einige unserer Daten zeigen an diesem Übergang eine ausgeprägte Symmetrie und in diesem Bereich erscheinen weitere Untersuchungen lohnenswert.

## A Acknowledgments

I want to acknowledge the support of many people, without whom this work would not have been possible.

**Jürgen Behring** helped with mounting the  $\pi$ -filters.

**Karl Eberl** supplied MBE grown sample substrates.

**Ulf Graumann** optimized the ohmic contacts to the 2DES.

**Klaus von Klitzing** discussed results with me and signed all blue order forms without complaints.

**Daniela Pfannkuche** answered many questions about quantum dots. She was also busy solving and creating computer problems.

**Thomas Reindl** analyzed samples with the SEM.

**Monika Riek** assisted with processing and bonding the samples.

**Frank Schartner** bonded samples and made optical masks.

**Alice and Gerhard Schmid**, my parents, proof-read the manuscript.

**Manfred Schmid** was the first address for all mechanical issues and helped with the rotating probe.

**Herbert Schoeller** got me interested in the subject.

**Linus Torvalds** and all the contributors to Linux across the internet provided an operating system that allowed 24/7 operation and the collection of 10646215367 bytes of data.

**Ulrike Waizmann** assisted with the electron-beam lithography, with analyzing samples with the SEM and was our reference for the Swabian language.

**Werner Wegscheider** supplied sample substrates that were, however, not used in the successful experiments.

**Jürgen Weis** was my supervisor and competent in all experimental and quantum-dot questions. He also read the manuscript for this thesis carefully.

**Ulf Wilhelm** was always ready for a long discussion on the fundamentals of quantum mechanics and operating systems. He also implemented the measurement software “measkern”, without which some of the measurements wouldn’t have happened.

**Michele Williams-Schmid**, my wife, was patient when I spent too much time at work and proof-read this manuscript.

Of course I want to thank all my colleagues for the good atmosphere at the institute. In case I have missed somebody in the list I kindly ask the person to not feel offended and blame it on my forgetfulness.

## B Fock-Darwin spectrum

The single-particle states of electrons in a two-dimensional system in the presence of a harmonic potential and a magnetic field have been calculated by Fock [84] and Darwin [85]. Here we want to present some results using the notation found in [91] without going through the calculation. The Hamiltonian is

$$H = \frac{1}{2m_e}(\vec{p} + \frac{e}{c}\vec{A})^2 - \frac{1}{2}m_e\Omega_0^2 r^2,$$

with the parameters  $\vec{A} = (B_\perp, 0, 0)$ , the confining potential  $\Omega_0$  and the effective mass  $m_{e,\text{GaAs}}$  for electrons in GaAs substituted for  $m_e$ .

The solutions can be labeled in terms of  $m \in \mathcal{Z}$ , the eigen values of the angular momentum in z-direction  $L_z$  and an index  $n_r \in \mathcal{N}$  for the radial part of the wavefunction. The corresponding eigen functions of the Hamiltonian in polar coordinates are

$$\psi_{m,n_r}(r, \varphi) = \psi_m(\varphi)\psi_{m,n_r}(r),$$

where

$$\psi_m(\varphi) = \frac{1}{\sqrt{2\pi}}e^{im\varphi}$$

and

$$\psi_{m,n_r}(\xi \times l) = \frac{\sqrt{2}}{l} \sqrt{\frac{n_r!}{(n_r + |M|)!}} e^{-\frac{1}{2}\xi^2} - \frac{1}{2}\xi^2 \xi^{|M|} L_{n_r}^{|M|}(\xi^2),$$

$$l = \sqrt{\frac{\hbar}{m_{e,\text{GaAs}}\omega_{\text{eff}}^2}},$$

$$\omega_{\text{eff}} = \sqrt{\Omega_0^2 + \frac{\omega_c^2}{4}},$$

with the energy eigen values

$$E_{mn_r} = \hbar\omega_{\text{eff}}(2n_r + |m| + 1) + \frac{m}{2}\hbar\omega_c.$$

However, one can also choose different quantum numbers to label the states:

$N_+$  and  $N_-$  which are related to the above mentioned eigen values:  $m = N_+ - N_-$ , and  $n_r = \min\{N_+, N_-\}$ . In terms of these, the eigen energies are

$$E_{N_+N_-} = \hbar\Omega_+(N_+ + 1/2) + \hbar\Omega_-(N_- + 1/2). \quad (34)$$

The energy  $\hbar\Omega_+ = \hbar\omega_{\text{eff}} + \omega_c/2$  approaches  $\omega_c$  for high magnetic fields and the energy  $\hbar\Omega_- = \hbar\omega_{\text{eff}} - \omega_c$  approaches zero.

The first way of labeling the states has its merits at low fields, here the energies are proportional to  $B$  and  $m$ . The second way of labeling the states has advantages at high fields, the energies become proportional to  $N_+$  and the cyclotron frequency  $\omega_c$ . It therefore makes sense to call  $N_+$  “Landau index” at higher magnetic fields.

## C Two-dimensional electron system

Two-dimensional electron systems and their behavior in magnetic fields are not fully understood. However, for many situations the picture of edge-channels [92, 93] and the Landauer-Büttiker [94, 95] formalism explain the experiments well. Even though the quantum dot is the main point of interest, the 2DES forms the leads and the effect of the magnetic field on the leads is observed in the experiments. This appendix contains an extremely short phenomenology of the edge-channel picture. It also contains data obtained for the 2DES and single quantum point contacts to support the interpretations for the quantum dot.

In the case of a quantum point-contact (QPC) defined by an appropriate voltage applied to one set of gate fingers, transport can be understood in terms of a single channel going through the point contact and the other channels going past the point contact undisturbed. In the case of a quantum dot, where single-electron tunneling is observed, we find no indication of channels going past the dot undisturbed for the relatively low magnetic fields studied in our experiments.

### C.1 Edge-channel picture

In a 2DES in a magnetic field there exist edge-channels that have a conductance of  $e^2/h$  and a direction. The filling-factor  $\nu_{2DES}$  can be different for different regions of the 2DES, the edge-channels are either transmitted or reflected at such a boundary.

The conductance of a geometry as depicted in Figure 65 is given by [93]

$$G_{1,4;2,3} = \frac{V_{2,3}}{I_{1,4}} = \frac{e^2}{h} \left( \frac{1}{\nu_{2DES 1}} - \frac{1}{\nu_{2DES 2}} \right)^{-1}$$

which, in the situation depicted in Figure 65, gives  $4/3 \times (e^2/h)$ .

### C.2 Application to a single point contact

In the case of a single quantum point contacts the 2DES is fully depleted below the gates (for gate voltages below  $\approx -0.3$  V) except for a small area close to the tips. This does not change the picture as long as one can determine a number of edge-channels that traverse the QPC. Figure 66 shows a measurement of the differential conductance as function of  $B_{\perp}$  and  $V_R$  (see Figure 81). Around the points marked by a,b,c there are areas

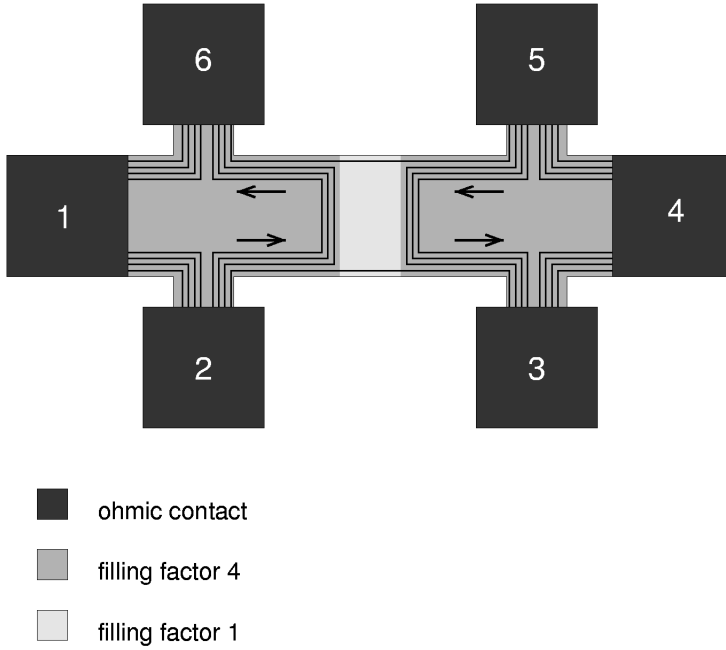


Figure 65: Schematic hall-bar in a perpendicular magnetic field; the light area in the middle corresponds to an area with lower electron density / higher filling factor. Such a geometry can be achieved by depletion via a gate.

of nearly constant differential conductance of  $2e^2/h$ ,  $1.5e^2/h$  and  $1.33e^2/h$  respectively. These values can be interpreted as one channel traversing the constriction and 2, 3 and 4 channels being present in the bulk. The Hall trace included in Figure 66 can be used to determine the transitions between different filling factors in the bulk. These agree well with the position of the boundaries a/b and b/c on the magnetic field axis.

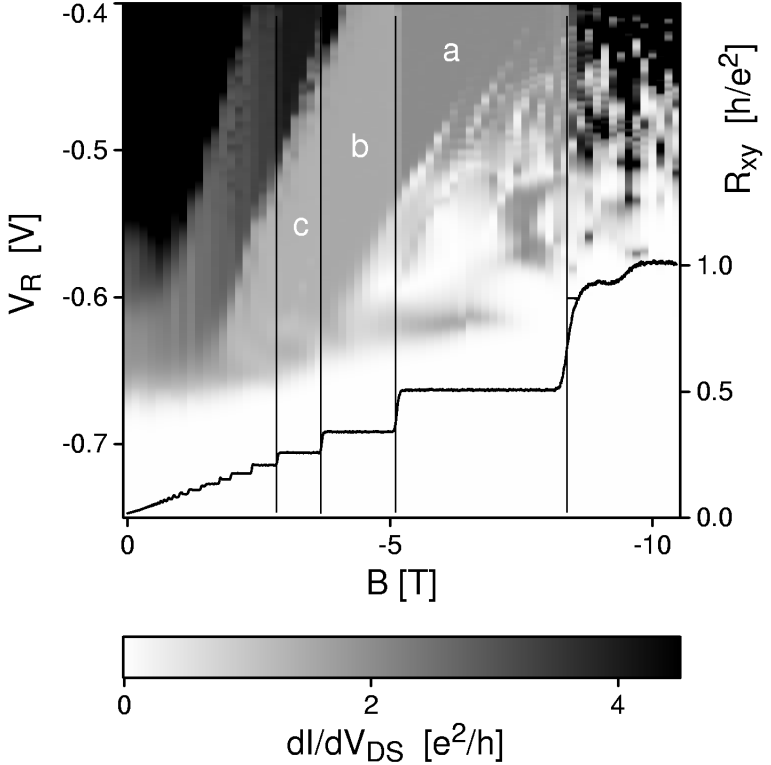


Figure 66: 4-point measurement of the differential conductance through a quantum-point contact. For reference a Hall curve is included.

These areas of nearly constant conductance are only present over a limited  $V_R$  range. More negative voltages pinch off the channel leading to zero conductance, more positive voltages lead to more channels being transmitted through the quantum point contact. Even though there are two features

in Figure 66 that could be interpreted as opening a second and third channel, the plateaus that would be expected are not observed clearly.

### C.3 Consequences for the quantum dot

The observations mentioned above make it necessary to consider the effect of the magnetic field on the leads when studying a quantum dot. In general, one would have to assume tunneling rates that are different for different edge channels. As an extreme (and simple) case, one can assume — in analogy to the observations on the quantum point contact — that a number of channels is tunnel-coupled to the SET (with constant tunnel-coupling) and that the rest of the channels is perfectly decoupled. Adding an additional edge channel that is perfectly decoupled would again lead to a step *with predictable height* in the differential conductance at the magnetic field of a quantum Hall transition in the drain and source parts of the 2DES. This is not observed in the experiments in the parameter range where Coulomb blockade occurs, which leads to the conclusion that the dot is not perfectly decoupled from some of the edge channels.

## D Sample preparation

In this section the preparation of the samples is described. It is meant to provide the information necessary to reproduce the samples used in the experiments presented in this thesis. To be able to use this information, one needs proper equipment and training. Reading this section is not necessary to understand the experiments.

Problems that had to be overcome during sample preparation are mentioned, but not all of them were studied in enough detail to be able to claim that the explanations for the undesired symptoms are correct and that the respective solutions are the only or the simplest possible solutions. Some parameters were changed in the course of this work, the figures mentioned are those for sample p11.5.1.

The samples are based on a two-dimensional electron system (2DES) that forms at an interface in a GaAs/AlGaAs heterostructure [33]. A region of 2DES (mesa) is isolated by etching and contacted with ohmic contacts. Finally, a patterned metal-layer is deposited on top of the heterostructure which is used in the experiments to locally deplete the 2DES. These gates have to bridge between the small dot structure — on the order of the Fermi wavelength, i.e. 100 nm — and the large pads for contacting the gates (100  $\mu\text{m}$  for wire bonding). Therefore, a two step process combining optical and electron-beam is necessary. The overall sample structure is similar to that of a field-effect transistor.

### D.1 Heterostructure

Even though the growth of modulation-doped [32] GaAs/AlGaAs heterostructures via MBE has become the standard way to obtain high quality 2DESs [33], the need for a 2DES close to the surface has led to problems that were not obvious from standard characterization, e.g. from Hall measurements.

**Problems:** Shallow (40 nm) heterostructures [96] with  $\delta$ -doping (the Si donors concentrated in one plane) displayed the following behavior: When a point contact was defined by applying a negative voltage to a pair of top gates, there was telegraph noise in the current through the point contact and the current increased on a timescale of hours. A possible explanation is that the donor layer was slightly conducting, leading to a screening of the gates on a long time scale. These shallow heterostructures also displayed a nonlinear dependence of the carrier density on the voltage applied to a large

area front gate. This also indicates a charge redistribution, possibly in the donor layer, due to the gate voltage and not just a depletion of charge in the plane of the 2DES.

The GaAs/AlGaAs heterostructure used in the successful experiments was grown at the *Max-Planck-Institut* in the group of Karl Eberl (substrate No. 8363). The layer sequence is given in Figure 67, the doping is continuous. For this heterostructure the carrier density depends linearly on a voltage applied to a large area front gate and the current through a point contact is stable in time.

It is not clear at this time, whether the kind of doping makes the difference.

## D.2 Cutting the samples

The wafer is cut into chips for further processing. As the properties of the 2DES are not necessarily uniform across a wafer, the positions of the samples on the wafer are given for completeness in Figure 68. No dependence on the wafer position was observed, but during later studies it was found that the crystallographic orientation could strongly influence the quality of the ohmic contacts.

The size of the samples was chosen as  $3\text{ mm} \times 4\text{ mm}$  which could be handled easily throughout the following processes.

## D.3 Mesa etching

In this step, separated areas of 2DES (mesas) are defined by optical lithography and etching. On each chip there are four equivalent mesas, the large dark areas in Figure 69 (a). Additional mesas are used for checking the ohmic contacts and for aligning the other process masks.

### Process:

1. *Clean*:<sup>3</sup>

- (a) Process the sample in acetone<sup>4</sup> in an ultra sonic basin for 2 min,

---

<sup>3</sup>This and other processes occur repeatedly. They are only described the first time they occur in the sequence of processes. Afterwards, cursive writing indicates that a step has been specified already.

<sup>4</sup>The chemicals used are of high purity e. g. VLSI acetone was used, but no record was kept on batch number or manufacturer.

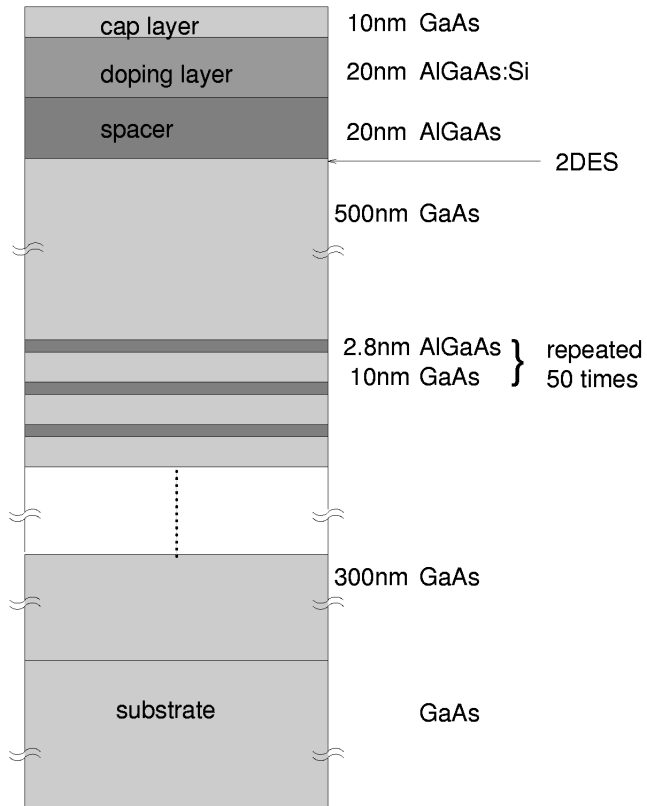


Figure 67: Layer sequence of the heterostructure used in the successful experiments.

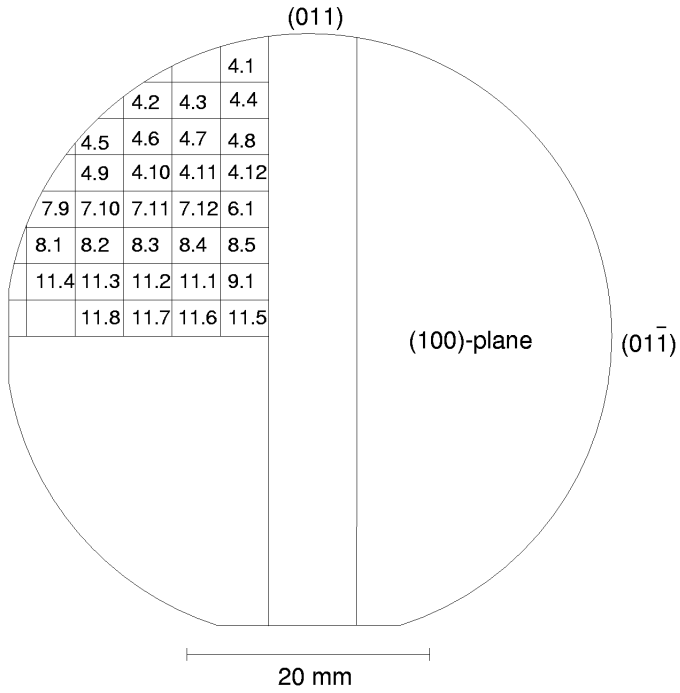


Figure 68: Map of the samples as cut from the heterostructure.

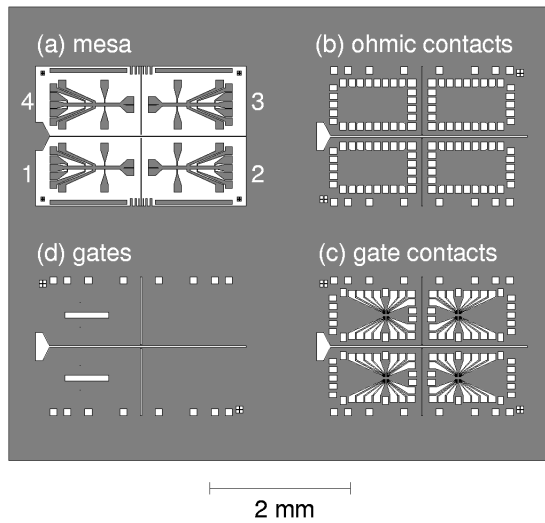


Figure 69: Chrome masks used for optical lithography. White corresponds to transparent in the mask, i.e. areas where the photoresist is exposed and removed in a positive process. Mask (d) is used for the characterization of heterostructures.

- (b) take the sample through three consecutive acetone baths,
- (c) splash with acetone;
- (d) do not let acetone dry on the sample when changing baths, keep it under propanol until ready for spin coating.

2. *Coat with photoresist:*

- (a) Use spin-coater 1001S /St146 (Convac),
- (b) adjust sample on acentric platter and blow dry with nitrogen,
- (c) apply a few drops of Microposit S1805 (Shipley) to the sample and spin at 4500 1/min for 30 s,
- (d) bake for 20 min in an oven at 85 °C.

3. *Expose photoresist* for 10 s with the 'mesa' mask (Figure 69(a)):

- (a) Use MJB3 mask aligner (300 nm–400 nm UV-light, made by Karl Suss).

4. *Develop photoresist:*

- (a) Dilute Microposit 351 developer 1 : 4 with DI-water,
- (b) shake sample in this mixture for 30 s,
- (c) remove developer by rinsing with DI-water,
- (d) blow dry with nitrogen.

5. *Etch:*

- (a) Mix  $\text{H}_2\text{O}:\text{H}_2\text{O}_2(31\%):\text{H}_2\text{SO}_4(96\%)$  at a ratio of 200 : 16 : 2 <sup>5</sup>,
- (b) dilute this mixture with DI-water at the ratio of 1 : 9;
- (c) etch each sample for 80 s in the resulting mixture, to obtain a depth of 60 nm;
- (d) rinse sample with DI water,
- (e) blow dry with nitrogen.

---

<sup>5</sup>All ratios are volume ratios.

## D.4 Alloyed ohmic contacts

In this step ohmic contacts to the 2DES are prepared. Metal pads of gold/germanium/nickel are deposited on parts of the mesa, then the sample is heated, melting the metal, dissolving part of the underlying mesa and forming an electric contact between the metal and the 2DES.

**Problems:** The quality of the “ohmic contacts” to the 2DES was not always satisfactory (a contact is considered good if it has a linear current-voltage characteristic  $V = R \times I$  at all temperatures and  $R < 100 \Omega$  at 4K). Non-linear behavior, i.e reduced conductance for small voltages, was especially visible at low temperatures ( $< 0.1\text{K}$ ) and became worse after the radio-frequency shielding was improved. This suggests that potential barriers close to the contacts cause the problem and that activated transport is taking place.

The work of Ulf Graumann lead to improved understanding as to which parameters are critical and to several changes in the process:

- The contact geometry is critical. The quality of the ohmic contacts depends strongly on the orientation of the GaAs crystal with respect to the border of the contact-pads. The resistance is inversely proportional to the length of this border. Therefore, the pads were changed to have longer borders and—more important—to include different crystal orientations as shown in Figure 70. It was already known that pads for ohmic contacts have to overlap the mesa edge to avoid decoupling at high magnetic fields (“Corbino geometry”).
- The surface of the sample before the deposition of the metal layers is critical. It was already known that a HCl-dip is needed to remove the oxide that forms on the sample surface. If the sample is left in air, the oxide builds up again, leading to contact and adhesion problems. Two more cleaning steps were added, but still some batches of samples fabricated in our clean room have serious adhesion problems. This is not understood, but did not affect the experiments discussed here.
- The composition of the metal layers is critical. In the beginning, gold and germanium were evaporated as an alloy, which lead to inconsistent results. Thereafter, gold and germanium were evaporated separately, allowing precise control over the composition. In all experiments, an eutectic composition of gold/germanium was used. It was found that

the thickness of the metal layer should be at least twice the depth of the 2DES below the surface. The amount of nickel is also critical, but has to be optimized for each heterostructure.

- The alloying itself is not critical; the temperature window for good contacts is large compared to the controllability of the oven.

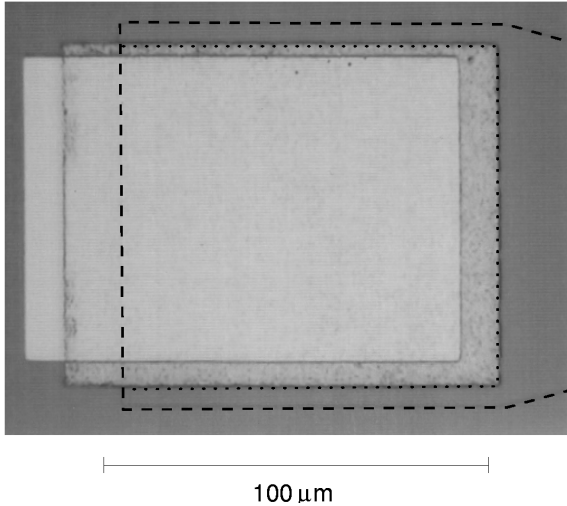


Figure 70: Ohmic contact: The outline of the mesa is marked by a dashed line. The alloyed metal provides contact to the 2DES along the dotted line, which includes different crystal orientations. The top layer is the “gate mask” metalization for easier bonding.

### Process:

1. *Clean.*
2. *Coat with photoresist.*
3. *Expose* for 25 s with the ‘contact’ mask (Figure 69(b)).
4. *Create undercut* (this step changes the profile of the photoresist after development to allow for an easier lift-off):
  - (a) Process sample in chlorobenzene for 3 min,

- (b) bake it for 10 min at 85 °C in an oven.
- 5. *Develop photoresist.*
- 6. Prepare surface for ohmic contacts:
  - (a) Process sample in an O<sub>2</sub> plasma (30 s, pressure 0.3 torr, power 200 W in a 100-EPLASMA SYSTEM from Technics Plasma GmbH),
  - (b) put sample in “semico clean” for 2 min;
  - (c) dip sample in HCl 30% for 2 s,
  - (d) rinse with DI water for 5 s,
  - (e) put it into evaporator within 5 min of HCl-dip.
- 7. Deposit metalization in Univex 450 evaporator (Leybold Heraeus) from thermal sources:
  - (a) 107.3 nm of Au at a rate of  $\approx 0.3$  nm/s,
  - (b) 52.9 nm of Ge at a rate of  $\approx 0.25$  nm/s,
  - (c) 40.8 nm of Ni at a rate of  $\approx 0.15$  nm/s.
- 8. *Lift-off:*
  - (a) Put sample into acetone, the photoresist dissolves and the metalization only sticks to the areas of the sample where there was no photoresist before evaporation,
  - (b) put into propanol,
  - (c) blow dry with nitrogen.
- 9. Alloy contacts in an annealing oven (AZ500 from MBE Komponenten GmbH) under forming gas at:
  - (a) 370 °C for 120 s, forming gas pressure 0.3 bar, no gas flow,
  - (b) 440 °C for 50 s, forming gas pressure 0.3 bar, no gas flow,
  - (c) cool down rapidly by turning on forming gas flow.

## D.5 Bond pads and gate leads

In this step, a metal layer is deposited that bridges between the structure size accessible to wire bonding and the field size accessible to e-beam lithography.

**Problems:** The resulting layer does not always stick well enough to the substrate to allow wire bonding. This problem is avoided in the newer mask by adding pads in the “ohmic contacts” mask below the bond areas. These alloyed pads form a solid base for bonding [97].

Lift-off sometimes did not work well after this process. Hot acetone and using an ultrasonic bath helps.

**Hearsay:** Cooling the sample with liquid nitrogen during the evaporation helps avoiding leakage-currents between gate and 2DES. A leakage current between gates and 2DES was not observed in any sample.

**Process:**

1. *Clean.*
2. *Coat with photoresist.*
3. *Expose* photoresist for 25 s with the ‘gate’ mask (Figure 69(c)).
4. *Create undercut.*
5. *Develop photoresist.*
6. *Deposit metalization* in Varian VT118 UHV-evaporator with e-beam evaporation unit:
  - (a) Put the sample in the transfer chamber, pump the transfer chamber overnight,
  - (b) evaporate from the NiCr and the Au source for 3 min each,
  - (c) pump for 1 h, transfer the sample into the main chamber;
  - (d) heat up the NiCr source,
  - (e) cool the sample for 2 min with liquid nitrogen through the transfer tube and continue cooling during the whole evaporation;
  - (f) open the shutter, evaporate 20 nm NiCr at a rate of  $\approx 0.5$  nm/s as adhesion layer,
  - (g) evaporate 100 nm Au at a rate of  $\approx 1$  nm/s,
  - (h) turn off the liquid nitrogen and let the sample warm up for 2 h before removing sample from system.
7. *Lift-off*, use ultrasound if necessary.

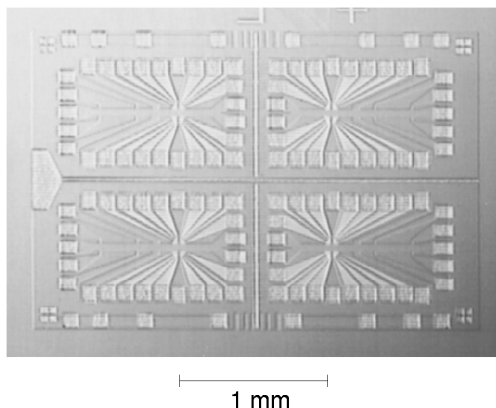


Figure 71: Chip p11.8 after the processes defined by optical lithography.

## D.6 Electron-beam lithography

In this step, the gate structure defining the SET is created. The gate fingers used have a center to center distance of only  $100\text{ nm}$  as shown in Figure 74(b). Many of the problems mentioned are due to limitations of our e-beam writing system consisting of a Hitachi SEM and an Elphy III deflection unit.

**Problems with the e-beam system:** Adjusting to the leads deposited via optical lithography had to be better than  $1.5\ \mu\text{m}$ , as can be seen in Figure 72(a). By continuously exposing the alignment windows (see Figure 72(a)), the gate metalization becomes visible on the SEM screen, allowing a mechanical adjustment better than  $1\ \mu\text{m}$ .

The resolution is not good enough in the large write fields that are needed to reach the optically predefined gate leads. Therefore, the SET-pattern is exposed in a smaller write field.

The center of the two write fields is different and the write field sizes deviate from their nominal values due to imperfections in the amplifiers of the SEM. Therefore, process step 3c became necessary. In addition to this, the position drifts; letting the hardware warm up for half an hour and working quickly results in good alignment of the write fields, as in Figure 74(a).

**Problems with the resulting gate structures:** Some gates showed hysteretic behavior, some had no effect at all. Test strips were added to each sample to be able to check each metalization.

NiCr, as only component of the metalization, was not to be conducting well. Thin layers (12 nm) that were conducting at room temperature showed diminishing conductance at lower temperatures. Thicker layers (24 nm) had cracks visible under an SEM. As a result, a layer of gold was added to the metalization and the lithography adapted to the thicker metalization.

The Hall-bar edges are candidates for weak links in the metalization. Therefore, the thicker metalization for the gate contacts extends onto the Hall-bar.

The gate contacts are thick compared to the metalization for the e-beam structure. The geometry and evaporation angle were chosen, as explained in Figure 73, to avoid discontinuities due to shadowing.

A number of other defects such as broken cryostat wiring, broken bonds and damage by electrostatic discharge can also cause similar symptoms.

### Process:

1. *Clean.*
2. Spin-coat sample with e-beam resist (PMMA):
  - (a) Use spin-coater 1001S /St146 (Convac),
  - (b) center sample on platter, blow dry with nitrogen,
  - (c) apply three drops of PMMA (E-Beam Resist PMMA 950K [AR-P 671 from Allresist GmbH] thinned to 2.5% solid contents with chlorobenzene as solvent);
  - (d) spin at 3000 1/min for 5 s and apply another 3 drops of PMMA,
  - (e) continue spinning at 8000 1/min for 30 s;
  - (f) bake for 1.5 h at 160 °C in an oven,
  - (g) measure the thickness of the resist (168 nm for p11.5):
    - i. Make scratches into PMMA in the homogeneous central area,
    - ii. measure depth with contact probe (Dektak 3030 from Sloan Technology Corporation).
3. Expose PMMA using a Hitachi S-2000 SEM with the deflection controlled via an ELPHY III system (Raith GmbH):

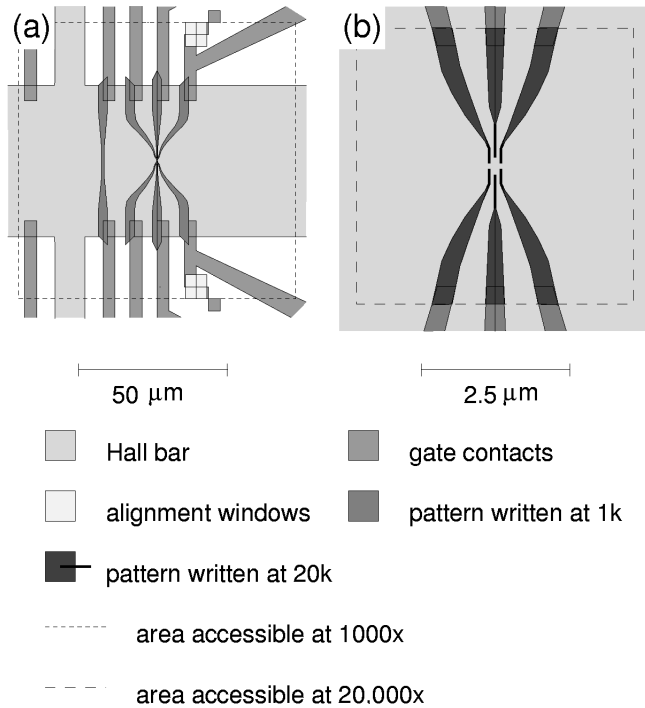


Figure 72: Structure layout for e-beam lithography. (a) Alignment of e-beam structure to predefined optical lithography. (b) Nanostructure relevant for the experiments. The distance between the inner lines defining the split gates is 100 nm.

- (a) Adjust beam current to  $\approx 15$  pA,
  - (b) focus and correct astigmatism,
  - (c) correct mismatch between write fields at different magnifications:
    - i. Expose four spots for 1 min at 1000 magnification to generate visible contamination and
    - ii. read the positions of these spots at 20 000 magnification to determine the necessary corrections.
4. After this preparation, perform the following steps for each chip-section:
- (a) Adjust the focus at a spot close to the writing position;
  - (b) align to the gate leads of the first SET,
  - (c) write SET “a” and test strip:
    - i. Expose the light grey areas in Figure 72 at 1000x magnification with a dose of  $300 \mu\text{C}/\text{cm}^2$ ,
    - ii. expose dark grey areas in Figure 72 at 20,000x magnification with a dose of  $300 \mu\text{C}/\text{cm}^2$  and
    - iii. expose the lines in Figure 72(b) at 20,000x magnification with 1 nm point spacing and  $10 \mu\text{s}$  dwell time per point.
  - (d) Align to gate leads of the second SET and
  - (e) write SET “b”.
5. Develop PMMA.
- (a) Mix isobutyl methyl ketone : propanol in the ratio 1:3;
  - (b) develop for 80 s in this mixture (the development time depends on the thickness  $d$  of the PMMA:  $30 \text{ s} + 30 \text{ s} \times d/100 \text{ nm}$ ), shaking continuously;
  - (c) stop development by putting sample for 60 s in propanol,
  - (d) blow dry with nitrogen.
6. *Evaporate metal:*
- (a) Use an angle of  $5^\circ$  as depicted in Figure 73(b),

- (b) evaporate 5 nm NiCr (adhesion to GaAs is sufficient, to PMMA it is not. 10 nm NiCr give good adhesion on PMMA also) and
- (c) evaporate 20 nm Au.

7. *Lift-off*, use hot acetone (65 °C) and ultrasonic bath if necessary.

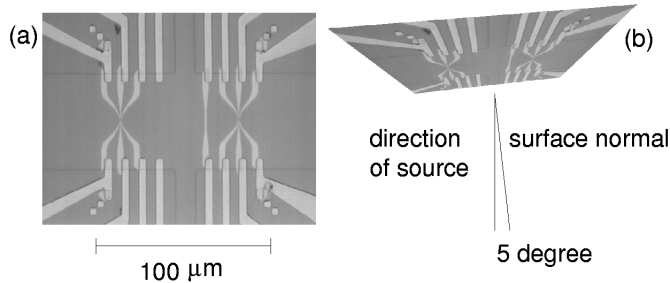


Figure 73: Pattern defined by electron-beam lithography and alignment to the structures defined by optical lithography. (a) The electron-beam pattern overlaps all the optically defined leads to one side and (b) the evaporation is carried out at a small angle to avoid discontinuities caused by shadowing.

## D.7 Splitting and mounting

The chips are split into four pieces and glued into chip carriers using PMMA or epoxy glue (see Figure 75). The pads are then wire bonded to the carrier using 17.5 μm gold wire. The problem of electrostatic discharge is an experimental detail, but it can be hard to find out in which step it occurs; I, therefore, want to mention what worked for me.

**Problem:** The structures are susceptible to electrostatic discharge which can lead to a destruction of the gate metalization as seen in Figure 76. Depending on the cryostat two different paths were taken:

### TLM-400 system (without socket for the chip carrier)

1. Solder leads with connectors to the contacts of the chip carrier;
2. ground all of the contacts during bonding and mounting;

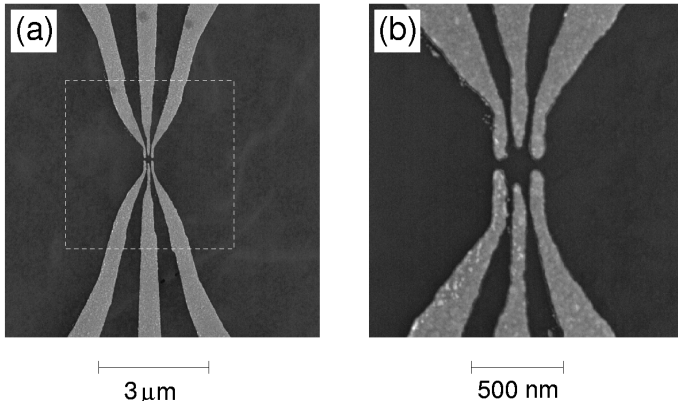


Figure 74: SEM pictures of the split gates that define the quantum dot. Light areas correspond to the metalization (a) dashed line delimits the area written at higher resolution (b) the open area in the center between the gates has a diameter of approximately  $180\ \text{nm}$ .

3. use an anti-static wrist strap and non-conducting tweezers; keep lines on top of transfer-tube grounded until the sample is cold.

### **Kelvinox system (with socket for the chip carrier)**

1. Isolate all contacts during bonding except the back-gate contact;
2. connect back-gate contact to ground;
3. as first bond, connect the back-gate contact to the substrate (at room temperature and under illumination the substrate is conducting; this reduces the likelihood of damage);
4. plug the sample into the socket using non-conducting tweezers wearing an anti-static wrist strap. Keep lines on top of transfer-tube grounded until the sample is cold.

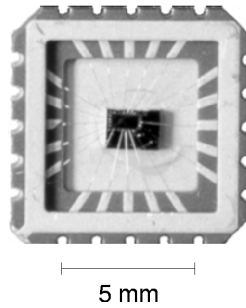


Figure 75: Sample glued and bonded into a chip-carrier.

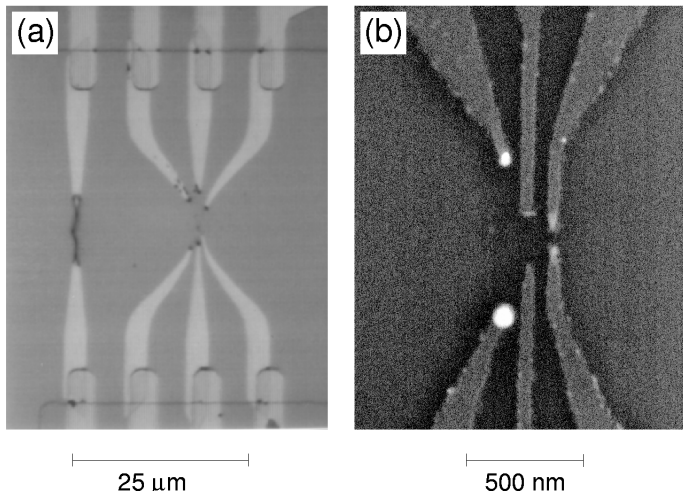


Figure 76: Samples destroyed by electrostatic discharge. (a) Severe damage of p11.5.4o caused by careless handling while taking the pictures in this section. (b) More subtle damage of p5.2.2b (note that the scales are different). There is noticeable damage by electrostatic discharge close to the Hall bar edge in (a) indicating that there are still weak links.

## E Measurement setup

### E.1 Instrumentation

The experiments described in this work were done in two different dilution refrigerators, both from Oxford instruments, and using two different measurement-setups. In this section the measurement setups are depicted and the errors are discussed. The details found in this chapter are not interesting from the physical point of view, but the practical information may be helpful in reproducing the experiments.

#### E.1.1 TLM400

The measurements presented in Chapter 2 were done in the TLM400 with the setup in Figure 77 at a base temperature of approximately 30 mK.

The voltage  $V_D$  applied to the drain contact of the sample consists of a DC and a small AC component  $V_D(t) = \overline{V_D} + \Delta V_D \cos(2\pi ft)$ . An “Ithaco 1211” current to voltage converter (I-V converter) is used to keep the point  $V_S$  at virtual ground and to measure the current into this point. The DC component  $I$  is obtained from dividing the readout of a Keithley digital multimeter attached to the I-V converter by the conversion factor. The AC component  $\Delta I$  is measured indirectly via an EG&G PRINCETON APPLIED RESEARCH Model 5210 lock-in amplifier. The quantities of interest are the voltage across the quantum dot  $V_{DS} \approx V_D - V_S$  and the differential conductance  $dI/dV_{DS} \approx \Delta I/\Delta V_D$ .

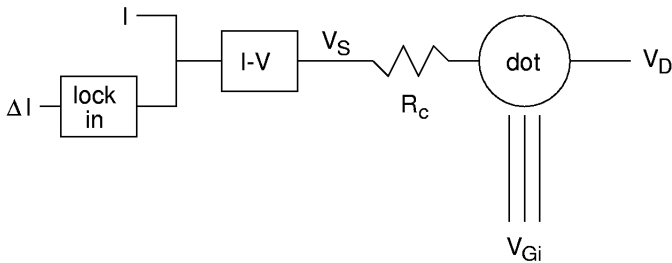


Figure 77: Schematic representation of the measurement setup. “I-V” stands for an Ithaco 1211 current-to-voltage converter.  $V_{Gi}$  stands for the different gate voltages,  $V_D$  for the drain voltage and  $R_c$  for cable and contact resistances in series with the dot.

The relevant errors in these measurements were the following:

- There is a contact “resistance”  $R_c$  due to the wiring and the ohmic contacts of the sample. In the experiments the series p8\* had non ohmic contacts with a maximum resistance of  $20\text{ k}\Omega$  at low drain voltages and low ( $< 0.2\text{ T}$ ) magnetic fields. This leads to the following errors:
  - $V_{\text{DS}}$  deviates from the voltage across the dot.
  - The measurement of the differential conductance is inaccurate, especially for low  $V_{\text{DS}}$ .
- The gate voltages  $V_{\text{G}i}$  drift by up to  $\pm 150\text{ }\mu\text{V}$  due to changes in the room temperature.
- The current to voltage converter introduces an offset in  $V_{\text{DS}}$  which drifts by  $\approx 5\text{ }\mu\text{V}$  and has an average value on the order of one hundred  $\mu\text{V}$ . This average value was subtracted.
- A DC bias of  $\approx \pm 3\text{ }\mu\text{V}$  was needed to obtain a unique current direction due to high frequency noise [98]. This information is used as a measure of the quality of the RF shielding.
- In the lock-in measurements, a signal of  $\approx 4\text{ }\mu\text{V}_{\text{RMS}}$  at a frequency of  $f \approx 13\text{ Hz}$  and an integration time of  $1\text{ s}$  was used.

### E.1.2 Kelvinox 400

The later measurements (all data in Chapters 5 and 6 except Figures 38 and 38) were done in a kelvinox 400 system. A base temperature of  $12\text{ mK}$  was reached in this system. The measurement setup was modified to allow for accurate measurements of the differential conductance even in the presence of contact resistances by adding a second lock-in amplifier to measure  $\Delta V_{\text{DS}}$ . Due to improved ohmic contacts,  $R_C$  was truly ohmic and significantly smaller than before with a value of  $\approx 2\text{ k}\Omega$ . In addition to this, the RF noise was shielded better and the stability of the gate voltage sources was improved. In this system a probe with a rotatable sample holder was available for measurements in tilted magnetic fields. This setup had the following characteristics:

- drift in the gate voltages below  $50\text{ }\mu\text{V}$ ,
- the bias needed to obtain a unique current direction was below  $\pm 0.75\text{ }\mu\text{V}$ ,

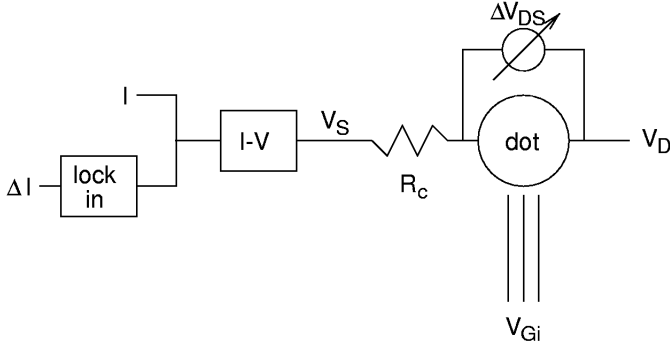


Figure 78: Setup for the Kelvinox system. A second lock-in amplifier was added to measure  $\Delta V_{DS}$ .

- the error in  $V_{DS}$  is smaller due to a smaller  $R_C$ ,
- the systematic error in the differential conductance is negligible,
- In the lock-in measurements a signal of  $\approx 1 \mu V_{RMS}$  at a frequency of  $f \approx 37$  Hz and an integration time of 1 s was used.

## E.2 Low temperature measurements

Temperature is a quantity which is only well defined in equilibrium systems. Our sample is connected to room temperature equipment with metal wires, and thermal and other noise can disturb the measurement. To make the situation worse, at milli Kelvin temperatures thermal conduction between the wires and the  $\text{He}^3/\text{He}^4$  mixture drops sharply due to the Kapitza effect.

### E.2.1 Thermal noise

Thermal voltage noise (Johnson noise) is necessarily present in wires or electronics with a finite resistance  $R$

$$V_{\text{noise, RMS}} = \sqrt{4k_B T R f_B},$$

where  $f_B$  is the bandwidth or cutoff frequency [99]. For a  $10 \text{ k}\Omega$  resistor at room temperature and a bandwidth of  $100 \text{ kHz}$ , this already leads to a noise voltage of  $4 \mu V$ . When applying voltages to the sample it is, therefore, necessary to avoid high resistances at room temperature and to limit the

bandwidth. Limiting the bandwidth of the electrical lines going to the sample is also essential for a less fundamental reason, namely RF interference.

### E.2.2 RF-interference

RF-interference turned out to be the major obstacle in achieving undisturbed measurements at low temperatures. The primary source found with a spectrum analyzer were radio stations. Computers made visible but smaller contributions. An interference in the range of a few mV was commonly observed even when using shielded cables (due to imperfect shielding of the instruments). Limiting the band-width to suppress the high frequency range was used successfully to reach low noise levels in the experiments. Figures 79 and 80 depict the high frequency roll off of three filters used in the experiments. These descriptions correspond to our best results obtained in the Kelvinox setup, the part numbers of the components used are included to ease reproduction.

The  $\pi$ -feed-through filter (Tusonix part Nr. 4700-056) gives a good suppression of high frequencies (Figure 79(c)), but is not suitable for low temperatures or high magnetic fields (it contains a ferrite bead). It is essential to carefully solder the filter into a ground-plane to avoid crosstalk as can be seen from Figure 79(b) which at DC corresponds to the same circuit as Figure 79(c). This filter was used on every line going into the probe head.

Some types of ceramic capacitors can be used at low temperatures, others fail. In our experience capacitors with an NP0 dielectric work. The three terminal SMD (surface mount device) capacitors from AVX (Part No. W3FIIA4718AT, 470 pF) were used at the location of the 1-k pot in the cryostat and close to the sample on all lines. The suppression is shown in Figure 80. Even when carefully soldering these capacitors into a ground plane we end up with a pole in the several 100 MHz range above which noise is transmitted.

We therefore also used a so-called strip-line (see for example [100]), a distributed resistive and capacitive component. It was made of  $\approx 25$  cm coated manganin wire with  $50 \mu\text{m}$  diameter covered by a layer of conductive silver paint that was connected to ground. This strip-line (Figure 80(c)) was operated at the base temperature of the cryostat close to the sample, since the resistance necessary for the damping would be a noise source of its own at higher temperatures.

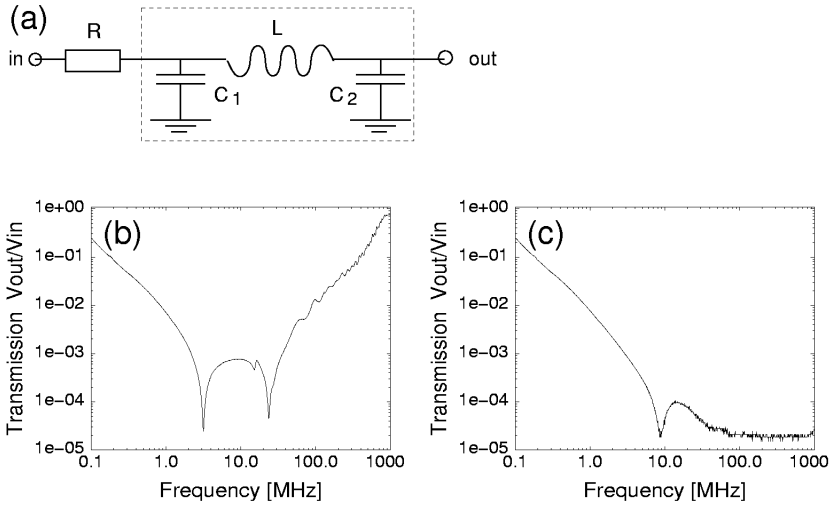


Figure 79: Transmission through a tucsonix  $\pi$ -filter. (a) A series resistance of  $R = 50\ \Omega$  was used in the measurement. The  $\pi$ -filter is symbolized by the dotted area and specified as  $C_1 = C_2 = 5\ \text{nF}$ . (b) Filter contacted by wires. (c) Filter soldered into a ground plane.

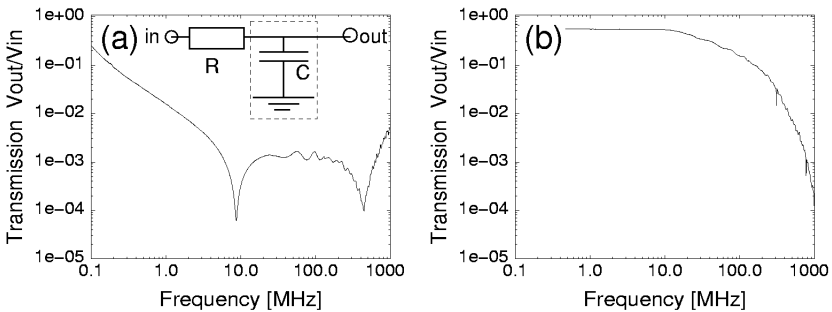


Figure 80: (a) Transmission through a  $470\ \text{pF}$  SMD capacitor with a  $R = 50\ \Omega$  resistor in series. (b) Transmission through a strip line.

## F Symbols and notations

In this chapter, the terms and abbreviations used throughout the thesis are defined. In addition to this, the values of material parameters and of physical constants are given.

### F.1 Conventions

Energy	is measured in eV or meV instead of J as the “natural” unit of energy for single electrons.
Conductance	is measured in units of $e^2/h$ .
Vectors	are boldface, the corresponding normal symbol represents the absolute value of the quantity.
Reservoir	denotes a large electron system. The term implies that excitations are swallowed without changing the state of the reservoir in a way that a small system coupled to the reservoir could notice.
Lead	denotes a physical system; it can come close to being a reservoir.
Transparency	is a property of a tunnel-barrier in a single-particle picture and measured in 1/s.
Tunnel-coupling	is the energy corresponding to the transparency.
Tunnel-rate	denotes a quantity derived in the single-electron approximation as the product of transparency and distribution functions.
Addition spectrum	denotes the discrete energies for adding electrons to the dot but does not contain information about their weights.
Spectral density	is defined in Chapter 4.

$pa.b.cx$  is the name of a sample,  $a$  denotes the batch,  $b$  the sample within a batch,  $c \in \{1..4\}$  the chip section,  $x \in \{i, o\}$  the inner or outer quantum dot.

## F.2 Abbreviations

2DES	two-dimensional electron system
SET	single-electron transistor
CB	Coulomb blockade
QPC	quantum point contact
DI-water	de-ionized water
RF	radio frequency
SEM	scanning electron microscope
MBE	molecular beam epitaxy
UHV	ultra-high vacuum
PMMA	polymethylmetacrylat
STM	scanning tunneling microscope
SQUID	superconducting quantum interference device
$f_F(x) = 1/(1 + \exp(x))$	Fermi function

## F.3 Physical constants

$c = 2.997925 \times 10^8 \text{ m} \cdot \text{s}^{-1}$	speed of light
$e = 1.6021917 \times 10^{-19} \text{ C}$	elementary charge
$-e$	charge of an electron
$h = 6.626196 \times 10^{-34} \text{ J} \cdot \text{s}$ ,	Planck constant
$\hbar = h/2\pi = 1.054592 \times 10^{-34} \text{ J} \cdot \text{s}$	

$k_B = 1.3806 \times 10^{-23} \text{ J} \cdot \text{K}^{-1}$  Boltzmann constant

$m_e = 9.109558 \times 10^{-31} \text{ kg}$  mass of an electron

$\mu_B = eh/(4\pi m_e)$  Bohr magneton

$$= 9.274096 \times 10^{-24} \text{ J} \cdot \text{T}^{-1}$$

$\Phi_0 = e/h = 2.41797 \text{ T}^{-1} \cdot \text{m}^{-2}$  flux quantum

$e^2/h = 0.3874045 \times 10^{-6} \Omega^{-1}$  conductance quantum

$R_K = 25\,812.807 \Omega$  Klitzing constant, the value given is  $R_{K-90}$

## F.4 Material parameters of the two-dimensional electron system (2DES)

The values given in parentheses are specific for substrate No. 8363 (see Figure 67).

$d_{2\text{DES}}$  depth of the 2DES below the surface ( $d_{2\text{DES}} = 50 \text{ nm}$ )

$n_{2\text{DES}}$  electron density of the 2DES ( $n_{2\text{DES}} = 3.2 \times 10^{15} \text{ m}^{-2}$ )

$\mu_{2\text{DES}}$  electron mobility of the 2DES at 4.2 K ( $\mu_{2\text{DES}} = 30 \text{ V} \cdot \text{s} \cdot \text{m}^{-2}$ )

$m_{e,\text{GaAs}} = 0.067m_e$  effective mass of electrons in GaAs

$g_{\text{GaAs}} = -0.44$  Landé  $g$ -factor of electrons in bulk GaAs  
( $\mu_B g_{\text{GaAs}} = -25.5 \times 10^{-6} \text{ eV} \cdot \text{T}^{-1}$ )

$\epsilon_{\text{GaAs}} = 13.17$  relative dielectric constant of GaAs at room temperature [101], values as different as 12.85 have been suggested [102]

### F.4.1 Derived material parameters

$\nu_{2DES} = en_{2DES}/(hB_{\perp})$	Landau-level filling factor or number of electrons per magnetic flux quantum
$\varepsilon_F = \pi\hbar^2 n_{2DES}/(2m_{e,\text{GaAs}})$	Fermi energy ( $\varepsilon_F = 5.7 \times 10^{-3}$ eV)
$\lambda_F = \sqrt{8\pi/n_{2DES}}$	wavelength of the electrons at the Fermi energy of the 2DES ( $\lambda_F = 89 \times 10^{-9}$ m)
$v_F = h/\lambda_F$	Fermi velocity ( $v_F = 1.23 \times 10^5$ m/s)
$D = 2m_{e,\text{GaAs}}/(\pi\hbar^2)$	Density of states for twofold spin degeneracy in two dimensions ( $D = 2.8 \times 10^{17}$ eV $^{-1}$ ·m $^{-2}$ )
$\omega_c = eB_{\perp}/m_{e,\text{GaAs}}$	cyclotron frequency in GaAs ( $\hbar\omega_c/B_{\perp} = 1.7 \times 10^{-3}$ eV·T $^{-1}$ )
$\lambda_c = \sqrt{\hbar/(eB_{\perp})}$	magnetic length (radius of cyclotron orbit) ( $\lambda_c = 25.656 \times 10^{-9}$ m·T $^{1/2}$ )

## F.5 Voltages applied to the sample

The voltages  $V_i$  applied to the 2DES and the gate electrodes via the cryostat wiring are depicted schematically in Figure 81. These voltages determine the electro-chemical potentials  $\mu_i$  and electrical potentials  $\varphi_i$  at the position of the SET.

$V_D$	drain voltage
$V_S$	source voltage usually set to 0
$V_{LU}$	gate voltage applied to upper left gate
$V_{LL}$	gate voltage applied to lower left gate
$V_{MU}$	gate voltage applied to upper middle gate
$V_{ML}$	gate voltage applied to lower middle gate
$V_{RU}$	gate voltage applied to upper right gate
$V_{RL}$	gate voltage applied to lower right gate

$V_{BG}$  voltage applied to the metalized chip carrier at the back side of the sample substrate

$V_G$  gate voltage, can stand for any of the above except  $V_S$  or  $V_D$

Those voltages are combined to :

$V_{DS} \equiv V_D - V_S$  drain-source voltage, also called transport voltage

$V_L \equiv V_{LU} = V_{LL}$  gate voltage applied to both left gates

$V_M \equiv V_{MU} = V_{ML}$  gate voltage applied to both middle gates

$V_R \equiv V_{RU} = V_{RL}$  gate voltage applied to both right gates

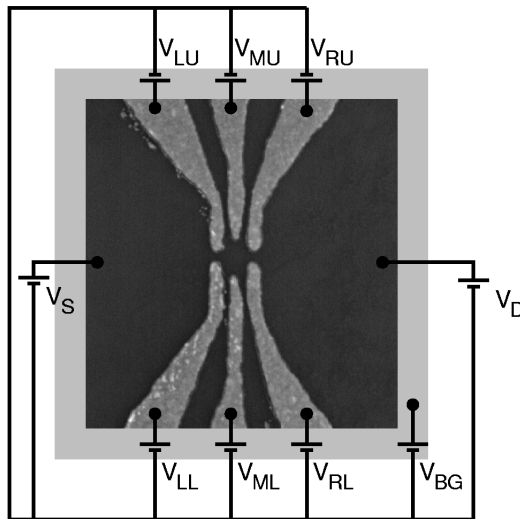


Figure 81: Names assigned to the voltages applied to the sample. The shaded area represents a gold-surface at the back of the sample.

## F.6 Observables

$I$  current through the quantum dot

$dI/dV_{DS}$  differential conductance

## F.7 Other experimental parameters

$T$	temperature of the sample
$\mathbf{B}$	magnetic field
$B$	absolute value of the magnetic field
$B_{\parallel}$	component of the magnetic field in the plane of the 2DES
$B_{\perp}$	component of the magnetic field orthogonal to the plane of the 2DES

## F.8 Characteristics of a quantum dot

$N$	number of electrons on the dot
$E_{N,I}$	energy for $N$ electrons on the dot in state $I$
$\mu_{N,I,F} \equiv E_{N,F} - E_{N-1,I}$	energy for adding the $N^{th}$ electron to an isolated dot, initial state $I$ (of the $N-1$ electron system), final state $F$ (of the $N$ electron system)
$\Gamma_{r,N,I,F}$	transparency of barrier $r$ for the above mentioned transition (the index $r \in \{D, S\}$ stands for the drain and source barriers),
$\Gamma_r$	if no transition is specified, <i>equal</i> transparencies for the transitions studied are assumed
$\Gamma = \Gamma_D + \Gamma_S$	<i>sum</i> of the transparencies of both barriers, $\hbar\Gamma$ is also called intrinsic linewidth
$\mu_N \equiv \mu_{N,0,0}$	energy for adding the $N^{th}$ electron to the dot beginning in the $N-1$ -electron ground-state and ending in the $N$ -electron ground-state
$E_{G,N} \equiv \mu_N - \mu_{N-1}$	gap between adding the $N-1^{st}$ and the $N^{th}$ electron
$= E_N + E_{N-2} - 2E_{N-1}$	

$C_\Sigma$	total capacitance of the dot
$\Delta\mu_{N,F} = \mu_{N,I,F} - \mu_{N,I,0}$	excitation energies of the $N$ -electron system
$\varepsilon_{ks}$	single-particle energies for a given confinement potential
$T_K$	Kondo temperature

The following derivatives are named:

$\alpha_{i,N,I} = \partial E_{N,I} / \partial \varphi_i$	coupling between dot and electrode $i$
$c_{iN,I} = (1/eN) \cdot \partial E_{N,I} / \partial \varphi_i$	normalized coupling
$C_G = C_\Sigma \times c_G$	“capacitance” between dot and electrode $i$

## References

- [1] G. J. D. T. A. Fulton, Phys. Rev. Lett. **59**, 109 (1987).
- [2] J. M. Hergenrother, M. T. Tuominen, and M. Tinkham, Phys. Rev. Lett. **72**, 1742 (1994).
- [3] M. Bockrath, D. H. Cobden, P. L. McEuen, N. G. Chopra, A. Zettl, A. Thess, and R. E. Smally, Science **275**, 1922 (1997).
- [4] J. H. F. Scott-Thomas, S. B. Field, M. A. Kastner, H. I. Smith, and D. A. Antoniadis, Phys. Rev. Lett. **62**, 583 (1989).
- [5] H. V. Houten and C. W. J. Beenakker, Phys. Rev. Lett. **10**, 1893 (1989).
- [6] L. I. Glazman and R. I. Shekhter, J. Phys.: Condens. Matter **1**, 5811 (1989).
- [7] P. L. McEuen, E. B. Foxman, U. Meirav, M. A. Kastner, Y. Meir, N. S. Wingreen, and S. J. Wind, Phys. Rev. Lett. **66**, 1926 (1991).
- [8] U. Meirav, M. A. Kastner, and S. J. Wind, Phys. Rev. Lett. **65**, 771 (1990).
- [9] J. Weis, Ph.D. thesis, Universität Stuttgart, 1994.
- [10] H. Pothier, J. Weis, R. J. Haug, and K. v. Klitzing, Appl. Phys. Lett. **62**, 3174 (1993).
- [11] S. Tarucha, D. G. Austing, T. Honda, R. J. van der Hage, and L. P. Kouwenhoven, Phys. Rev. Lett. **77**, 3613 (1996).
- [12] L. P. Kouwenhoven, T. H. Oosterkamp, M. W. S. Danoesastro, M. Eto, D. G. Austing, T. Honda, and S. Tarucha, Science **278**, 1788 (1997).
- [13] T. H. Oosterkamp, J. W. Janssen, L. P. Kouwenhoven, D. G. Austing, T. Honda, and S. Tarucha, Phys. Rev. Lett. **82**, 2931 (1999).
- [14] L. J. Geerligs, V. F. Anderegg, P. A. M. Holweg, J. E. Mooij, H. Pothier, D. Esteve, C. Urbina, and M. H. Devoret, Phys. Rev. Lett. **64**, 2691 (1990).

- [15] L. P. Kouwenhoven, A. T. Johnson, N. C. van der Vaart, C. J. P. M. Harmans, and C. T. Foxon, *Phys. Rev. Lett.* **67**, 1626 (1991).
- [16] H. Pothier, P. Lafarge, C. Urbina, D. Esteve, and M. H. Devoret, *Europhysics Letters* **17**, 249 (1992).
- [17] J. M. Martinis, M. Nahum, and H. D. Jensen, *Phys. Rev. Lett.* **72**, 904 (1994).
- [18] P. Lafarge, H. Pothier, E. R. Williams, D. Esteve, C. Urbina, and M. H. Devoret, *Z. Phys. B* **85**, 327 (1991).
- [19] M. J. Yoo, T. A. Fulton, H. F. Hess, R. L. Willett, L. N. Dunkleberger, R. J. Chichester, L. N. Pfeiffer, and K. W. West, *Science* **276**, 579 (1997).
- [20] Y. Y. Wei, J. Weis, K. v. Klitzing, and K. Eberl, *Appl. Phys. Lett.* **71**, 2514 (1997).
- [21] Y. Y. Wei, J. Weis, K. v. Klitzing, and K. Eberl, *Phys. Rev. Lett* **81**, 1674 (1998).
- [22] P. W. Anderson, *Phys. Rev.* **124**, 41 (1961).
- [23] I. Giaever and H. R. Zeller, *Phys. Rev. Lett* **20**, 1504 (1968).
- [24] J. B. Barnes and S. T. Ruggiero, *Phys. Rev. Lett.* **59**, 807 (1987).
- [25] D. V. Averin and K. K. Likharev, *Journal of Low Temperature Physics* **62**, 345 (1986).
- [26] M. H. Devoret, D. Esteve, H. Grabert, G. L. Ingold, H. Pothier, and C. Urbina, *Phys. Rev. Lett.* **64**, 1824 (1990).
- [27] S. M. Girvin, L. I. Glazman, M. Jonson, D. R. Penn, and M. D. Stiles, *Phys. Rev. Lett.* **64**, 3183 (1990).
- [28] U. Meirav and E. B. Foxman, *Semicond. Sci. Technol.* **10**, (1995).
- [29] D. Davidović and M. Tinkham, *Appl. Phys. Lett.* **73**, 3959 (1998).
- [30] D. L. Klein, R. Roth, A. K. L. Lim, A. P. Alivisatos, and P. L. McEuen, *Nature* **389**, 699 (1997).

- [31] A. Thornton, I. Itskevich, T. Ihn, M. Henini, P. Moriarty, A. Nogaret, P. H. Benton, L. Eaves, P. C. Main, J. R. Middleton, and M. Heath, *Superlattices and Microstructures* **21**, 255 (1997).
- [32] R. Dingle, H. L. Störmer, A. C. Gossard, and W. Wiegmann, *Appl. Phys. Lett.* **33**, 665 (1978).
- [33] H. L. Störmer, R. Dingle, A. C. Gossard, W. Wiegmann, and M. D. Sturge, *Solid State Comm.* **29**, 705 (1979).
- [34] B. J. van Wees, H. van Houten, C. W. J. Beenakker, J. G. Williamson, L. P. Kouwenhoven, D. van der Marcel, and C. T. Foxon, *Phys. Rev. Lett.* **60**, 848 (1988).
- [35] K. v. Klitzing, G. Dorda, and M. Pepper, *Phys. Rev. Lett.* **45**, 494 (1980).
- [36] H. L. Störmer, D. C. Tsui, A. C. Gossard, and J. C. M. Hwang, *Physica B* **117**, 688 (1983).
- [37] C. W. J. Beenakker, *Phys. Rev. B* **44**, 1646 (1991).
- [38] M. H. Devoret and H. Grabert, in *Single Charge Tunneling Coulomb blockade Phenomena in Nanostructures*, edited by H. Grabert and M. H. Devoret (Plenum Press, New York and London, 1992), pp. 1–18, nATO ASI Series B Physics Vol. 294.
- [39] L. P. Kouwenhoven, C. M. Marcus, P. L. McEuen, S. Tarucha, R. M. Westervelt, and N. S. Wingreen, in *Mesoscopic Electron Transport*, edited by L. L. S. et al. (Kluwer Academic Publishers, the Netherlands, 1997), pp. 105–214.
- [40] E. B. Foxman, P. L. McEuen, U. Meirav, N. S. Wingreen, Y. Meir, P. A. Belk, N. R. Belk, M. A. Kastner, and S. J. Wind, *Phys. Rev. B* **47**, 10020 (1993).
- [41] J. Weis, R. J. Haug, K. v. Klitzing, and K. Ploog, *Phys. Rev. Lett.* **71**, 4019 (1993).
- [42] D. Esteve, in *Single Charge Tunneling Coulomb blockade Phenomena in Nanostructures*, edited by H. Grabert and M. H. Devoret (Plenum Press, New York and London, 1992), pp. 109–137, nATO ASI Series B Physics Vol. 294.

- [43] A. Furusaki and K. A. Matveev, *Phys. rev. B* **52**, 16676 (1995).
- [44] J. Schmid, Ph.D. thesis, Institut für Theoretische Festkörperphysik, Universität Karlsruhe, 1996.
- [45] D. Goldhaber-Gordon, H. Shtrikman, D. Mahalu, D. Abusch-Magder, U. Meirav, and M. A. Kastner, *Nature* **391**, 156 (1998).
- [46] L. I. Glazman and M. E. Raïkh, *Pis'ma Zh. Eksp. Teor. Fiz.* **47**, 378 (1988).
- [47] T. K. Ng and P. A. Lee, *Phys. Rev. Lett.* **61**, 1768 (1988).
- [48] S. M. Cronenwett, T. H. Oosterkamp, and L. P. Kouwenhoven, *Science* **281**, 540 (1998).
- [49] F. Simmel, R. H. Blick, J. P. Kotthaus, W. Wegscheider, and M. Bichler, *Phys. Rev. Lett.* **83**, 804 (1999).
- [50] J. Göres, D. Goldhaber-Gordon, S. Heemeyer, M. A. Kastner, H. Shtrikman, D. Mahalu, and U. Meirav, to be published (2000).
- [51] W. J. de Haas, J. de Boer, and G. J. van den Berg, *Physica* **1**, 1115 (1933).
- [52] G. J. van den Berg and J. de Nobel, *Le journal de physique et le radium* **23**, 665 (1962).
- [53] J. Kondo, *Progress of Theoretical Physics* **32**, 37 (1964).
- [54] J. R. Schrieffer and P. A. Wolff, *Physical Review* **149**, 491 (1966).
- [55] J. A. Appelbaum and L. L. Shen, *Phys. Rev. B* **5**, 544 (1972).
- [56] E. L. Wolf and D. L. Losee, *Phys. Rev. B* **2**, 3660 (1970).
- [57] D. C. Ralph and R. A. Buhrman, *Phys. Rev. Lett.* **72**, 3401 (1994).
- [58] J. Schmid, J. Weis, K. Eberl, and K. von Klitzing, *Physica B* **256-258**, 182 (1998).
- [59] V. Madhavan, W. Chen, T. Jamneala, M. F. Crommie, and N. S. Wingreen, *Science* **280**, 567 (1998).

- [60] N. Andrei, G. T. Zimányi, and G. Schön, *Phys. Rev. B* **60**, R5125 (1999).
- [61] U. Wilhelm, J. Schmid, J. Weis, and K. v. Klitzing, to be published (2000).
- [62] U. Wilhelm, Ph.D. thesis, Max-Planck-Institut für Festkörperforschung Stuttgart, 2000.
- [63] D. C. Langreth, *Phys. Rev.* **150**, 516 (1966).
- [64] A. Kawabata, *Journal of The Physical Society of Japan Letters* **60**, 3222 (1991).
- [65] T. A. Costi, A. C. Hewson, and V. Zlatić, *J. Phys.: Condens Matter* **6**, 2519 (1994).
- [66] J. Schmid, J. König, H. Schoeller, and G. Schön, *Physica E* **1**, 241 (1997).
- [67] Y. Meir, N. S. Wingreen, and P. A. Lee, *Phys. Rev. Lett.* **70**, 2601 (1993), *gut*.
- [68] J. König, J. Schmid, H. Schoeller, and G. Schön, *Phys. Rev. B* **54**, 16820 (1996).
- [69] N. S. Wingreen and Y. Meir, *Phys. Rev. B* **49**, 11040 (1994).
- [70] J. König, H. Schoeller, and G. Schön, *Europhysics Letters* **31**, 31 (1995).
- [71] F. D. M. Haldane, *Phys. Rev. Lett.* **40**, 416 (1978).
- [72] J. König, H. Schoeller, and G. Schön, *Phys. Rev. Lett.* **76**, 1715 (1996).
- [73] D. Goldhaber-Gordon, J. Göres, M. A. Kastner, H. Shtrikman, D. Mahalu, and U. Meirav, *Phys. Rev. Lett.* **81**, 5225 (1998).
- [74] D. R. Hamann, *Phys. Rev.* **158**, 570 (1967).
- [75] P. Nozieres, *J. Low Temp. Phys.* **17**, 31 (1974).
- [76] H. R. Krishna-murthy, J. W. Wilkins, and K. G. Wilson, *Phys. Rev. B* **21**, 1003 (1980).

- [77] H. R. Krishna-murthy, J. W. Wilkins, and K. G. Wilson, *Phys. Rev. B* **21**, 1044 (1980).
- [78] N. S. Wingreen, *Phys. Rev. B* **49**, 11040 (1994).
- [79] T. Inoshita, A. Shimizu, Y. Kuramoto, and H. Sakaki, *Phys. Rev. B* **48**, 14725 (1993).
- [80] T. Inoshita, Y. Kuramatu, and H. Sakaki, *Superlattices and Microstructures* **22**, 75 (1997).
- [81] T. Pohjola, J. König, M. M. Salomaa, J. Schmid, H. Schoeller, and G. Schön, *Europhys. Lett.* **40**, 189 (1997).
- [82] A. L. Yeyati, F. Flores, and A. Martín-Rodero, *Phys. Rev. Lett.* **83**, 600 (1999).
- [83] D. Pfannkuche, *Aspects of Coulomb Interaction in Semiconductor Nanostructures*, Max-Planck-Institut für Festkörperforschung, Stuttgart, Germany, 1998.
- [84] V. Fock, *Z. Phys* **47**, 446 (1928).
- [85] C. G. Darwin, *Proc. Camb. Phil. Soc.* **27**, 86 (1930).
- [86] P. L. McEuen, E. B. Foxman, J. Kinaret, U. Meirav, M. A. Kastner, N. S. Wingreen, and S. J. Wind, *Phys. Rev. B* **45**, 11419 (1992).
- [87] R. C. Ashoori, H. L. Stormer, J. S. Weiner, L. N. Pfeiffer, S. J. Pearton, K. W. Baldwin, and K. W. West, *Physica B* **189**, 117 (1993).
- [88] R. C. Ashoori, H. L. Stormer, J. S. Weiner, L. N. Pfeiffer, K. W. Baldwin, and K. W. West, *Surface science* **305**, 558 (1993).
- [89] B. Coqblin and J. R. Schrieffer, *Physical Review* **185**, 847 (1969).
- [90] M. Keller, U. Wilhelm, and J. Weis, unpublished (personal communication).
- [91] D. Pfannkuche, Ph.D. thesis, Max-Planck-Institut für Festkörperforschung, Stuttgart, Germany, 1998.
- [92] D. B. Chklovskii, B. I. Shklovskii, and L. I. Glazman, *Phys. Rev. B* **46**, 4026 (1992).

- [93] R. J. Haug, *Semicond. Sci. Technol.* **8**, 131 (1993).
- [94] R. Landauer, *IBM J. Res. Dev.* **1**, 223 (1957).
- [95] M. Büttiker, Y. Imry, R. Landauer, and S. Pinhas, *Phys. Rev. B* **31**, 6207 (1985).
- [96] These samples were obtained from W. Wegscheider at the Walter-Schottky-Institute in Munich.
- [97] This change was recommended by Christian Albrecht. He had used it successfully for similar problems.
- [98] J. Weis, R. J. Haug, K. von Klitzing, and K. Ploog, *Semicond. Sci. Technol.* **10**, 887 (1995).
- [99] P. Horowitz and W. Hill, in *THE ART OF ELECTRONICS*, edited by P. Horowitz (Cambridge University Press, Cambridge, 1980).
- [100] H. Courtois, O. Buisson, J. Chaussy, and B. Pannetier, *Rev. Sci. Instrum.* **66**, 3465 (1995).
- [101] D. D. Nolte, in *Properties of Gallium Arsenide*, datareviews series ed., edited by M. R. Brozel and G. E. Stillman (inspec, 1996), Vol. 16, Chap. Optical functions of GaAs, p. 201.
- [102] J. S. Blakemore, *J. Appl. Phys* **53**, R123 (1982).

# Resume

Jörg D. Schmid

29. Sept 1968            born in Mainz as Sohn of Dr. Gerhard and Alice Schmid
- Sept 1973 - May 1974    *Zena Elementary School* in Kingston, New York
- Sept 1974 - July 1978    *Grund- und Hauptschule Stetten auf den Fildern* (primary school)
- Aug 1978 - May 1987    *Immanuel-Kant-Gymnasium* in Leinfelden-Echterdingen (secondary school); graduation on May 12, 1987 obtaining the *Abitur*
- Okt 1987 - May 1989    civil service in the *Katholische Sozialstation Biberach* (mobile care for elderly people)
- Mai 1989 - Sept 1989    voyage through China by bike
- Okt 1989                start of studying physics at the *TU Karlsruhe* in Karlsruhe
- Okt 1991                *Vordiplom* in physics
- Sept 1993 - June 1994    *University of Oregon*, Eugene, Oregon; graduated on May 12, 1994 with an MA in physics; book prize for the best exam
- Okt 1994 - Apr 1996    Diploma thesis at the *Institut für Theoretische Festkörperphysik* at the *TU Karlsruhe*
- May 1995                marriage with Michele R. Williams
- May 1996                graduation from the *TU Karlsruhe* with a *Diplom* in physics
- since June 1996        dissertation at the *Max-Planck Institut für Festkörperforschung*, Stuttgart